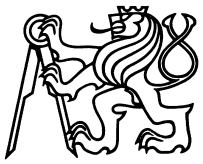

ČESKÉ VYSOKÉ UČENÍ TECHNICKÉ V PRAZE
Fakulta jaderná a fyzikálně inženýrská

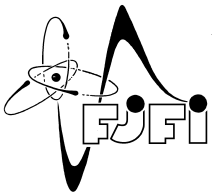

Studium trajektrorií relativistických elektronů v magnetickém poli tokamaku

Studies of trajectories of relativistic electrons in the magnetic field of a tokamak

MASTER'S THESIS

Author: **Jaroslav Čeřovský**

Supervisor: **doc. RNDr. Jan Mlynář, Ph.D.**

Academic year: 2017/2018

- Zadání práce -

- Zadání práce (zadní strana) -

Čestné prohlášení:

Prohlašuji, že jsem svou diplomovou práci vypracoval samostatně a použil jsem pouze podklady (literaturu, projekty, SW atd. ...) uvedené v přiloženém seznamu.

Nemám závážný důvod proti použití tohoto školního díla ve smyslu §60 Zákona č. 121/2000 Sb., o právu autorském, o právech souvisejéících s právem autorským a o změně některých zákonů (autorský zákon).

V Praze dne 7. července 2018 Jaroslav Čeřovský

Poděkování:

Chtěl bych zde poděkovat svému školiteli doc. RNDr. Janu Mlynářovi, Ph.D. za ochotné vedení mé diplomové práce a za jeho vstřícný přístup ke studentům. Nemalý dík si zaslouží Ing. Onřej Ficker, který se svým obětavým přístupem zasloužil na řadě mých dosavadních výsledků a vždy byl zdrojem hodnotných informací. Dále bych chtěl poděkovat Ing. Jakubu Urbanovi, Ph.D., který mi dával cenné rady při implementaci algoritmu. V neposlední řadě bych chtěl poděkovat celé mé rodině a to zejména mamce a taťkovi, kteří mi umožnili studim na vysoké škole a nepřetržitě mě v něm podporovali.

Děkuji.

Jaroslav Čeřovský

Název práce:

Studium trajektorií relativistických elektronů v magnetickém poli tokamku

Autor: Jaroslav Čeřovský

Obor: Fyzika a technika termojaderné fúze

Druh práce: Diplomová práce

Vedoucí práce: doc. RNDr. Jan Mlynář, Ph.D., Katedra fyziky, FJFI ČVUT

Abstrakt: Tato diplomová práce se věnuje problematice tzv. ubíhajících elektronů, které jsou generovány za určitých podmínek v zařízeních typu tokamak. Tyto vysokoenergetické elektrony jsou urychlovany přítomným elektrickým polem a dopad jejich svazku na první stěnu experimentálního zařízení může způsobit závažné škody. Práce v prvé řadě shrnuje zakladní teoretické poznatky z fyziky ubíhající elektronů. Důraz je kladen na výklad metod, pomocí kterých lze počítat trajektorie relativistických částic v magnetickém poli tokamaku, a které byly využity při tvorbě softwaru simulujícího pohyb ubíhajících elektronů v tokamku COMPASS. Výsledky částicových simulací byly porovnány s měřením Čerenkovova detektoru, který je schopen detekovat energetické elektrony unikající z plazmatu.

Klíčová slova: časticové simulace, Čerenkovův detektor, tokamak, ubíhající elektrony

Title:

Studies of trajectories of relativistic electrons in the magnetic field of tokamak

Author: Jaroslav Čeřovský

Abstract: This diploma thesis is dealing with so called runaway electrons, which are generated in the the tokamaks under particular conditions. These high energy electrons are accelerated in the electric field of tokamak and their impact onto the first wall of the experimental facility can cause serious damage. A brief summary of the fundamentals of runaway electron physics is given. The integration schemes dedicated for description of the dynamics of the relativistic particles in the magnetic field of the tokamak are presented. The given schemes were used to implement the program capable to calculate trajectories of the runaway electrons in the COMPASS tokamak. The results of the particle simulations were compared with measurements from the Cherenkov detector, which detects energetic electrons escaping from plasma volume.

Key words: Cherenkov detector, particle simulation, runaway electrons, tokamak

Contents

Introduction

One of the greatest and most expensive scientific project in the mankind history is slowly but gradually being built in Cararache in the France. This project attracts attention not only of the whole fusion community, but the name of the project ITER appears also in the press. The name ITER was originally an abbreviation of the International Thermonuclear Experimental Reactor. ITER project aims to prove feasibility of the thermonuclear fusion, demonstrate physical principles and verify physical models, which were developed during the last decades. ITER is often presented as the final stage of the fusion research and represents main goal of the researches from the 50s, when nuclear fusion began to be seriously investigated. Unfortunately, ITER will be not the end of a long journey, but a new start of the scientific investigation, which could bring the humanity to a nearly sustainable source of energy.

Nuclear fusion Nuclear fusion is opposite process to the well know and commercially exploited nuclear fission. Nuclear fusion is a reaction of two or more atomic nuclei. When incident particles come close enough to form one or more different nuclei and subatomic particles, the energy is released in the form of kinetic energy of the products. One way, how to get nuclei close enough is delivery of relatively large amounts of energy to overcome the Coulomb repulsion, which acts between oppositely charged particles. This way of realisation of nuclear fusion is called thermonuclear fusion. The most promising nuclear reaction, which can lead to a release of relatively large amount of energy could be released, is the fusion reaction of deuterium with tritium

$$D + T \rightarrow {}^{4}He + n. \tag{1}$$

The products of this reaction are an alpha particle and a neutron. 17.6 MeV energy is released by this reaction in the form kinetic energy of products. This fusion reaction is not only favourable from the point of view of the amount of released energy, but especially due to the probability of the realisation. The quantity, which describes the probability of the reaction, is called the cross section. The cross section of the most important fusion reactions is shown in the figure 1. As can be seen in the figure, the fusion reaction of deuterium with tritium has the largest cross section for the lower energies of incident particle and thus is is the most accessible reaction. The importance and advantage of different fusion reactions lies in the type of fusion products. For example the reaction

$$p + {}^{11}B \rightarrow 3{}^{4}He, \tag{2}$$

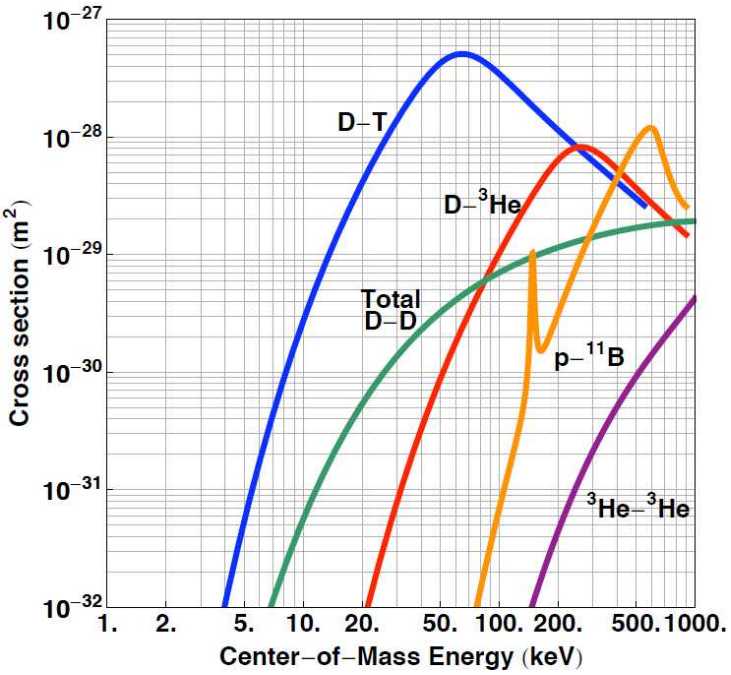

Figure 1: The cross section of the most important fusion reactions. [47]

releases 8.7 MeV of energy, but products of the reaction are only charged particles. This type of fusion reaction belongs to the group, where no neutrons are produces, which are usually called advanced fusion reactions.

Tokamak Thermonuclear reactions require delivery of large amounts of energy to particles of matter. The matter has to be heated up to extreme temperatures, keeping in mind that the temperature is a measure of the average kinetic energy. When the matter is heated up to sufficiently high temperatures, then the matter exists in the state called plasma, which can be simply described as a gas consisting of ions and electrons.

One of the problems, which thermonuclear fusion has to deal with, is the required very high temperature (tens of millions K) of the plasma. The plasma cannot be sustained in any chamber made of conventional materials, because after the contact of the plasma with material the material would essentially ceased to exist while the plasma would decrease temperature and increase impurity contents. However, the scientist proposed come up with so called magnetic confinement. The conception of magnetic confinement is based on an idea, that plasma can be confined by magnetic fields and the fields prevent plasma from touching the wall of the device.

One of the facilities, which can contain the plasma with help of magnetic field, is called a tokamak. The word tokamak is an abbreviation from Russian words with English meaning "toroidal chamber with magnetic coils". The tokamak uses strong toroidal magnetic field generated by toroidal field coils combine with poloidal magnetic field, which is generated by current driven through the plasma column in the toroidal direction. The plasma current is necessary for creation of magnetic field, which is capable to confine the particles of the plasma, but also for heating of the plasma. Unfortunately, plasma is also subject to a number of instabilities. The instabilities limit the operational space of tokamak and they are dangerous for the tokamak

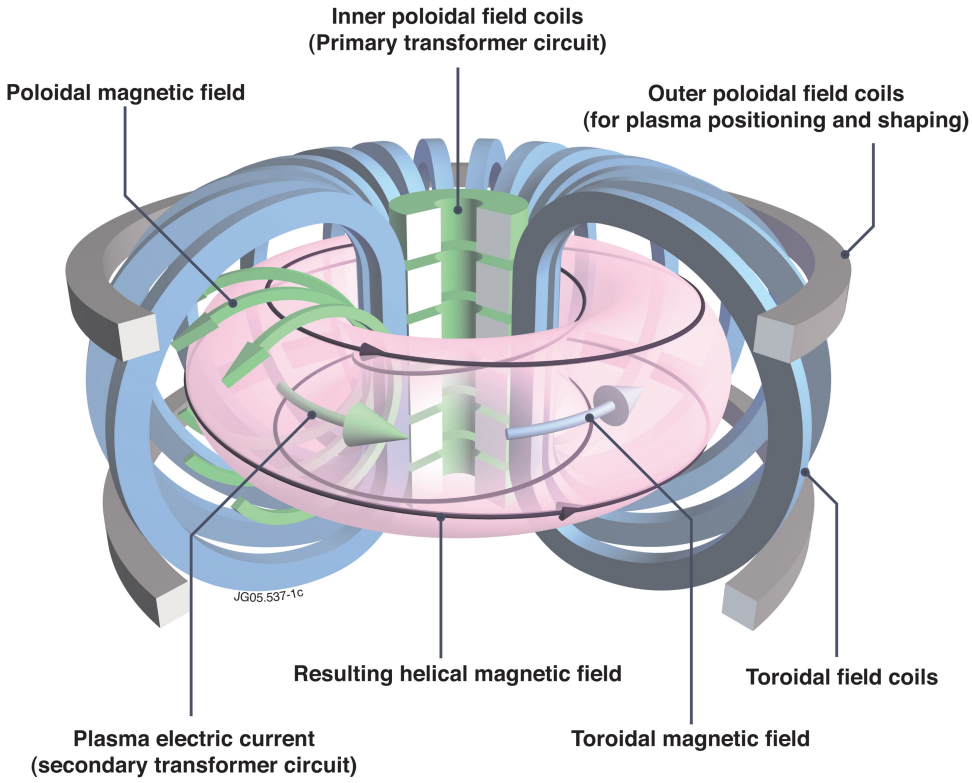

Figure 2: The figure shows the sketch of the tokamak with its main components. [1]

operation. The instabilities can result in sudden termination of the plasma. This particular event is called a disruption and can be accompanied by generation of the runaway electrons.

Runaway electrons The electrons, which are called runaway, are high energy particles with the velocities approaching the speed of light. In tokamaks, the runaway electrons are generated usually during the low density discharges or in the moment of plasma disruption. The need of the current driven through the plasma in tokamaks is linked to induction of the electric field. In the case that the electric force is greater than the mean force caused by the collisions with bulk particles, the electrons can run away. The impact of beam consisting of runaway electrons onto the first wall can damage important components of the tokamak and thus put the facility out of operation. However, the runaway electrons are not only phenomenon observed in the tokamak physics. By the presence of the runaways the principle of the lighting strike or occurrence of the terrestrial gamma-rays are explained.

The runaway electrons are subject of intensive studies on several devices across Europe. The emphasis is especially put on understanding of physics behind generation of the runway electrons and possibilities of their mitigation. According to the numerical simulations of the ITER plasma disruption, the runway electrons can carry several MA of the plasma pre-disruption current. Its energy is sufficient to cause serious damage to the first wall, therefore, reliable mitigation strategy has to be developed before the ITER will be put in operation. Otherwise, the financial investment, the spent human and material resources and future of the fusion research will be put at risk.

As was indicated in the previous paragraph, this thesis deals with the physics of runaway electrons. Main part of the thesis is dedicated to simulation of the trajectories of runaway electrons in the magnetic field of the tokamak. The first chapter in focused on the basics of the runaway electron physics, summarises the generation principles and covers important features of runaway dynamics. In the second chapter, the reader will be introduced into particle motion in electric and magnetic fields. The numerical methods of calculation of the particle trajectory are given. The stress is put especially on numerical schemes capable of correct description of relativistic particles. The algorithm used for determination of the particle trajectory is described in the third chapter. In the fourth chapter the results of the particle simulations are discussed with implications for experimental observations. The final fifth chapter is dedicated to comparison of the experimental results with the measurements.

Chapter 1

Physics of runaway electrons

The operation of future tokamaks and especially tokamak ITER has to deal with several threats, which can put them out of operation and seriously damage experimental facility. Currently, a wide variety of strategies of mitigation of disruptions are under develop, but there are still open questions. The runaway electrons are one of the possible threats, which could be detrimental for the first wall and in-vessel components. This chapter concerns with fundamentals of physics of runaway electrons.

1.1 Introduction to physics of runaway electrons

As it was said in the introduction of this thesis, runaway electrons are high-energy particles, which can be generated in tokamaks by the toroidal electric field. Runaway electrons occur, when electric force $\boldsymbol{F_e} = -e\boldsymbol{E}$ exceeds friction force $\boldsymbol{F}_d = -m_e\nu\boldsymbol{v}$, where e is the elementary charge, m_e is mass of the electron and ν denotes collisional frequency. Electron collision frequency for suprathermal electrons, i.e. electrons with much higher velocities than the thermal velocity, can be approximated by formula

$$\nu = \frac{n_e e^4 \ln\Lambda}{4\pi\epsilon^2 m_e^2 v^3}. \tag{1.1}$$

Here n_e is the electron density, e elementary charge, $\ln\Lambda$ is the Coulomb logarithm, ϵ is the permitivity of vacuum, m_e and v denote the electron mass and the electron velocity respectively. Furthermore Coulomb logarithm is defined as

$$\ln\Lambda = \ln\left(\frac{\lambda_D}{b_0}\right), \qquad \lambda_D = \sqrt{\frac{\epsilon_0 k_B}{\Sigma_\alpha Q_\alpha^2 n_\alpha / T_\alpha}}, \tag{1.2}$$

where λ_D is so called Debye length and b_0 is the critical collision parameter or impact parameter. The collision parameter is the perpendicular distance between the path of the particle and the center of a potential field created by another particle that the scatter particle is approaching. Than the critical collision parameter represent the perpendicular distance in which the scattering angle equals 90°. The Debye length has great importance in plasma physics, because this length

characterizes scale of interaction between individual particles in plasma. Movement of electron in electric field can be described by simplified equation of motion

$$m_e \frac{\mathrm{dv}}{\mathrm{d}t} = -eE - m_e \nu v \approx -eE - \frac{n_e m_e e^4 ln\Lambda}{4\pi\epsilon^2 m_e^2 v^2}. \tag{1.3}$$

Here E denotes the magnitude of electric field. From this equation we can draw a simple conclusion. When the right hand side of the equation (1.3) is negative, the electron will be slowed down, when the right hand side is positive the electron is accelerated and will run away. Whether the electron will be accelerated or slowed down depends on its the initial velocity. If we set the time derivative in the equation (1.3) to zero, we can determine the critical velocity. The critical velocity is given by equation

$$v_c = \sqrt{\frac{n_e e^3 \ln\Lambda}{4\pi\epsilon^2 m_e E}}. \tag{1.4}$$

Electrons with higher velocities than critical velocity v_c, will be accelerated. As can be seen from the equation (1.4), the critical velocity is proportional to the reciprocal value of the square root of intensity of the electric field E and the square root of the electron density n_e. This means that the electrons will run away especially in low density plasma with high applied external electric field. Due to the fact, that the speed of any object is limited by the speed of light, the critical field E_c exists [10]. Below this value of the electric field, it is not possible to electron runaway. The critical field is given by

$$E_c = \frac{n_e e^3 \ln\Lambda}{4\pi\epsilon_0^2 mc^2}, \tag{1.5}$$

where c denotes the speed of light in vacuum. If a more precise treatment is followed and the collision with the ions are taken into account, a slightly different formula can be derived for the critical velocity, which can be expressed by

$$v_c = \sqrt{\frac{n_e e^3 \ln\Lambda(2 + Z_{eff})}{4\pi\epsilon^2 m_e E}}, \tag{1.6}$$

$Z_{eff} = \frac{\Sigma_j n_j Z_j}{n_e}$ is the effective charge. The initial energy that an electron runaway needs to become a runaway electron can be estimated by the formula

$$W_c = \frac{1}{2} m_e v_c^2 \approx 2.2(2 + Z_{eff}) \frac{n_e[10^{-19}\mathrm{m}^{-3}]}{E[\mathrm{V/m}]}\ \mathrm{keV}. \tag{1.7}$$

The formula 1.7 is applicable only in low density plasmas, otherwise the relativistic formula for energy has to be used. Here, it has to be noted that the collision frequency is not a decreasing function of velocity in the whole range of velocities. For velocities smaller than the thermal velocity v_T, the collisional frequency is almost independent on velocity and the friction force increases linearly with the velocity. The friction force reaches its maximum at the thermal speed and than it is decreasing function of velocity. The mentioned situation is illustrated in the figure 1.1. The black curve represents the friction force, which is expressed by so called

Chandrasekhar function. The red one is accelerating force given by electric field. The graph is divided by intersections of these curves into three regions. In the first and the third region the accelerating force dominates. However, border between region I. and II. is stable and therefore the electrons will runaway only in the third region.

1.2 Generation of runaway electrons

In this section, the description of the mechanisms of generation of runaway electrons are given. The mechanisms of generation can be divided into two groups. First group covers mechanisms, which do not need previous existence of suprathermal electrons and these are called primary generation mechanisms. These mechanisms provide runaway electron seed, which can be multiplied by secondary generation mechanism. In the small tokamaks, the Dreicer primary generation dominates over the secondary - avalanche mechanism. The so called hot-tail mechanism takes place exclusively during the plasma disruption. Other two possible generation mechanisms will be discussed in the following section.

1.2.1 Primary generation

1.2.1.1 Dreicer generation

The production mechanism of RE described in the previous section is in the literature called Drecier mechanism after H. Dreicer, who as the first described the mentioned phenomena [11, 12]. The Dreicer in his work introduce an important quantity, which is nowadays called after him the Dreicer field and the value of the field need to cause all electrons to run away. The Dreicer field is expressed by formula

$$E_D = \frac{n_e e^3 \ln \Lambda}{4\pi\epsilon^2 k T_e}, \tag{1.8}$$

where k is the Boltzmann constant and T_e is temperature of electrons. The growth rate of the runaway population is characterized by [10]

$$\frac{\mathrm{d}n_r}{\mathrm{d}t} = C n_e \nu_{th} \varepsilon^{-3(1+Z_{eff}/16)} \exp\left(-\frac{1}{4\epsilon} - \sqrt{\frac{1+Z_{eff}}{\varepsilon}} \right). \tag{1.9}$$

Here n_r is runaway electron density, $\varepsilon = \frac{E}{E_D}$, C is constant in order of unity not determined by analytical model and v_{th} is electron-electron collisional frequency of thermal particles given by

$$\nu_{th} = \frac{n_e e^4 \ln \Lambda}{4\pi\epsilon^2 m_e^2 v_{th}^3}. \tag{1.10}$$

1.2.1.2 Hot-tail mechanism

The following generation process significantly differs from previous Dreicer mechanism and it is associated with plasma instability. Hot-tail generation [36] process is caused by incomplete thermalization of electrons during sudden plasma colling, which is one of the first stages of

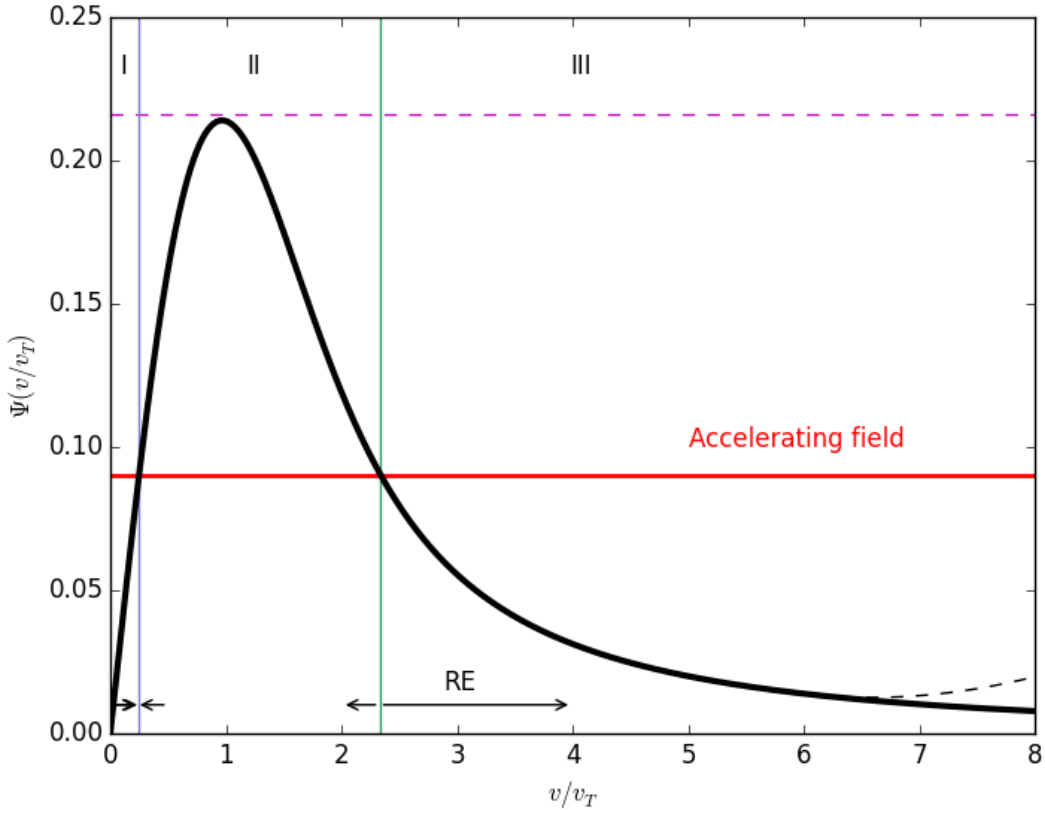

Figure 1.1: Illustration of the basic mechanism of the generation of the runaway electrons. The plotted Chandrasekhar function (black) represents the friction force, which is caused by Coulomb collisions with bulk plasma particles. The red curve is constant accelerating force acting on the particles and given by the value of the electric field. The intersections of these two curves divide the graph into three regions. The border between the first and the second region (blue line) is stable, but the border of the second and the third region is unstable and all particles to the right of this border are accelerated. For higher velocities, radiation effects have to be taken into account and the friction force acting on electrons rises and prevents electrons to gain higher speed than is speed of light. Courtesy of O. Ficker [14]

.

rapid plasma termination called disruption. During rapid plasma cooling, which is often caused by presence of impurities, electrons are decelerated by ionization and excitation. The electrons with high enough velocities have very low collisional frequency and on the time scale of thermal quench undergo negligible number of major collisions and these electrons are not thermalized as the rest of the bulk particles. This means that the time between two collisions τ (reversed value of collisional frequency) of particles with enough kinetic energy is longer than or comparable to characteristic time of thermal quench t_0. This mechanism of generation of runaway electrons is called hot-tail mechanism, because the emerging runaway electrons have their origin in the hot tail of the Maxwellian distribution function. The growth rate of the runaway electron population by hot tail mechanism can be estimated by formula [35]

$$\left(\frac{\mathrm{d}n_r}{\mathrm{d}t}\right)_{hot-tail} = 4\pi\frac{\mathrm{d}}{\mathrm{d}t}\int_{v_c}^{+\infty}(v^2 - v_c^2)f\,\mathrm{d}v, \tag{1.11}$$

where v_c is the critical velocity for the runaway generation. If we assumed the exponential decrease of temperature during the thermal quench, $T = T_0 e^{-\frac{t}{t_0}}$ (t_0 denotes characteristic time of duration of the thermal quench), one may obtain simple analytical formula for estimation the runaway density

$$n_r^{hot-tail} \approx n_{e0}\frac{2}{\sqrt{\pi}}u_{c,min}e^{u_{c,min}^2} \tag{1.12}$$

with

$$u_{c,min}^3 = t_0\nu_0\left[2\ln\frac{E_{D0}}{E_{\|0}} - \frac{4}{3}\ln\left(\frac{4}{3}t_0\nu_0\right) - \frac{5}{3}\right] \tag{1.13}$$

. Here n_{e0} is the initial density of electrons, v_{T0} is the initial thermal speed of background electrons, $\nu_0 = \frac{n_{e0}e^4\ln\Lambda}{4\pi\varepsilon_0^2 m_e^2 v_{T0}^3}$ is the collisional frequency of the thermal electrons before disruption and the $E_{D0}/E_{\|0}$ initial ratio of Dreicer electric field and parallel electric field. The above formula is known to overestimate the number of high energy electrons compared to the more precise kinetic treatment.

1.2.1.3 Tritium decay

Naturally occurring trititum is extermely rare on Earth, because of radiocative nature and short half-life of this isotope of hydrogen. Half-time of the tritium τ_T is 4500 ± 4 days and tritium decay into helium is described by formula

$$T \rightarrow {}^3_2\mathrm{He} + e^- + \bar{\nu}_e, \tag{1.14}$$

which states, that the products of the reaction is helium, electron and the electron antineutrino. The rate of production of β particles is given by [26]

$$\left(\frac{\mathrm{d}n_\beta}{\mathrm{d}t}\right) = \lambda_T n_T = \ln 2\frac{n_T}{\tau_T}. \tag{1.15}$$

Here n_T is density of trititium and $\lambda_T = \ln 2/\tau_T$ is denotes decay constant. Maximum kinetic energy of the released electrons is 18.6 keV and the average energy is 5.7 keV. The generation rate of the runaway electrons by the tritium decay is expressed as

$$\left(\frac{\mathrm{d}n_r}{\mathrm{d}t}\right)_{tritium} = \lambda_T n_T = \ln 2 \frac{n_T}{\tau_T} F_\beta(E_c), \tag{1.16}$$

where $F_\beta(E_c)$ is a fraction of the beta spectrum that would become runaway. This fraction of beta particles can be calculated from equation

$$F_\beta(E_c) = \int_{E_c}^{E_{max}} f_\beta(E)\mathrm{d}E, \tag{1.17}$$

$f_\beta(E)$ is spectrum of beta particles normalized to one, E_c is critical energy and E_{max} is maximum energy of beta particles. The growth rate 1.16 does not include the dependence on the electric field, which plays an important role in the runaway generation. The runaway electrons cannot be born, if the initial velocity of the electron is oriented oppositely to the direction of the electric field. So the formula 1.16 overestimates the number of generated runaway electrons.

1.2.1.4 Compton scattering

Another way of generation of the ruanaway electrons, which is unimportant in the present day tokamaks is Compton scattering of γ rays with electrons. In the DT phase of the ITER the γ rays will be emitted by activated wall and the rate of the runaway generation can be estimated by formula [26]

$$\left(\frac{\mathrm{d}n_r}{\mathrm{d}t}\right)_{compton} \approx n_e \int \Gamma_\gamma(E_\gamma)\sigma(E_\gamma)\mathrm{d}E_\gamma, \tag{1.18}$$

E_γ is the photon energy, $\Gamma_\gamma(E_\gamma)$ the gamma flux energy spectrum and $\sigma(E_\gamma)$ the Compton cross-section for photons of energy E_γ. The total gamma flux is in ITER estimated as $10^{20}\mathrm{m}^{-2}\mathrm{s}^{-1}$ The Compton scattering is a well understood process, in which the γ rays are scattered on electrons. The energy of photon E'_γ, which undergoes the Compton scattering is determined by the formula

$$E'_\gamma = \frac{E_\gamma}{1 + \frac{E_\gamma}{m_e c^2}(1 - \cos\theta)}. \tag{1.19}$$

Here θ is the scattering angle. If we are interested in the production of runaway electrons, we have to consider only these scattering events, where electrons gain enough energy to become runaways. This condition is experessed $E_e = E_\gamma - E'_\gamma \geq E_c$, where E_e is energy of incident electron and E_c is the critical energy. The total cross-section for the Compton scattering, which appears in (1.18) is calculated from following equation

$$\sigma(E_\gamma) = \int_{\theta_c}^{\pi} \frac{\mathrm{d}\sigma}{\mathrm{d}\Omega}\mathrm{d}\Omega, \tag{1.20}$$

$\frac{\mathrm{d}\sigma}{\mathrm{d}\Omega}$ is the differential cross section and integration is performed from so called critical angle θ_c. This is the smallest scattering angle, which causes generation of runaway electron and can be determined from equation (1.19). Generation mechanism describe here together with tritium decay can provide additional sources of primary runaway electrons, which can be then multiplied by the avalanche mechanism. As it was noted in the previous subsection, the formula

1.18 overestimates the number of generated runaway electron, because does not include some factor, which represents dependence on direction of initial energy with respect to orientation of the toroidal magnetic field.

1.2.2 Secondary generation

Unique and very important process, which leads to creation of runaway electrons and depends on already existing runaway population is the secondary generation or often in the literature called avalanche mechanism [34]. Secondary runaways are formed when existing runaway electrons collide with thermal electrons and the runaway electron transfers enough energy to thermal electron to kick it into the runaway region while incoming electron remains in the runaway region. This type of collisions are called a knock-on collision and it is quite rare in the tokamak plasmas. In large tokamak the avalanche mechanism plays the main role in the runaway electron generation process and this source of production of RE will be crucial for ITER.

If we follow simple description of the avalanche mechanism given in the previous paragraph, we can derive simple conclusions. The energy of incoming particle must satisfy inequality $W_i > 2W_c$, where W_i and W_c are energy of incoming particle and the critical energy, respectively. The rate of generation of the runaway electrons by the avalanche mechanism is given by [10]

$$\frac{\mathrm{d}n_r}{\mathrm{d}t} = \frac{n_r(E_r - 1)}{\tau \ln \Lambda} \sqrt{\frac{\pi\Gamma}{3(Z_{eff} + 5)}}(1 - E_r + \frac{4\pi(Z_{eff} + 1)^2}{3\Gamma(Z_{eff} + 5)(E_r^2 + 4/\Gamma^2 - 1)})^{-1/2}, \tag{1.21}$$

where $E_r = \frac{E}{E_c}$ denotes relative strength of electric field, Γ is so called neoclassical function, which describes the effects of the toroidal geometry, and $\tau = \frac{m_0 c}{eE_c}$. So called neoclassical function Γ can be roughly expressed as

$$\Gamma \approx (1 + 1.46\sqrt{\varepsilon} + 1.72\varepsilon)^{-1}, \tag{1.22}$$

where ε represents the tokamak aspect ratio ($\varepsilon = \frac{a}{R_0}$). The equation 1.21 takes a simple form for very strong fields ($E_r \gg 1$), $Z_{eff} = 1$ and large aspect ratios ($\varepsilon \to 0$)

$$\frac{\mathrm{d}n_r}{\mathrm{d}t} = \sqrt{\frac{\pi}{2}} \frac{n_r}{3\tau \ln \Lambda}(E_r - 1). \tag{1.23}$$

It is important to realise, that rate of generation of the runaway electrons by the avalanche mechanism depends on number of electrons in the runaway region. Therefore the population of RE is increased exponentially by this mechanism.

Provided that the secondary generation dominates over the primary mechanisms, the quasi-steady runaway electron distribution function can be determined analytically. The results is given by [16]

$$f_{ava}(p_\parallel, p_\perp) = \sqrt{\frac{\pi}{3(Z_{eff} + 5)}} \frac{n_r \hat{E}}{2\pi p_\parallel \ln \Lambda} \exp(-\sqrt{\frac{\pi}{3(Z_{eff} + 5)}} \frac{p_\parallel}{\ln \Lambda} - \frac{\hat{E} p_\perp^2}{2p_\parallel}), \tag{1.24}$$

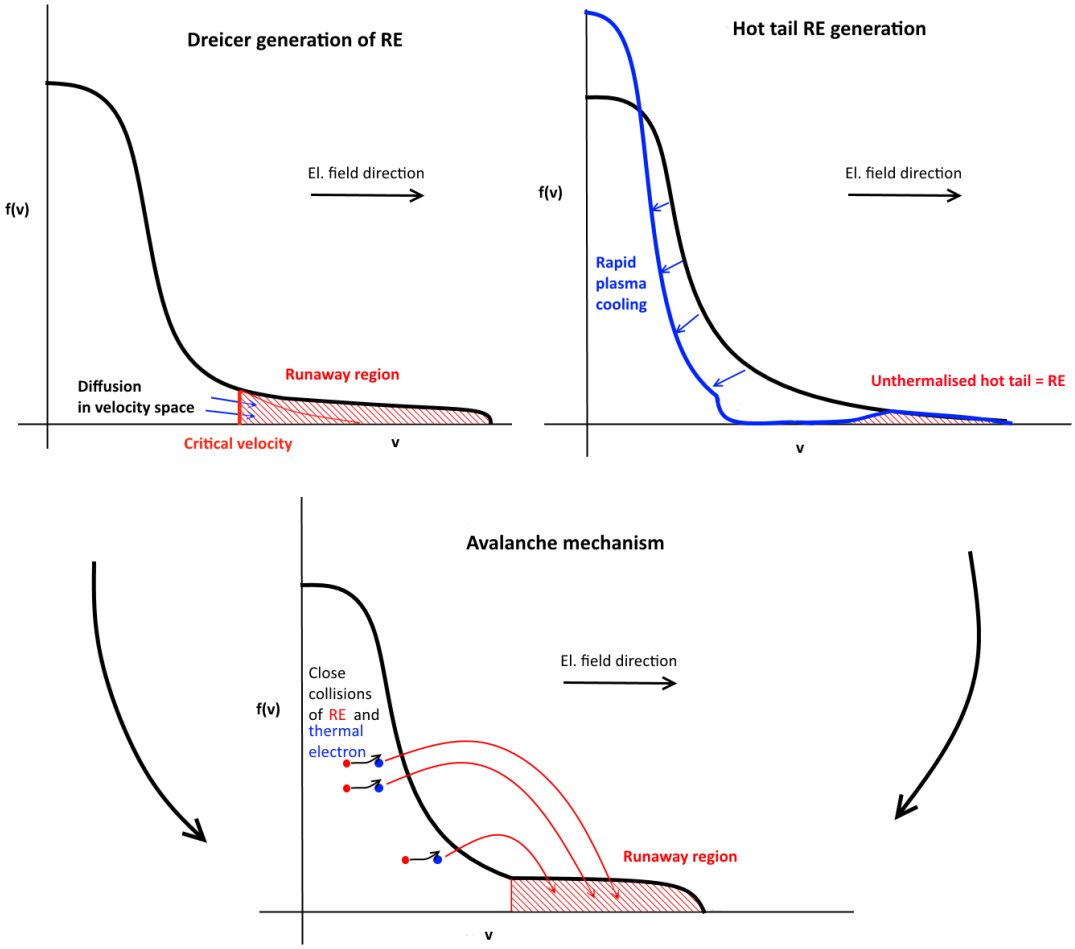

Figure 1.2: Illustration of the three most important mechanisms of production of RE. The figures show effects on the distribution function. Courtesy of O. Ficker [14].

where $\hat{E} = \frac{E/E_c - 1}{1+Z_{eff}}$, $p_{\parallel}$ and $p_{\perp}$ are parallel and perpendicular components of normalized momentum with respect to magnetic field. This equation is valid only, when the following assumptions are satisfied: $\gamma \gg 1$ and $E/E_c \gg 1$, where γ denotes the relativistic factor or the Lorentz factor given by following formula $\gamma = \frac{1}{\sqrt{1-\frac{v^2}{c^2}}}$

1.3 Radiation of runaway electrons

Study of radiation of runaway electrons has a great importance not only from the diagnostics point view, but also for mitigation strategies, which are under develop for protection of experimental facilities. Study of synchrotron and ECE emission from runaway electrons belongs to unique techniques capable of giving some information about distribution function of RE allowing deeper insight into RE physics.

Every charged particle, which experience acceleration, emits radiation while the particle is loosing their energy. The dipole radiation power of an accelerated particle is

$$P = \frac{e^2 a^2}{6\pi\epsilon_0 c^3}, \tag{1.25}$$

where a is acceleration of the particle. Following sections will discuss the different types of radiation of charged particles. First of all the effects of the particle radiation will be summarized. Then the specific types of radiation are listed.

1.3.1 Radiation reaction force

As it was said, an accelerating charge particle emits radiation. The emission of electromagnetic radiation cause a recoil force which acts on a particle. In the relativistic case, the reaction force is represented by the Abraham-Lorentz-Dirac force [22]

$$\boldsymbol{F}_{rad} = \frac{q^2\gamma^2}{6\pi\epsilon_0 c^3}\left[\dot{\boldsymbol{v}} + \frac{3\gamma^2}{c^2}(\boldsymbol{v}\cdot\dot{\boldsymbol{v}})\,\dot{\boldsymbol{v}} + \frac{\gamma^2}{c^2}\left(\boldsymbol{v}\cdot\ddot{\boldsymbol{v}} + \frac{3\gamma^2}{c^2}(\boldsymbol{v}\cdot\dot{\boldsymbol{v}})^2\right)\right] \tag{1.26}$$

where q is the elementary charge and γ is Lorentz factor given by equation

$$\gamma = \frac{1}{\sqrt{1-\frac{v^2}{c^2}}}. \tag{1.27}$$

This form of equation (1.26) is impractical and it can be easily seen that it is dependent on second derivatives of velocity. Notwithstanding, the more practical formula can be found under some assumptions. If we consider that particle motion is dominated by the cyclotron motion, i.e. $\boldsymbol{v}\cdot\dot{\boldsymbol{v}} \approx 0$ and with help of a relation

$$\ddot{\boldsymbol{v}} = -\frac{q^2B^2}{\gamma^3 m^3}\boldsymbol{p}_\perp, \tag{1.28}$$

which follows from the Lorentz equation, equation for ALD force becomes

$$F_{rad} \approx -\frac{1}{\tau_r}\left(\boldsymbol{p}_\perp + \frac{p_\perp^2}{(mc)^2}\boldsymbol{p}\right), \tag{1.29}$$

where $\tau_r = \frac{q^4B^2}{6\pi\epsilon_0\gamma(mc)^3}$ is characteristic time scale for the radiation reaction force.

1.3.2 Bremsstrahlung

On of the radiative processes influencing the runaway electron dynamics is the bremsstrahlung. This type of radiation was already mentioned earlier with connection of RE wall interaction. The bremsstrahlung denotes radiation process, which occurs during Coulomb collisions and that is caused by abrupt acceleration of the incident particles. The spectrum of single electron scattered on ion is given by

$$P(\lambda) = \frac{4\pi}{3}\frac{Z^2e^6}{m_e c^3 b^2 v^2}e^{-\frac{4\pi cb}{\lambda v}} \tag{1.30}$$

Spectrum of the particle is dependent on the velocity of the incident electron v and on the properties of the ion. The drag force, which is associated with the bremsstrahlung radiation and is caused by the Coulomb interactions with the ions is equal to [13]

$$F_B^{e-i}(p) = -\frac{\alpha}{\pi}\frac{eE_c Z_{eff}}{\ln\Lambda}(\gamma-1)\left(\ln 2\gamma - \frac{1}{3}\right), \tag{1.31}$$

where E_c denotes the critical electric field and Z_{eff} the effective charge. If we investigate the influence of bremsstrahlung on dynamics of the runaway electrons, we cannot omit the interaction with the background electrons. The drag force caused by Coulomb collisions of runaway electrons with the electrons is given by

$$F_B^{e-e}(p) = -\frac{\alpha}{\pi}\frac{eE_c}{\ln\Lambda}(\gamma-1)\left(\ln 2\gamma - \frac{1}{3}\right). \tag{1.32}$$

The only difference between equations (1.31) and (1.32) is in the value of the effective charge Z_{eff}. Therefore, the drag force caused by interaction with all plasma species is equal to

$$F_B(p) = -\frac{\alpha}{\pi}\frac{eE_c\left(1+Z_{eff}\right)}{\ln\Lambda}(\gamma-1)\left(\ln 2\gamma - \frac{1}{3}\right). \tag{1.33}$$

The bremsstrahlung is an important energy loss channel of the runaway electrons. Unlike the synchrotron radiation, the bremsstrahlung is independent of the magnetic field, but is affected by density and plasma species. The enhanced bremsstrahlung can be expected in the dense plasma with the presence of impurities.

1.3.3 ECE emission

Each charged particle moving in the magnetic field emits the radiation.The circular movement of charged particles causes this behaviour. If only non-relativistic movement of particles is assumed, the particles are capable to emit radiation only on frequencies given by

$$\omega_c = \omega_c(B) = \frac{eB}{m} \tag{1.34}$$

Here B is the strength of the magnetic field, e the elementary charge and m is the mass of the particle. Due to finite Larmor radius effects particles emit the cyclotron emission not only on cyclotron frequency but also on its harmonics $n\omega_c$. If we take into account relativistic effects, then the frequency, which can be emitted or absorbed by the particle, is equal to

$$\omega = \omega_c(B)/\gamma + k_{\|}v_{\|}, \tag{1.35}$$

where k is the wave vector and $v_{\|}$ is the parallel component of the velocity. Due to the fact that the magnetic field in the tokamaks varies in space, the electron cyclotron emission is widely used for determining the electron temperature with spatial resolution. In the case that the relativistic effect are dominating, the cyclotron emission is not useful for estimation of temperature, but can be used for investigation of the properties of runaway electrons. It is convenient to locate antenna for detection of the cyclotron emission along the constant value of the toroidal

magnetic field for measurements of features of runaway electrons. This set up is called vertical ECE (V-ECE).

1.3.4 Synchrotron radiation

Synchrotron radiation is electromagnetic radiation of charged particles emitted when the particles are accelerated perpendicular to their velocity ($\boldsymbol{a} \perp \boldsymbol{v}$). If the particles are moving with velocity much lower than the speed of light, e. g. non-relativistic, then this kind of radiation is called cyclotron emission. The term synchrotron radiation refers to relativistic or ultra-relativistic particles. The investigation of synchrotron radiation caused by runaway electrons is an important possibility how to determine the distribution function of the runaway electrons. It has to be noted that the software, which is capable to reconstruct the distribution function of runway electrons from the measured synchrotron radiation was developed recently. The diagnostic tool SOFT (Synchrotron-detecting Orbit Following Toolkit) [20, 21] already demonstrate the usefulness of this approach and helps to infer additional information from experimental measurements of spatial and spectral distribution of the synchrotron radiation. Spectral density of the synchrotron radiated power from a single electron can be expressed as

$$P_{synch}(\lambda) = \frac{1}{\sqrt{3}} \frac{e^2 c}{\epsilon_0 \gamma^2 \lambda^3} \int_{\lambda_c/\lambda}^{\infty} K_{5/3}(l)\,\mathrm{d}l, \tag{1.36}$$

where $\lambda_c = \frac{4\pi}{3}\frac{c}{\omega_c \gamma^2} = \frac{4\pi}{3}\frac{cm_e\gamma_\parallel}{eB\gamma^2}$ is a critical wavelength, λ is a wavelength of the induced radiation and $\gamma_\parallel$ is a Lorentz factor of the parallel component of the velocity ($\gamma_\parallel = \frac{1}{\sqrt{1-\frac{v_\parallel^2}{c^2}}}$), $K_{5/3}$ is a modified Bessel function of the second kind. Under some assumptions, equation (1.36) can be simplified and expressed in the form

$$P_{synch} = \frac{e^4}{6\pi m \epsilon_0 m_e^2 c} B^2 p_\perp^2. \tag{1.37}$$

From previous equation, we can deduce some important features of the synchrotron radiation. Firstly, the synchrotron radiations plays an important role in high magnetic fields. Secondly, particles with high perpendicular component of the momentum are more affected by the synchrotron radiation reaction force. If we would like to study the synchrotron radiation of the whole runaway population, we have to use

$$P_{synch}^{Re} = \frac{2\pi}{n_r} \int_{\Omega_{Re}} f_{Re}(p,\psi) P_{synch}(p,\psi,\lambda) p^2 \mathrm{d}p\mathrm{d}\psi. \tag{1.38}$$

Here f_{Re} is distribution function of the runaway electrons. As it was said in the beginning of this section, the emission of the radiation by the particle is associated with the recoil force, which acts on the particle. The drag force of the synchrotron radiation is given by [39]

$$F_{synch} = \frac{2}{3} r_e m_e c^2 \left(\frac{v}{c}\right)^3 \gamma^4 \left\langle \frac{1}{R^2} \right\rangle \tag{1.39}$$

with

$$\left\langle \frac{1}{R^2} \right\rangle \approx \frac{1}{R_0^2} + \frac{\sin^4 \theta}{r_l^2}. \tag{1.40}$$

The formula (1.40) has a meaning of the average field line curvature and is given by major radius of the tokamak R_0 and by Larmor radius r_l. The θ can be determined from the relation $\cos\theta = \frac{v_\parallel}{v}$, where $v_\parallel$ and v are parallel velocity with respect to the magnetic field and velocity of the particle, respectively.

1.3.5 Cherenkov radiation

Another radiative process, which was theoretically described and can be used for detection of RE in tokamaks or even play role during the motion of the RE in plasma is the so called Cherenkov radiation [9, 6]. When the particle travels through the dielectric medium, it polarizes atoms of the dielectric medium around it and causes them to briefly radiate as they relax to the original state. When a particle is moving slowly the polarization is symmetrical and no significant radiative output is observed, but if particle is moving faster than the phase velocity of light in the dielectric medium, then its own electromagnetic field is moving slower than the particle and it results in an asymmetry in polarization. Asymmetrical polarization causes the radiation, which is emitted in the direction of the motion. The Cherenkov radiation can be emitted only in the environments with the refractive index greater than one. The condition, which has to be fulfilled, states that $n\beta > 1$. The Cherenkov radiation is always described by a simple relation

$$\cos\theta_c = \frac{1}{n\beta}, \tag{1.41}$$

which gives into relation properties of the environment, particle and emitted radiation. The Cherenkov angle θ_c is an angle of the cone in direction of the moving particle in which the radiation is the emitted. The total amount of energy emitted by particle on the path through medium can be calculated using

$$\frac{\mathrm{d}W}{\mathrm{d}x} = \frac{q^2}{c^2} \int_{\beta n(\omega)>1} \omega \left(1 - \frac{1}{n^2(\omega)\beta^2}\right) \mathrm{d}\omega. \tag{1.42}$$

The integral given above is always finite, because the refractive index become unity at high frequencies. The plasma can have also refractive index greater than one and thus the particles can emit Cherenkov radiation. The emitting of radiation is again associated with the recoil force. The drag force caused by the Cherenkov effect is equal to [24]

$$F_{ch} = -\frac{e^2 \omega_{pe}}{v^2} \ln\Lambda, \tag{1.43}$$

where $\omega_{pe} = \sqrt{\frac{n_e e}{m\epsilon_0}}$ is the plasma frequency. This relation is applicable only to unmagnetised plasma. In magnetised plasma equation (1.43) has the following form

$$F_{ch}^{mag} = -\frac{e^2\omega_{pe}^2}{v^2}\left[\ln\Lambda + \ln\frac{v}{v_{th}} + \ln\frac{\sqrt{\omega_{pe}^2+\omega_{ce}^2}}{\omega_{pe}}\right] \tag{1.44}$$

Here v_{th} denotes thermal velocity. ω_{pe} and ω_{ce} states for electron plasma frequency and electron cyclotron frequency respectively.

1.4 RE-wall interaction

The threats with the generation of the runaway electrons are mostly associated with their impact of the first wall of the experimental device and with potential damage. Due to these fact, it is important to understand the physics responsible for interaction of fast electrons with the solid material. The detection of consequences of the described interaction is in some cases the only way, how to get some information of properties of runaway electrons.

The electrons penetrating matter lose their energy by the ionization or by bremsstrahlung. The relativistic factor of the electrons of interest always fulfilled the condition $\gamma \gg 1$ (electron with energies in range $20 - 300$ MeV). For those electrons the ionization loss is independent of their energy [2] and is a function of the density. The ionization loss rate could by than approximated by relation

$$\left(\frac{\mathrm{d}E}{\mathrm{d}x}\right)_{ion} \approx -2\cdot\rho\,\frac{\mathrm{MeV}}{\mathrm{cm}}, \tag{1.45}$$

where the ρ is a density of the medium. This type of energy losses results in heat generation in the material. The different situation is in the case of bremsstrahlung. The electrons lose their energy in radiative collisions with atomic nuclei

$$\mathrm{e}^- + \text{nucleus} \rightarrow \mathrm{e}^- + \text{nucleus} + \gamma. \tag{1.46}$$

Here γ denotes a photon generated by this reaction. The total radiation loss of the electron penetrating a medium of thickness $\mathrm{d}x$ is

$$\left(\frac{\mathrm{d}E}{\mathrm{d}x}\right) = -\frac{E}{X_0}, \tag{1.47}$$

E is energy of electron and X_0 is radiation length of the material, which is inversely proportional to the density and the atomic number Z of the material. Due to the fact, that the ionization loss for fast electrons is approximately constant and the radiation loss via bremsstrahlung is proportional to the energy of electrons. The radiative energy loss dominates over ionization. The so called critical energy can be defined as the energy at which the effect of the two processes on the energy loss of an electron is about equal. The E_c could be roughly given as a function of Z:

$$E_c \approx \frac{600}{Z}\ \mathrm{MeV} \tag{1.48}$$

For the iron, beryllium and carbon the critical energy E_c is 26, 150, 100 MeV. The measured HXR spectra can be very helpful from diagnostic point of view. The intensity of the HXR radiation gives the rough information about number of interacting particles and the measured energies of photons tell about spectrum of incident runaway electrons. However, the proper reconstruction of the properties of runaway electrons from measured HXR is a very ill-posed problem, but under some assumptions could be done.

In the case when the energy of the incident particle is high enough, the photon generated by bremsstrahlung effect can interact with nuclei of the material and the neutron could be released. This neutron is called photo-neutron [17] and is a result of nuclear transmutation of the nuclei into the different isotope. The relevant reactions are

$$\begin{aligned} {}^{2}D(\gamma, n)H \quad & E_{th} = 2.2 \text{ MeV} \\ {}^{12}C(\gamma, n)^{11}C \quad & E_{th} = 18 \text{ MeV} \end{aligned} \tag{1.49}$$

Chapter 2

Modeling of trajectories of RE

Analytical approach of solving particular equations of motions is impossible for almost all real physical systems. In these situations grow importance of numerical methods, which are capable at least approximate evolution of the system. Due to various time scales of the involved processes it is possible to utilize different ways of computing trajectories of particles in electromagnetic fields. Firstly, we can start with Lorentz equation and solve it. This method is called full orbit modelling, because the whole Larmor radius is reconstructed. Another approach of calculating the trajectory of the particle is to used so called guiding centre approach [5]. This method relies on different time scales of movements of charged particles in the electromagnetic fields. In this chapter, the basis of description of movement of charged relativistic particle in electro-magnetic field is given. The various schemes for calculation of particles orbit are discussed. The following chapter also deals with guiding center description of particle motion.

2.1 Motion of relativistic particle

If we want to analyse the movement of the relativistic particles, one of the many ways to do it is to employ the Lagragian theory. Lagragian theory works with so called Lagragian, which is a function of kinetic and potential energy. This function is given as $L = T - V$, where T denotes kinetic energy and V potential energy. If we assume that our system of interest consists of single particle with mass m_0 in a given electromagnetic field. The Lagragian can be written in the form

$$L = -m_0 c^2 \sqrt{1 - \frac{\boldsymbol{v}^2}{c^2}} - q\Phi + q\boldsymbol{A} \cdot \boldsymbol{v}, \tag{2.1}$$

where $\boldsymbol{v}$ is velocity of the particle, Φ is the electric potential, $\boldsymbol{A}$ is vector potential, c and q are speed of light and electric charge of particle, respectively. Equations of motion of particle can be extracted from function 2.1 with help of the Euler-Lagrange equations, which read

$$\frac{\mathrm{d}}{\mathrm{d}t}\left(\frac{\partial L}{\partial \dot{\boldsymbol{q}}_i}\right) - \frac{\partial L}{\partial \boldsymbol{q}_i} = 0, \tag{2.2}$$

where L stands for the Lagragian. The derivatives are made with respect to generalized coordinates $\boldsymbol{q}_i$ and generalized velocities $\dot{\boldsymbol{q}}_i$. From Lagragian formalism, we can move to the Hamiltonian formalism, where the Hamiltonian H is a function given by a relation

$$H = \sum_i \dot{\boldsymbol{q}}_i \frac{\partial L}{\partial \dot{\boldsymbol{q}}_i} - L = \sum_i \dot{\boldsymbol{q}}_i \boldsymbol{p}_i - L. \tag{2.3}$$

Hamiltonian formalism requires $\boldsymbol{p} = \frac{\partial L}{\partial \boldsymbol{q}}$. It has to be noted, that in the equation 2.1 L is a function of generalized coordinates and generalized velocity and is defined on the configuration space. On the contrary the Lagragian in equation 2.3 is also a function of generalized coordinates, however it is not a function of the generalized velocity, but the generalized momentum. For the single in electromagnetic field, we get Hamiltonian in the following form

$$H = c\sqrt{m_0^2 c^2 + (\boldsymbol{p} - q\boldsymbol{A})^2} + q\Phi. \tag{2.4}$$

From the Hamiltonian equations of motion can be calculated with help of formulas

$$\dot{\boldsymbol{p}} = -\frac{\partial H}{\partial \boldsymbol{q}} \qquad \dot{\boldsymbol{q}} = \frac{\partial H}{\partial \boldsymbol{p}} \tag{2.5}$$

For the particular Hamiltonian given above, we get the well known the Lorentz equation of motion.

$$\frac{\mathrm{d}}{\mathrm{d}t}(\gamma m_0 \boldsymbol{v}) = \frac{\mathrm{d}\boldsymbol{p}}{\mathrm{d}t} = q(\boldsymbol{E} + \boldsymbol{v} \times \boldsymbol{B}), \tag{2.6}$$

where γ is Lorentz factor $\gamma = \frac{1}{\sqrt{1-\frac{v^2}{c^2}}} = \sqrt{1 + \left(\frac{p}{m_0 c}\right)^2}$, $\boldsymbol{E}$ is the electric field and $\boldsymbol{B}$ denotes the magnetic field.

2.2 Full orbit

The full orbit simulations are based on numerical solution of the Lorentz equation and thus reconstruct the real particle trajectory. The crucial disadvantage of this kind of simulation is that, it is computationally cost. If we assume that we would like to describe one gyration period at least by 100 point, than the characteristic time step of the simulation will be given by

$$\mathrm{d}t = \frac{T_{gyro}}{100} = \frac{2\pi}{100}\frac{\gamma m}{qB} \approx 10^{-13}\mathrm{s}, \tag{2.7}$$

where T_{gyro} is period of the Larmor gyration. From the previous equation, it is obvious that the tracing a particle for milliseconds will need tens of millions of steps. This is the fact that makes full orbit simulation computationally demanding. A large number of steps bring another difficulty. The long-lasting simulation struggles with the imperfect conservation of invariant such as energy and total momentum. To minimise this unwanted behaviour the proper integration scheme has to be chosen. The integrators that are optimize in this respect are called symplectic.

Symplecticity of the algorithm rises up from volume-preserving property. The volume-preserving property of the integration scheme means, that if the integrator is applied to a Hamiltonian system, then it preserves volume in the phase space. This particular property of the algorithm is very crucial for long-duration simulation, because ensures that errors are bounded. This property will be discussed in more details in the following sections.

As it was written in the beginning of this section, the full orbit simulations solve the Lorentz equation (2.6). A more practical form of equation (2.6) with respect to numerical simulation can be obtain by transforming the one differential equation of the second order to the two differential equations of the first order. After this transformation, the equations of motion for particle with the mass m and the charge q in electric and magnetic fields $\boldsymbol{E}(t, \boldsymbol{x})$ and $\boldsymbol{B}(t, \boldsymbol{x})$ can be written

$$\frac{\mathrm{d}\boldsymbol{x}}{\mathrm{d}t} = \boldsymbol{v}, \tag{2.8a}$$

$$\frac{\mathrm{d}(\gamma\boldsymbol{v})}{\mathrm{d}t} = \frac{q}{m}\left(\boldsymbol{E} + \boldsymbol{v} \times \boldsymbol{B}\right), \tag{2.8b}$$

where $\boldsymbol{x}$, $\boldsymbol{v}$ are respectively the position, velocity, time is t and c is the speed of light. If substitution $\boldsymbol{u} = \gamma\boldsymbol{v}$ is assumed, the system of the equations (2.8) changes into following form

$$\frac{\mathrm{d}\boldsymbol{x}}{\mathrm{d}t} = \frac{\boldsymbol{u}}{\gamma}, \tag{2.9a}$$

$$\frac{\mathrm{d}\boldsymbol{u}}{\mathrm{d}t} = \frac{q}{m}\left(\boldsymbol{E} + \frac{\boldsymbol{u}}{\gamma} \times \boldsymbol{B}\right). \tag{2.9b}$$

Here, the relativistic factor γ is given by relation $\gamma = \frac{1}{\sqrt{1+\boldsymbol{u}^2/c^2}}$. In some situations, it is more convenient to express (2.8) with help of momentum $\boldsymbol{p}$. Then the system of equations can be written as

$$\frac{\mathrm{d}\boldsymbol{x}}{\mathrm{d}t} = \frac{\boldsymbol{p}}{\gamma m}, \tag{2.10a}$$

$$\frac{\mathrm{d}\boldsymbol{p}}{\mathrm{d}t} = q\left(\boldsymbol{E} + \boldsymbol{v} \times \boldsymbol{B}\right) \tag{2.10b}$$

The velocity $\boldsymbol{v}$, which appears in the equation (2.10), could be expressed as $\boldsymbol{v} = \frac{\boldsymbol{p}}{\gamma m} = \frac{\boldsymbol{p}}{\sqrt{m^2+\boldsymbol{p}^2/c^2}}$. In this case the Lorentz factor could be written in the following from $\gamma = \sqrt{1 + \left(\frac{\boldsymbol{p}}{mc}\right)^2}$ The given forms of equation of motion are always the starting points in description of particle dynamics. In following subsections, the various method for numerical solving of the equation of motions will be given.

2.2.1 Leap-frog method

The leap frog method[3] belongs to basic methods, which are routinely used for integration of trajectories of particles. This scheme is widely used in plasma physics due to low computational cost. The premise of the leap frog method is that the calculation of the position in the n-th

time step the velocity from the time step (n-1)-th is used. Velocity and position integration leap over each other, being displaced by a half time step. Therefore this scheme is known as the leap frog pusher. This property of the leap frog method introduces little difficulty into the start of the simulation. Before start of the simulation, the velocity and position of the particle are given at the same time. In order to use the leap frog integration, the velocity or the position of the particle has to be calculated in the shifted time coordinate. The usual method is to integrate the velocity of the particle backwards through $-0.5\Delta t$, then the described method could be used. The relativistic version of the Leap frog pusher is given by following scheme.

$$\gamma_n = \frac{1}{\sqrt{1 - \frac{\boldsymbol{v}_n^2}{c^2}}} \tag{2.11a}$$

$$\tilde{\boldsymbol{E}} = \frac{q\Delta t}{m}\boldsymbol{E}_n \quad \bar{\boldsymbol{B}} = \frac{q\Delta t}{2m\gamma_n}\boldsymbol{B}_n \tag{2.11b}$$

$$\tilde{\boldsymbol{u}}_{n-\frac{1}{2}} = \frac{\boldsymbol{v}_{n-\frac{1}{2}}}{\sqrt{1 - \frac{\boldsymbol{v}^2_{n-\frac{1}{2}}}{c^2}}} \quad \tilde{\boldsymbol{u}} = \tilde{\boldsymbol{u}}_{n-\frac{1}{2}} + \tilde{\boldsymbol{E}} + \tilde{\boldsymbol{u}}_{n-\frac{1}{2}} \times \tilde{\boldsymbol{B}} \tag{2.11c}$$

$$\boldsymbol{u}_{n+\frac{1}{2}} = \tilde{\boldsymbol{u}} + \frac{[\tilde{\boldsymbol{u}} + \tilde{\boldsymbol{u}} \times \tilde{\boldsymbol{B}}] \times \tilde{\mathbf{B}}}{1 + \tilde{\boldsymbol{B}}^2} \tag{2.11d}$$

$$\boldsymbol{v}_{n+\frac{1}{2}} = \frac{\boldsymbol{u}_{n+\frac{1}{2}}}{\sqrt{1 + \frac{\boldsymbol{u}^2_{n+\frac{1}{2}}}{c^2}}} \tag{2.11e}$$

$$\boldsymbol{x}_{n+1} = \boldsymbol{x}_n + \boldsymbol{v}_{n+\frac{1}{2}}\Delta t \tag{2.11f}$$

The Leap frog pusher is widely used in particle in cell (PIC) simulations, because of the energy-conservation properties of the pusher.

2.2.2 Boris-Buneman scheme

The Boris-Buneman method [4] was the first integration scheme, which was designed to fit the requirements of the magnetised plasma physic. In particle simulation of magnetised plasma, the Boris algorithm is the standard for advancing a charged particle in electromagnetic fields. Note that the Boris algorithm is explicit for fast calculation and time-centered so it has the second order accuracy. Important feature of the Boris algorithm is the exact conservation of the total energy, if there the electric field is not presented. However, as it is typical for the numerical tools, the energy is not conserved numerically, but due to the features of this algorithm the error of the energy is bounded. The Boris-Buneman algorithm is given by following scheme

$$\gamma_n = \frac{1}{\sqrt{1 - \frac{v_n^2}{c^2}}} \tag{2.12a}$$

$$\tilde{\boldsymbol{E}} = \frac{q\Delta t}{2m}\boldsymbol{E} \quad \bar{\boldsymbol{B}} = \frac{q\Delta t}{2m\gamma_n}\boldsymbol{B} \tag{2.12b}$$

$$\boldsymbol{u} = \gamma_n \boldsymbol{v}_n \tag{2.12c}$$

$$\tilde{\boldsymbol{u}} = \boldsymbol{u}_n + \tilde{\boldsymbol{E}} \tag{2.12d}$$

$$\tilde{\tilde{\boldsymbol{u}}} = \tilde{\boldsymbol{u}} + \frac{\left(\tilde{\boldsymbol{u}} + \tilde{\boldsymbol{u}} \times \tilde{\boldsymbol{B}}\right) \times \tilde{\mathbf{B}}}{1 + \tilde{\boldsymbol{B}}^2} \tag{2.12e}$$

$$\boldsymbol{u}_{n+1} = \tilde{\tilde{\boldsymbol{u}}} + \tilde{\boldsymbol{E}} \tag{2.12f}$$

$$\boldsymbol{v}_{n+1} = \frac{\boldsymbol{u_{n+1}}}{\sqrt{1 + \frac{\boldsymbol{u}_{n+1}{}^2}{c^2}}} \tag{2.12g}$$

$$\boldsymbol{x}_{n+1} = \boldsymbol{x}_n + \boldsymbol{v}_{n+1}\Delta t \tag{2.12h}$$

The extraordinariness of the Boris algorithm lies in the characteristic division of influence of particular electro-magnetic fields. The first step of the Boris-Buneman scheme is a substitution of the velocity and the Lorentz factor. Then it accounts for half of the acceleration caused by the electric field. Subsequently, the direction of the vector of velocity is changed due to action of magnetic field. Finally, the particle is again accelerated by the second half of the electric field. As it was indicated in the previous text, the Boris-Buneman (non-relativistic) algorithm belongs to the volume preserving integrators [33]. But the relativistic variant of the Boris scheme was designed only by introducing the relativistic quantities to the existing algorithm and therefore posses the desired symplecticity.

2.2.3 Vay pusher

Another leap-frog-like integration scheme, which could be used for calculation of trajectories of particles, is algorithm introduced by Vay. The Vay algorithm [43, 42] is an alternative formulation of the Boris-Buneman scheme. This algorithm was designed to preserve cancellation of the electric and magnetic field, which could arise in the specific situation ($\boldsymbol{E}+\boldsymbol{v}\times\boldsymbol{B} = 0$). In the derivation of Boris-Buneman scheme, the following approximation is used

$$\bar{\boldsymbol{v}}_{Boris} = \frac{\boldsymbol{v}(\boldsymbol{u_i} + \frac{1}{2}\boldsymbol{E}\Delta t) + \boldsymbol{v}(\boldsymbol{u}_f + \frac{1}{2}\boldsymbol{E}\Delta t)}{2}, \tag{2.13}$$

where $\boldsymbol{u}_i$ is an initial relativistic velocity $\boldsymbol{u} = \gamma\boldsymbol{v}$ and $\boldsymbol{u}_f$ is a final velocity. The scheme proposed by Vay differs from the Boris-Buneman algorithm by the approximation given by equation (2.13). The approximation used by Vay is

$$\bar{\boldsymbol{v}}_{Vay} = \frac{\boldsymbol{v}(\boldsymbol{u}_i) + \boldsymbol{v}(\boldsymbol{u}_f)}{2}. \tag{2.14}$$

From the equation (2.14), it is obvious that Vay used the average of the velocities in derivation. This particular choice allows the equilibrium solution, e.g. $\boldsymbol{E} + \bar{\boldsymbol{v}}_{Vay} \times \boldsymbol{B} = 0$ and therefore the

Vay method satisfied the condition for steady state solution, but unlike the Boris method the Vay method is not volume preserving. The Vay method is given by following scheme:

$$\boldsymbol{v}_n = \frac{\boldsymbol{p}_n}{\sqrt{m^2 + \frac{\boldsymbol{p}_n{}^2}{c^2}}} \tag{2.15a}$$

$$\boldsymbol{p}_0 = \boldsymbol{p}_{n-\frac{1}{2}} + \frac{q\Delta t}{2}\left(\boldsymbol{E}_n + \boldsymbol{v}_{n-\frac{1}{2}} \times \boldsymbol{B}_n\right) \tag{2.15b}$$

$$\boldsymbol{p}\prime = \boldsymbol{p}_0 + \frac{q\Delta t}{2}\boldsymbol{E}_n \tag{2.15c}$$

$$\gamma\prime = \sqrt{1 + \frac{\boldsymbol{p}\prime{}^2}{m_0^2 c^2}} \tag{2.15d}$$

$$\boldsymbol{\tau} = \frac{q\Delta t}{2m_0}\boldsymbol{B}_n \tag{2.15e}$$

$$u^\star = \frac{\boldsymbol{p}\prime \cdot \boldsymbol{\tau}}{m_0 c} \tag{2.15f}$$

$$\sigma = \gamma\prime{}^2 - \boldsymbol{\tau}^2 \tag{2.15g}$$

$$\gamma_{+1/2} = \sqrt{\frac{\sigma + \sqrt{\sigma^2 + 4\left(\boldsymbol{\tau}^2 + u^{\star 2}\right)}}{2}} \tag{2.15h}$$

$$\boldsymbol{t} = \frac{\boldsymbol{\tau}}{\gamma_{+1/2}} \tag{2.15i}$$

$$s = \frac{1}{1 + \boldsymbol{t}^2} \tag{2.15j}$$

$$\boldsymbol{p}_{n+\frac{1}{2}} = s \cdot \{\boldsymbol{p}\prime + (\boldsymbol{p}\prime \cdot \boldsymbol{t}) \cdot \boldsymbol{t} + \boldsymbol{p}\prime \times \boldsymbol{t}\} \tag{2.15k}$$

$$\boldsymbol{x}_{n+1} = \boldsymbol{x}_n + \frac{\boldsymbol{p}_{n+\frac{1}{2}}}{\sqrt{m^2 + \frac{\boldsymbol{p}_{n+\frac{1}{2}}{}^2}{c^2}}}\Delta t \tag{2.15l}$$

2.2.4 Higuera-Cary pusher

Another method, which is capable to calculate the trajectory of a charged particle in the electro-magnetic field, was designed by Higuera and Cary [19]. This integration scheme have both advantages of the Boris-Buneman and the Vay method. The scheme proposed by Higuera and Cary is volume preserving and also exactly preserves equilibrium. The Higuera-Cary scheme uses an approximation, which may be written as

$$\bar{\boldsymbol{v}}_{H-C} = \boldsymbol{v}\left(\frac{\boldsymbol{u}_i + \boldsymbol{u}_f}{2}\right). \tag{2.16}$$

The Higuera-Cary method is given by following scheme:

$$\boldsymbol{\epsilon} = \frac{q\Delta t}{2m}\boldsymbol{E}_n \quad \boldsymbol{\beta} = \frac{q\Delta t}{2m}\boldsymbol{B}_n \tag{2.17a}$$

$$\boldsymbol{u}_n = \gamma_n \boldsymbol{v}_n \tag{2.17b}$$

$$\boldsymbol{u}_- = \boldsymbol{u}_n + \boldsymbol{\epsilon} \tag{2.17c}$$

$$\gamma_- = \sqrt{1 + \frac{\boldsymbol{u}_-^2}{c^2}} \tag{2.17d}$$

$$\gamma_{new}^2 = \frac{1}{2}\left(\gamma_-^2 - \boldsymbol{\beta}^2 + \sqrt{\left(\gamma_-^2 - \boldsymbol{\beta}^2\right)^2 + 4\left(\boldsymbol{\beta}^2 + |\boldsymbol{\beta}\cdot\boldsymbol{u}_-|^2\right)}\right) \tag{2.17e}$$

$$\tilde{\boldsymbol{u}} = \boldsymbol{u}_- + 2\frac{\left(\boldsymbol{u}_- + \boldsymbol{u}_- \times \frac{\boldsymbol{\beta}}{\gamma_{new}}\right) \times \frac{\boldsymbol{\beta}}{\gamma_{new}}}{1 + \left(\frac{\boldsymbol{\beta}}{\gamma_{new}}\right)^2} \tag{2.17f}$$

$$\boldsymbol{u}_{n+1} = \tilde{\boldsymbol{u}} + \boldsymbol{\epsilon} \tag{2.17g}$$

$$\boldsymbol{v}_{n+1} = \frac{\boldsymbol{u}_{n+1}}{\sqrt{1 + \frac{\boldsymbol{u}_{n+1}^2}{c^2}}} \tag{2.17h}$$

$$\boldsymbol{x}_{n+1} = \boldsymbol{x}_n + \boldsymbol{v}_{n+1}\Delta t \tag{2.17i}$$

2.2.5 Pétri implicit scheme

The Pétri scheme [32] is implicit relativistic leap-frog-like scheme, which is capable to solve the Lorentz equation for ultra-relativistic particles. However, as can be seen from the scheme (2.18), Pétri method requires the matrix multiplication. This additional computational cost is completely compensated by the implicit nature of the scheme. The scheme is especially suitable for astrophysical applications because of a very good behaviour and accuracy for ultra-relativistic motion on large time scales for spatially and temporarily varying fields. These conditions are easily met in high-energy astrophysical plasmas. The Petri algorithm is given by the set of the following equations.

$$\boldsymbol{u}_{n-\frac{1}{2}} = \gamma_{n-\frac{1}{2}} \boldsymbol{v}_{n-\frac{1}{2}} \tag{2.18a}$$

$$\alpha = \frac{q\Delta t}{m} \quad p = \frac{\alpha}{2} \quad p_{\pm} = \frac{p}{\gamma_{n\pm\frac{1}{2}}} \tag{2.18b}$$

$$\mathbf{R^n} = \begin{pmatrix} 0 & pB_z^n & -pB_y^n \\ -pB_z^n & 0 & pB_x^n \\ pB_y^n & -pB_x^n & 0 \end{pmatrix} \quad \mathbf{S^n} = \begin{pmatrix} \alpha E_x^n \\ \alpha E_y^n \\ \alpha E_z^n \end{pmatrix} \tag{2.18c}$$

$$\boldsymbol{U}_{n+\frac{1}{2}} = \left(I - \frac{\mathbf{R^n}}{\gamma^{n+\frac{1}{2}}}\right)^{-1} \left(\left(I - \frac{\mathbf{R^n}}{\gamma^{n+\frac{1}{2}}}\right) \cdot \boldsymbol{u}_{\boldsymbol{n-\frac{1}{2}}} + \mathbf{S^n}\right) \tag{2.18d}$$

$$\left(I - \frac{\mathbf{R^n}}{\gamma^{n+\frac{1}{2}}}\right)^{-1} = \frac{1}{1 + p_+^2 \boldsymbol{B}^2} \begin{pmatrix} B_x^2 p_+^2 + 1 & B_x B y p_+^2 + B_z p_+ & B_x B_z p_+^2 - B_y p_+ \\ B_x B y p_+^2 - B_z p_+ & B_y^2 p_+^2 + 1 & B_y B_z p_+^2 + B_x p_+ \\ B_x B_z p_+^2 + B_y p_+ & B_y B z p_+^2 - B_x p_+ & B_z^2 p_+^2 + 1 \end{pmatrix} \tag{2.18e}$$

$$\gamma_{n+\frac{1}{2}} = \sqrt{\frac{\sqrt{a_1^2 - 4a_2} - a_1}{2}} \tag{2.18f}$$

$$a_1 = p^2 \boldsymbol{B_n}^2 - 1 - \boldsymbol{u}_{n-\frac{1}{2}}^2 - 2\mathbf{S^n} \cdot \boldsymbol{u}_{\boldsymbol{n-\frac{1}{2}}} - \left(\mathbf{p}\boldsymbol{v}_{\mathbf{n-\frac{1}{2}}} \times \boldsymbol{B_n} + \mathbf{S^n}\right)^{\mathbf{2}} \tag{2.18g}$$

$$a_2 = -p^2 \left(\boldsymbol{B}_n^2 + \left(\left(\mathbf{S^n} + \boldsymbol{u}_{\mathbf{n-\frac{1}{2}}}\right) \cdot \boldsymbol{B}_n\right)^2\right) \tag{2.18h}$$

2.2.6 Volume preserving algorithm (VPA)

The non-relativistic Boris algorithm shows long term accuracy and this feature of this popular integrator comes from the volume-preserving property. In general, geometric numerical methods, which preserve geometric structure of the original system (in the phase space) have long-term stability and accuracy. However, the relativistic form of the Boris scheme is not preserving and does not behave well in the long-term simulation. Absence of this important property of the integrator comes from complexity of the relativistic equations of motion.

Design of the relativistic integrator with volume preserving property is much more difficult than construction of the integrator in the non-relativistic case. Construction of the VPA cannot be based only on intuition or on time the centred method. A systematic procedure is needed. One of the options is a systematic splitting method. The splitting method consists of three steps:

1. to split the original system into several incompressible subsystems,
2. to find a volume preserving algorithm for each subsystem,
3. to combine the sub-algorithms into desired VPA for the original system.

If we introduce the phase space variable $z = (\boldsymbol{x}, \boldsymbol{p})$ and the vector field of the right hand side of the system of equations (2.10) $\boldsymbol{F}(z, t)$, then from the Liouville's theorem following condition can be derived

$$\nabla_z \cdot \boldsymbol{F} = \nabla_{\boldsymbol{x}} \cdot \frac{\boldsymbol{p}}{\sqrt{m^2 + \boldsymbol{p}^2/c^2}} + \nabla_{\boldsymbol{p}} \cdot q\left(\boldsymbol{E}(\boldsymbol{x}, t) + \frac{\boldsymbol{p}}{\sqrt{m^2 + \boldsymbol{p}^2/c^2}} \times \boldsymbol{B}(\boldsymbol{x}, t)\right) = 0. \tag{2.19}$$

This condition is often called condition of incompressibility and from this condition follows that solution of the equation $\phi_t : z(t_0) \to z(t)$ preserves volume of the phase space $V(t)$, i. e.

$$\frac{\mathrm{d}V}{\mathrm{d}t} = \int_{D(t)} \nabla_z \cdot \boldsymbol{F} \mathrm{d}\boldsymbol{z} = 0, \tag{2.20}$$

where $D(t)$ denotes the integral region, defined by a fixed set of particles in the phase space. As it was mentioned earlier, one way how to design a volume-preserving algorithm is a splitting technique. This technique is applicable, when vector field $\boldsymbol{F}(\boldsymbol{z}, t)$ can be split into incompressible systems S_i. Due to the simplicity of the subsystems, the volume-preserving algorithm ϕ_i can be easily found for each subsystem S_i. Finally, the desired volume-preserving algorithm is obtained by combination of all ϕ_i. The volume-preserving scheme, which was obtain by this procedure, can be given by a set of equations [46]

$$\boldsymbol{x}_{n+\frac{1}{2}} = \boldsymbol{x}_n + \frac{\Delta t}{2m} \frac{\boldsymbol{p}_n}{\sqrt{1 + \left(\frac{\boldsymbol{p}_n}{mc}\right)^2}} \tag{2.21a}$$

$$\tilde{\boldsymbol{p}} = \boldsymbol{p}_n + \frac{q\Delta t}{2} \boldsymbol{E}_{n+\frac{1}{2}} \tag{2.21b}$$

$$\tilde{\tilde{\boldsymbol{p}}} = \mathrm{Cay}\left(\frac{q\Delta t}{2m} \frac{\tilde{B}_{n+\frac{1}{2}}}{\sqrt{1 + \left(\frac{\tilde{\boldsymbol{p}}}{mc}\right)^2}}\right) \cdot \tilde{\boldsymbol{p}} \tag{2.21c}$$

$$\boldsymbol{p}_{n+1} = \frac{q\Delta t}{2} \boldsymbol{E}_{n+\frac{1}{2}} \tag{2.21d}$$

$$\boldsymbol{x}_{n+1} = \boldsymbol{x}_{n+\frac{1}{2}} + \frac{\Delta t}{2m} \frac{\boldsymbol{p}_{n+\frac{1}{2}}}{\sqrt{1 + \left(\frac{\boldsymbol{p}_{n+1}}{mc}\right)^2}} \tag{2.21e}$$

$$\tilde{B} = \begin{pmatrix} 0 & B_3 & -B_2 \\ -B_3 & 0 & B_1 \\ B_2 & -B_1 & 0 \end{pmatrix} \tag{2.21f}$$

Here the matrix transformation denoted as *Cay* could be written as

$$Cay(A) = (I - A)^{-1}(I + A), \tag{2.22}$$

where I is a unity matrix. Integration of the equations of motion by this VPA involves calculation of the inverse matrix, this fact makes the scheme relatively computational demanding. On the other hand, the VPA is suitable for long term simulation. *Cay* transform can be replaced by its Taylor expansion but this approximation is a source of errors.

2.3 Guiding centre

In some cases, the movement of a charged particle in electromagnetic field can be treated as the superposition of the fast circular motion around a point called guiding centre and relatively slow drift of the guiding centre. According to the previous, the position of the particle $\boldsymbol{x}$ could be decomposed into two components - the position of the guiding centre $\boldsymbol{X}$ and the position of the point $\boldsymbol{\rho}$, which gyrates around the guiding centre

$$\boldsymbol{x} = \boldsymbol{X} + \boldsymbol{\rho}. \tag{2.23}$$

The guiding centre description of the particle motion is possible only under some assumptions, which guarantee the validity of this approach. First assumption relates to the electromagnetic field time scale T and states that this characteristic time scale of the electromagnetic field T has to be much longer than the particle gyro-period T_{gyro}

$$\frac{T_{gyro}}{T} \ll 1. \tag{2.24}$$

Another assumption is that the electromagnetic field length scale L has to be much larger than the gyro-radius $\rho = |\boldsymbol{\rho}|$

$$\frac{\rho}{L} \ll 1. \tag{2.25}$$

The particle displacement in one gyro-period along $\hat{\boldsymbol{b}} = \frac{\boldsymbol{B}}{B}$ has to be small compared to the electro-magnetic field parallel variation length scale $L_{\|}$

$$\frac{l_{\|}}{L_{\|}} \ll 1, \tag{2.26}$$

where $l_{\|}$ can be estimated from equation $l_{\|} = \frac{2\pi|p_{\|}|}{|q|B}$. The last condition, which has to be satisfied, reads

$$\frac{|E_{\|}|}{E_{\perp}} \approx \frac{\rho}{L} \ll 1, \tag{2.27}$$

where $E_{\|}$ and $E_{\perp}$ are defined as $E_{\|} = \boldsymbol{E} \cdot \hat{\boldsymbol{b}}$ and $E_{\perp} = |\boldsymbol{E} - E_{\|}\hat{\boldsymbol{b}}|$. This condition is related to the guiding centre self-consistency. The dynamics in momentum space behaves differently in the direction along the magnetic field than in the perpendicular one. The perpendicular component of the momentum varies rapidly due to the cyclotron motion, whereas the component parallel to the magnetic field of the momentum changes slowly. Thus, the momentum of the particle can be decomposed to its parallel and perpendicular components

$$\boldsymbol{p} = p_{\|}\hat{\boldsymbol{b}} + \boldsymbol{p}_{\perp}, \tag{2.28}$$

where $\hat{\boldsymbol{b}}$ is a unit vector parallel with respect to the magnetic field. If we chose orthogonal basis $\{\, \hat{\boldsymbol{e}}_1, \hat{\boldsymbol{e}}_2 \,\}$ which satisfies $\hat{\boldsymbol{b}} \times \hat{\boldsymbol{e}}_{1,2} = 0$, than we can expressed the perpendicular momentum as

$$\boldsymbol{p}_{\perp} = p_{\perp}\left(-\sin\theta\hat{\boldsymbol{e}}_1 + \cos\theta\hat{\boldsymbol{e}}_2\right), \tag{2.29}$$

where θ denotes a gyro-angle. Defining the pitch $\xi = \frac{p_\parallel}{p}$ or in other words the cosine of the pitch angle. The momentum may be written

$$\boldsymbol{p} = \xi p \hat{\boldsymbol{b}} + \sqrt{1-\xi^2} p \left(-\sin\theta \hat{\boldsymbol{e}}_1 + \cos\theta \hat{\boldsymbol{e}}_2\right), \tag{2.30}$$

which allows us to describe the dynamic of the particle by different variables. The guiding centre description of the particle dynamics is associated with an adiabatic invariant μ. The adiabatic invariant means, that the quantity stays constant in slowly varying field (spatially and temporarily). In particular magnetic moment μ is defined as

$$\mu = \frac{p_\perp^2}{2mB} = \frac{(1-\xi^2)p^2}{2mB}, \tag{2.31}$$

where m is the mass of particle and B is the magnitude of the magnetic field. The guiding centre approximation of the particle motion uses quantity μ to reduce number of variables, which are needed for the description of the particle motion, because this quantity is almost constant during the particle motion, i.e. $\dot{\mu} = 0$. Although the fast gyration around the field line is omitted, the information about the momentum perpendicular to the field line is hidden in adiabatic invariant μ.

The dynamics of the guiding centre can be calculated from the following set of equations [41]

$$\begin{aligned}
\dot{\boldsymbol{X}} &= \frac{1}{B_{\parallel^*}}\left(\boldsymbol{E}\times\hat{\boldsymbol{b}} - p_\parallel \frac{\partial \hat{\boldsymbol{b}}}{\partial t}\times\hat{\boldsymbol{b}} + \frac{m\mu\hat{\boldsymbol{b}}\times\nabla B + p_\parallel \boldsymbol{B}^*}{m\gamma}\right),\\
\dot{p}_\parallel &= \frac{\boldsymbol{B}^*}{B_\parallel^*}\left(\boldsymbol{E} - p_\parallel\frac{\partial\hat{\boldsymbol{b}}}{\partial t} - \frac{\mu\nabla B}{\gamma}\right),\\
\dot{\mu} &= 0,\\
\dot{\theta} &= \Omega,
\end{aligned} \tag{2.32}$$

where is $\boldsymbol{X}$ is the position of the guiding centre, $p_\parallel$ is the parallel momentum, μ is a magnetic moment and θ is a gyro-angle of the particle. The equations are independent on gyro-angle θ, which is undesired for the guiding centre description. The equation for the gyro-angle θ is kept there only for completeness. The effective magnetic field $\boldsymbol{B}^*$, which appears in equations (2.32) is given by

$$\boldsymbol{B}^* = \boldsymbol{B} + \frac{p_\parallel}{q}\nabla\times\hat{\boldsymbol{b}}, \tag{2.33}$$

where q denotes a charge of particle. The Lorentz factor is in the guiding centre variables expressed as

$$\gamma = \sqrt{1+\left(\frac{p}{mc}\right)^2} = \sqrt{1+\left(\frac{p_\parallel}{mc}\right)^2 + \frac{2\mu B}{mc^2}}. \tag{2.34}$$

If we assume the magnetic field independent of time, the equations (2.32) could be written in a more compact form

$$\begin{aligned}
\dot{\boldsymbol{X}} &= \frac{p_{\parallel}}{\gamma m}\frac{\boldsymbol{B}^*}{B^*_{\parallel}} + \boldsymbol{E}^* \times \frac{\hat{\boldsymbol{b}}}{B^*_{\parallel}} \\
\dot{p}_{\parallel} &= q\boldsymbol{E}^* \cdot \frac{\boldsymbol{B}^*}{B^*_{\parallel}} \\
\dot{\mu} &= 0 \\
\dot{\theta} &= \Omega.
\end{aligned} \tag{2.35}$$

Than the effective fields $\boldsymbol{E}^*$ and $\boldsymbol{B}^*$ are given by formulas

$$\begin{aligned}
\boldsymbol{B}^* &= \boldsymbol{B} + \frac{p_{\parallel}}{q}\nabla \times \hat{\boldsymbol{b}}, \\
\boldsymbol{E}^* &= \boldsymbol{E} - \frac{\mu}{\gamma q}\nabla B
\end{aligned} \tag{2.36}$$

The sets of equations (2.32), (2.35) are usually solved by one of Runge-Kutta methods. Due to the fact that the equations are solved by one of the Runge-Kutta methods, the numerical method causes the error growth, because Runge-Kutta methods are not volume-preserving. This complicates the performance of this approach in the long simulation.

Before we start the calculation of the particle trajectory using the guiding center technique, we have to determine the position of the guiding center $\boldsymbol{X}$ ($= \boldsymbol{x}^{GC}$). Furthermore, during the transformation from the full orbit description to the guiding center, it needs to be considered, that the quantities like the total energy and the magnetic moment have to be conserved and equal in the both cases. For these reasons, the variables appearing in equations (2.32) and (2.35) have to be recalculated by relations [30]

$$\begin{aligned}
\boldsymbol{x}^{GC} &= \boldsymbol{x} - \frac{\boldsymbol{B}}{qB^2} \times \boldsymbol{p} \\
p_{\parallel}^{GC} &= \frac{1}{p_\phi b_\phi}\left(Rp_\phi + q\left(\Psi - \Psi^{GC}\right)\right) \\
\mu^{GC} &= \frac{E_0}{2B^{GC}}\left\{\left[\gamma + \frac{q}{E_0}\left(\Phi - \Phi^{GC}\right)\right]^2 - \left[1 + \left(\frac{p_{\parallel}^{GC}}{mc}\right)^2\right]\right\}
\end{aligned} \tag{2.37}$$

where the variables considered in the guiding center are denoted by $*^{GC}$. In these equations, the cylindrical coordinates system is adopted. R is the radial position of the particle, p_ϕ is the toroidal momentum, b_ϕ is the toroidal component of the unit vector of magnetic field. Ψ is a poloidal magnetic flux and Φ is the potential of the electric field.

Chapter 3

Implementation of the algorithm

In the following chapter the description of the implementation of the algorithm for calculation of the particle trajectories will be given. First of all theory behind the reconstruction of the magnetic and electric field will be briefly summarized. The interpolation techniques and used transformations in the simulations will be also discussed. Finally, the work-flow of the program is given.

3.1 Reconstruction of magnetic and electric field

The magnetic field of the tokamak COMPASS is reconstructed by the EFIT code. The EFIT allows the reconstruction of the equilibrium magnetic field by solving Grad-Shafranov equation. The basic inputs into the reconstruction of magnetic field are tokamak geometry, currents in the poloidal field coils and various magnetic measurements. The EFIT code reconstruct the equilibrium magnetic field by solving Grad-Shafranov equation, which may be written

$$R\frac{\partial}{\partial R}\left(\frac{1}{R}\frac{\partial \Psi}{\partial R}\right)+\frac{\partial^2 \Psi}{\partial Z^2}=-\mu_0 R^2\frac{\partial p(\Psi)}{\partial \Psi}-F(\Psi)\frac{\partial F(\Psi)}{\partial \Psi}, \tag{3.1}$$

where Ψ is the poloidal magnetic flux, μ_0 is permeability of the vacuum, p is the pressure of the plasma and F is a function of the magnetic toroidal flux (see (3.4)). The poloidal magnetic flux is defined as

$$\Psi(R,Z)=RA_\phi(R,Z), \tag{3.2}$$

where A_ϕ is the toroidal component of the magnetic vector potential, which is related to the magnetic field $\boldsymbol{B}$ via the equation

$$\boldsymbol{B}=\nabla\times\boldsymbol{A}. \tag{3.3}$$

With the knowledge of the reconstructed poloidal magnetic flux by the EFIT code and with relation (3.3), the magnetic field can be calculated from the following equation

$$\boldsymbol{B}=\frac{1}{2\pi R}\left(-\frac{\partial \Psi}{\partial Z},F(\Psi),\frac{\partial \Psi}{\partial R}\right). \tag{3.4}$$

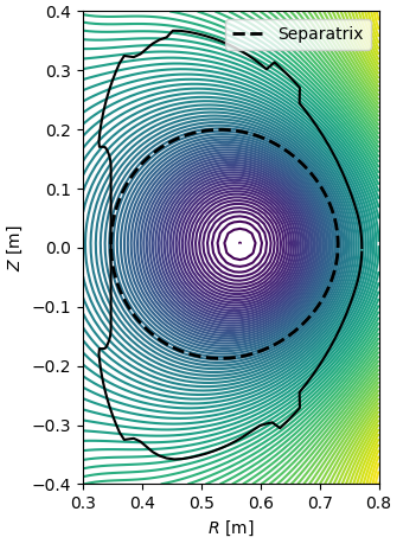

Figure 3.1: Example of the contour plot of the poloidal flux Ψ, which visualises the plasma configuration.

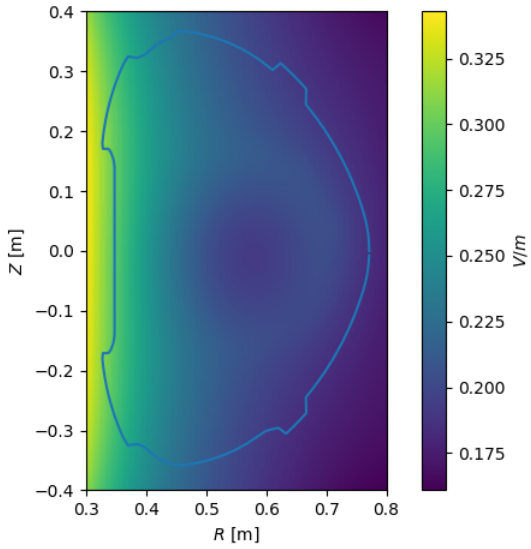

Figure 3.2: The figure displays the magnitude of the toroidal electric field E_ϕ.

From the poloidal magnetic flux, not only the magnetic field but also the electric field can be calculated. The calculation of the electric field can be performed by the time derivative of the poloidal magnetic flux

$$\boldsymbol{E} = -\nabla\varphi - \frac{\partial \boldsymbol{A}}{\partial t} \quad \rightarrow \quad E_\phi = \frac{1}{R}\frac{\partial \Psi}{\partial t}. \tag{3.5}$$

3.2 Transformation of coordinates

Transformation between different coordinate system is an important thing, because some expressions are easier to obtain in different coordinate system. In the implemented algorithm, calculations of the particle trajectories are carried out in Cartesian coordinates system. However, as can be seen from the equation (3.4), the reconstructed magnetic field is given in cylindrical coordinates. For this reason, the magnetic field is transformed from coordinate system (R, ϕ, z) transform into (x, y, z). For the conversion between cylindrical and Cartesian coordinates, it is convenient to assume, that the z-axis is the same in both coordinates systems. The correspondence between cylindrical and Cartesian coordinate system could be written

$$\begin{aligned} x &= R\cos\phi \\ y &= R\sin\phi \\ z &= z \end{aligned} \tag{3.6}$$

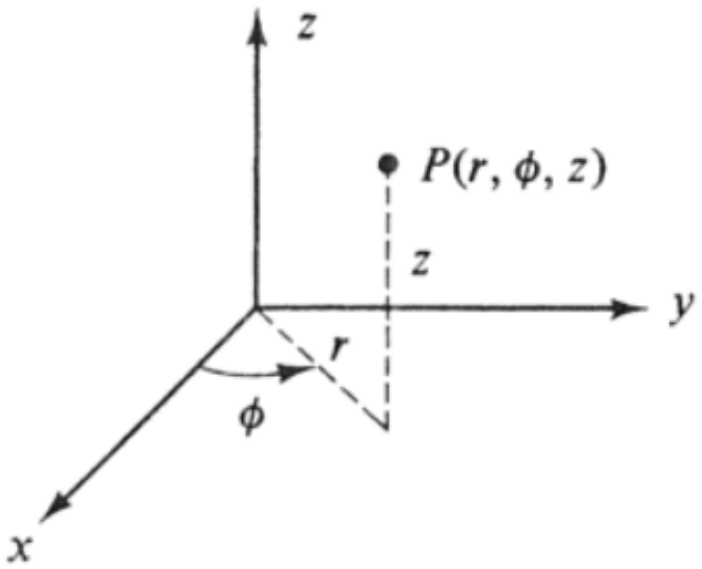

Figure 3.3: Cylindrical coordinates system.

and in the opposite direction

$$\begin{aligned} R &= \sqrt{x^2 + y^2} \\ \phi &= \arctan \frac{y}{x} \\ z &= z. \end{aligned} \tag{3.7}$$

The basis vectors of the cylindrical coordinates system are given by

$$\hat{\boldsymbol{r}} = (\cos\phi, \sin\phi, 0), \qquad \hat{\boldsymbol{\phi}} = (-\sin\phi, \cos\phi, 0), \qquad \hat{\boldsymbol{z}} = (0, 0, 1). \tag{3.8}$$

The knowledge of the mentioned basis vectors is convenient in situations, where we would like to calculate a projection of the particular vector in the direction of basis vectors. For the transformation of the vector fields, the transformation (3.6) cannot be used. Instead of (3.6), the following transformation has to be used:

$$\begin{pmatrix} A_x \\ A_y \\ A_z \end{pmatrix} = \begin{pmatrix} \cos\phi & -\sin\phi & 0 \\ \sin\phi & \cos\phi & 0 \\ 0 & 0 & 1 \end{pmatrix} \begin{pmatrix} A_r \\ A_\phi \\ A_z \end{pmatrix} \tag{3.9}$$

3.3 Interpolation of the fields

One of the most popular and useful representation of curves or other geometrical objects is a spline. A spline of the order n is a function defined piecewise by polynomials of a degree $n - 1$, generally, a smooth curve interpolated among given control points. B-splines of order n are basis functions for spline functions of the same order defined over the same control points. This means that all spline functions can be constructed by a linear combination of B-splines.

B-spline is defined by a set of coefficients α_i, a knot vector (vector of control points) $\boldsymbol{T} = \{t_j\}$ and a degree n, where $i = 0, 1, \ldots, p-1$, $j = 0, 1, \ldots, m$ and $m = p + n + 1$. The knot vector $\boldsymbol{T}$ is a set of non-decreasing values $t_k < t_{k+1}$. Usefulness of B-splines lies in the fact, that any spline function of order n can be expressed as a linear combination of B-splines on a given set of points:

$$S_{n,t}(x) = \sum_i \alpha_i B_{i,n}(x). \tag{3.10}$$

The splines interpolate between the points with the help of the basis functions. Any point on the curve is obtained by summing multiplications of control coefficients α_i and the basis functions $B_{i,n}$. The basis functions can be calculated from the expression:

$$\begin{aligned} B_{i,n}(x) &:= \begin{cases} 1 & \text{if} \quad t_i \leq x < t_{i+1} \\ 0 & \text{otherwise} \end{cases} \\ B_{i,k}(x) &:= \frac{x - t_i}{t_{i+k} - t_i} B_{i,k-1}(x) + \frac{t_{t+k+1} - x}{t_{t+k+1} - t_{i+1}} B_{i+1,k-1}(x) \end{aligned} \tag{3.11}$$

The above mentioned algorithm is called The Coax-de Boor formula. By this formula, it is possible to recursively calculate the basis functions $B_{i,n}$. It is known that the sum of the basis functions $B_{i,k}(x)$ is equal to one. The sum of $B_{i,k}(x)$ in the interval $k - n \leq i < k$ equals one as well, where $x_k \leq x < x_{k+1}$. It means that all basis functions outside the interval $k - n \leq i < k$ are zero, because any basis function is always non-negative. So the calculation of all basis function is not necessary. Less computationally demanding algorithm for calculation of the basis function than the Coax-de Boor algorithm is the inverted triangular scheme (ITS). Efficiency of this particular scheme lies in the fact that it does not compute all basis functions as the Coax-de Boor algorithm, but only these which are non-zero. The inverted triangular scheme may be written as

$$\begin{aligned} B_{i-j,k}(x) = \frac{L_{j+1}}{R_j + L_{j+1}} B_{i-j,p-1}(x) \quad + \quad \frac{R_{j+1}}{R_{j+1} + L_j} B_{i-j+1,k-1}(x) \\ L_j = x - t_{i+1-j} \qquad R_j = t_{i+j} - x \end{aligned} \tag{3.12}$$

The inverted triangular scheme was implemented in the Python environment. The interpolation routines based on the B-splines are already implemented in the standard Python modules, but interpolation routine is not available in the Python module Numba, which was used for implementation of the simulation code, because enables acceleration of the computation. The module Numba works by generating optimized machine code using LLVM compiler infrastructure at import the time, runtime or statically. Numba supports compilation of Python to run either on CPU or GPU hardware. The main aim of the implementation of interpolation in Numba module is time efficiency and fact that the routine could be easily adjust to run on GPU. The GPU version of the routine could be in the future used for simulation of large number of particles on GPU cards.

The knots and coefficients of the splines, which are needed for spline evaluation, can be calculated by Python routines present in the standard packages (*scipy.inrepolate*). This is done only once and so this calculation does not need any additional optimization. Input parameters of

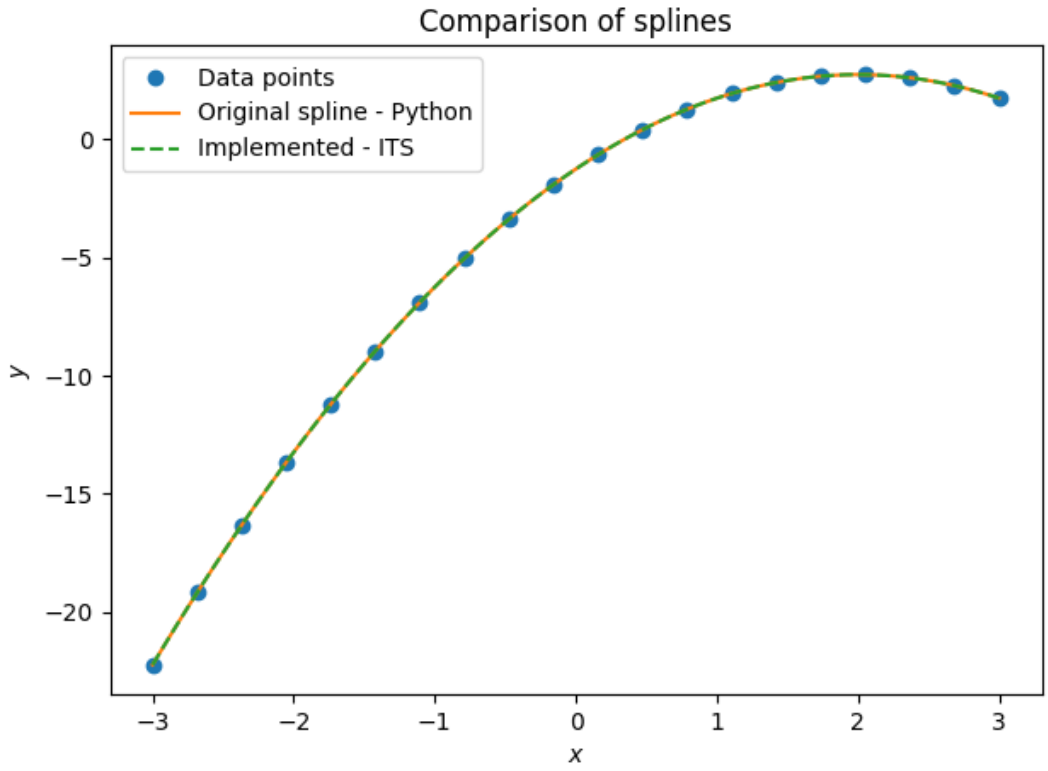

Figure 3.4: Comparison of different spline techniques. The orange line denotes the spline interpolation given by function implemented in Python package (*scipy.interpolate*). The dashed green line is calculated by the implemented ITS algorithm. The blue points represent the function, which has to be interpolated. The implemented ITS scheme gives exactly the same values as the original Python routine.

the implemented function are a vector of knots, the coefficients of the spline, order of the spline and of course the points of interests, i.e. the point, where the function has to be interpolated.

3.4 Normalization of quantities

For long term stability and for reduction of the errors, which arise from the finite precision of a computation involving a floating-point or a integer values, the normalisation of the quantities is usually applied. For the proper normalization one can start with the Lorentz equation (2.6), where we replace all variables by product of dimensionless variables and its characteristic scale, eg. $\boldsymbol{v} = v_0\bar{\boldsymbol{v}}$, where $\bar{\boldsymbol{v}}$ is dimensionless velocity and v_0 the characteristic velocity. After the substitution of all variables, we get the Lorentz equation in the following form

$$\frac{m_0 v_0}{t_0}\bar{m}\frac{\mathrm{d}\bar{\boldsymbol{v}}}{\mathrm{d}\bar{t}} = q_0 E_0 \bar{q}\bar{\boldsymbol{E}} + q_0 v_0 B_0 \bar{q}\bar{\boldsymbol{v}} \times \bar{\boldsymbol{B}}. \tag{3.13}$$

From the equation (3.13) two conditions follow which have to be satisfied

$$\frac{m_0 v_0}{t_0} = q_0 E_0\,, \tag{3.14}$$

$$\frac{m_0 v_0}{t_0} = q_0 v_0 B_0\,. \tag{3.15}$$

Due to the fact, that we are interested in the dynamics of relativistic electrons, the natural choices for variables are:

$$\begin{aligned} m_0 &= m_e\,, \\ v_0 &= c\,, \\ q_0 &= e\,. \end{aligned} \tag{3.16}$$

The B_0 and E_0 can be calculated from (3.14), (3.15), where t_0 can be chosen arbitrary. Is is convenient to chose the t_0 as a time step of the simulation.

3.5 Domain check

In order to determine the realistic particle trajectories, we have to keep in mind that there exists a constraint on the particle position. At all times of the simulation the particle has to be in the device. Therefore an algorithm, which is capable to identify whether the particle is within the device or whether it has already collided with wall is needed.

An simple method is one of the ray casting methods, which is usually used in computer graphics and computational geometry. These methods are capable to find an intersection of two curves and thus determine whether the point is located inside or outside of the given curve.

For example one simple way how to decide whether the point is inside or outside the given polygon is to test how many times a ray, which starts from the point and goes in any direction, intersects the edges of the polygon. If the point is in the polygon then it will intersect the edge an odd number of times. However, if the point is outside of the polygon then it will intersect the edge an even number of times.

3.6 Program workflow

In the third chapter, the schemes for integration of the equation of motion were presented, most of these algorithms were implemented and are capable to describe well the particle dynamics. To be able to get magnetic field data for every point in the COMPASS tokamak, the discrete data, which are loaded from the COMPASS database and then are recalculated, has to be interpolated. The interpolation is done by standard Python routines or by a routine, which was briefly described in the section 3.3.

All schemes for solving the particle motion in the electromagnetic fields are made in the Cartesian coordinate system. However, the tokamak posses the toroidal symmetry and the description of the magnetic field of the tokamak is preferred in the cylindrical coordinates. The magnetic data are stored in the COMPASS database in cylindrical coordinates, so the transformations of coordinates have to be done (see section 3.2).

Another very important part of the simulation algorithm is the domain check (section 3.5) and the normalization procedure. In each step of the algorithm, after calculation of the new position and velocity, the domain check has to be performed to determine whether the simulated particle is still in the allowed area, i.e. inside the vacuum vessel. For better numerical accuracy is convenient to normalize variables, which act in the integration scheme. This is discussed in the section 3.4.

The programme works as follows:

- Read input data, which contain the total time of the simulation T, the time step Δt, the initial energy $\mathcal{E}$, the initial pitch ξ, the initial position. The user has to specify the number of the shot from the COMPASS database and time in which the topology of the magnetic field should be reconstructed.
- Reconstruct the desired magnetic field and calculate the splines. The input data are stored and the memory needed for the simulation is allocated. The velocity is calculated in the mid-step if the leap-frog like scheme is used for integration of the equations of motion.
- Start the integrator and run until it reaches T or the traced particle is out of the tokamak interior.
- Take one step with the integrator and calculate new position and velocity of the particle for the time $t + \Delta t$.
- Check if the new position of the particle is inside the allowed domain.
- If yes, repeat until T is reached. Then write a solution data to file.
- If no, exit the calculation with a message saying that the particle hits the wall and write the solution data to the file.

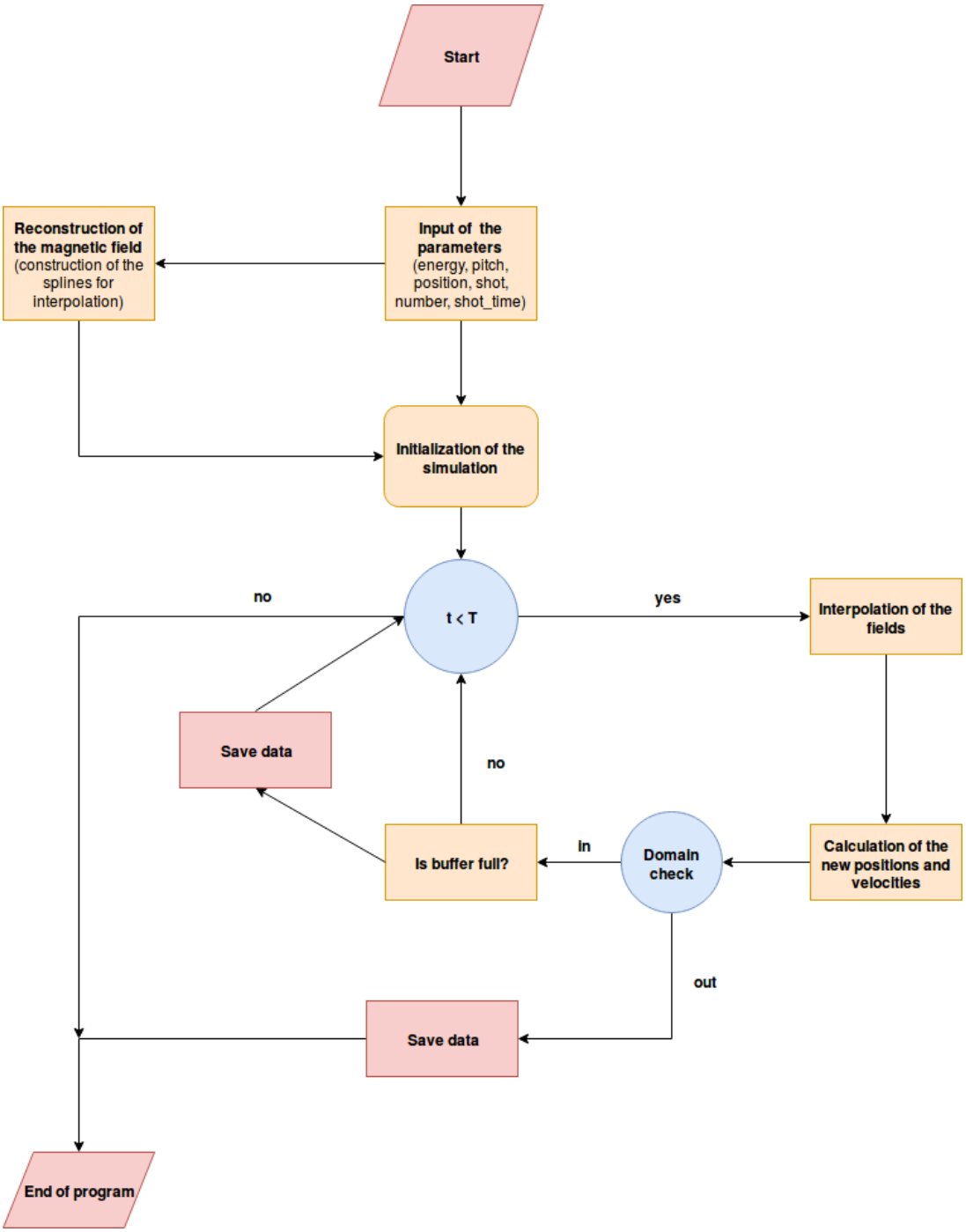

Figure 3.5: Flow chart of the program for simulation of the particle dynamics.

Chapter 4

Simulation of the RE trajectories in the COMPASS tokamak

In this chapter, the results of simulation of the trajectories of runaway electrons are presented together with the implication for measurements with the Cherenkov detector. Moreover, overview of modeling efforts in characterisation of runaway electrons in the COMPASS tokamak is given.

4.1 COMPASS tokamak

The COMPASS (COMPact ASSembly) tokamak [29] is one of two tokamaks, which are located in the Czech Republic. The COMPASS tokamak was build and operated in 1990s at Culham in the United Kingdom under name COMPASS-D. In 2006, it replaced the CASTOR tokamak, which has been operated at the Institute of Plasma Physics of the Czech Academy of Sciences since 1977. The name of the old tokamak CASTOR is an abbreviation of the words Czechoslovakak Academy of Sciences TORus. The CASTOR tokamak was build in the 60s in the Soviet Union and named TM1. Currently, the CASTOR tokamak is operated as GOLEM tokamak at the Faculty of Nuclear Sciences and Physical Engineering of the Czech Technical University in Prague and serves especially as an education device for students or tested bend for developing of new diagnostics.

The COMPASS tokamak belongs due to its size to medium size tokamaks, which are capable of so called H-mod (hight confinement mode). The unique features of this facility is a ability to achieve ohmic H-mode, H-mode without additional heating power. The COMPASS tokamak is capable to sustain plasma in various configurations as a D-shape or SND (single null divertor). This ability and its size makes it very important for scaling experiments. The scientific program of the tokamak is mostly focused on the physics of the plasma edge and the plasma wall interaction. The COMPASS tokamak benefits from its size also during runaway electron experiments, because it can be operated without any worries about damage of the device. The main parameters of the COMPASS tokamak are summarized in the Tab. 4.1.

Parameters		**Values**
Major radius	R [m]	0.56
Minor radius	a [m]	0.23
Maximal plasma current	I_p^{max} [kA]	400
Magnetic field	B [T]	0.9-1.6
Vacuum pressure	p_{vac} [Pa]	$1 \cdot 10^{-6}$
Elongation	ϵ	1.8
Plasma shape	-	D, SND, elipse, circular
Pulse length	t [s]	< 1

Table 4.1: Main parameters of the COMPASS tokamak.

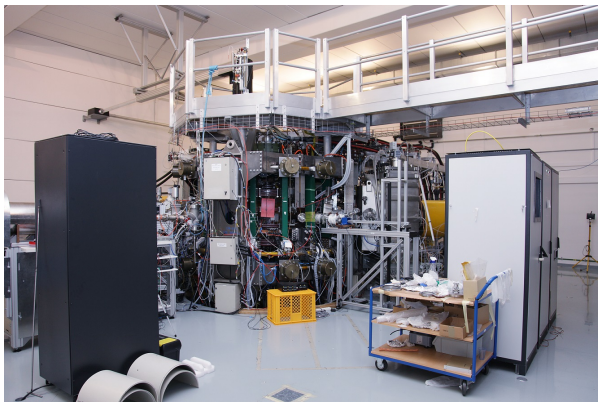

Figure 4.1: The COMPASS tokamak.

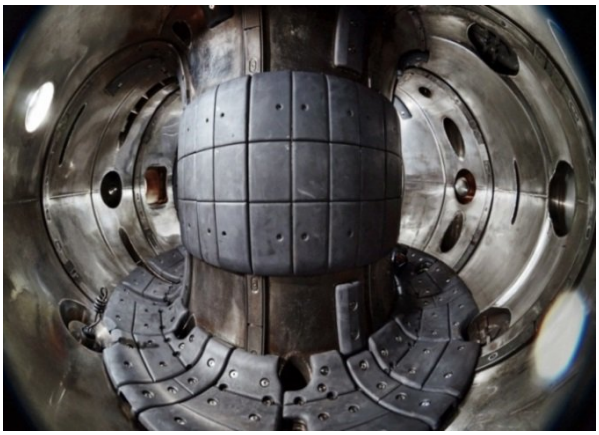

Figure 4.2: View of the chamber interior of the COMPASS tokamak.

4.2 Modeling of runaway electrons in the COMPASS tokamak

Attempts to model behaviour of the runaway electrons (RE) in the COMPASS tokamak are currently in the initial phase. A method, which estimates runaway current in flattop phase of plasma discharges, was tested on COMPASS discharges dedicated to investigation of runaway electrons [25]. This method assumes, that plasma current I_P consists of three parts: ohmic current I_Ω, bootstrap current I_{Boot}, this is self- induced current driven by magnetization drift of trapped electrons, and current, which is carried by runaway electrons I_{RE}. The value of the current carried by runaway electrons is determined from the relation

$$I_{RE} = I_p - I_{Boot} - I_\Omega = I_p - I_{Boot} - \frac{U_{loop} - L_p \mathrm{d}I/\mathrm{d}t}{R}, \tag{4.1}$$

where $L_p = \frac{\mu_0 R_0 l_i}{2}$ denotes plasma inductance, l_i is itself inductance, R_0 and R are major radius and plasma resistance respectively. The method uses fast transport code METIS [40], which is capable to reconstruct the evolution of the profiles of various quantities during the plasma discharge from measured quantities using scaling laws and transport equations. Outputs from this transport solver can be easily evaluated against experimental observations. This method was found to be very sensitive to U_{loop} and fast dynamic changes.

An extensive efforts in the runaway electron modeling are concentrated on coupling of the fast transport solver METIS and 1-D + 2-V relativistic bounce-average kinetic Fokker-Planck solver LUKE [27]. The LUKE code is capable to compute many important features of the RE dynamics as avalanche source of RE, radiation losses, radial transport with phase space dependence and trapping effects. Coupling of the METIS and LUKE allows to calculate a self-consistent, time and spaced resolved distribution function and an improved evolution of the plasma profiles.

4.3 Trajectories of the particles

In this chapter, the basic output of the programme, which is capable to calculate the trajectories of the particles, will be shown. The particles are divided into two groups due to features of their trajectories. The first group represents the passing particles. The passing particles have a sufficiently large velocity parallel to the magnetic field and circulate continuously around the torus. The other group of particles is called the trapped particles. These particles are trapped on outer side of the torus by the magnetic mirrors, which are formed due to the gradient of the toroidal magnetic field.

From the point of view of the runaway physics, the passing particles are the particles, which can be continuously accelerated by the toroidal electric field and thus can gain relativistic velocities. On the other hand, trapped electrons experiencing the strong electric field can also run away, but not immediately [28]. Indeed, their parallel velocity does not increase over one bounce period sufficiently, where the bounce period is the time it takes a particle to move back and forth between the two mirror points. However, they do pinch towards the tokamak center.

The movement towards the center is called Ware pinch [45] and the velocity of this movement can be expressed as

$$v_{Ware} = -\frac{E_\phi}{B_\theta}, \tag{4.2}$$

where E_ϕ is the magnitude of the toroidal electric field and B_θ denotes magnitude of the poloidal magnetic field. So the initially trapped electrons, which can be created by knock on collision or by interaction with the EC waves, will move inward until they fulfil the detrapping condition. The real situation is more complicated, because the detrapping of electrons is also caused by collisions, but it can be shown that the pinch dettraping is more effective than the effect of collisions. The trapped electrons due to their larger pitch emit energy via the synchrotron radiation. This could also caused faster detrapping.

For illustrations of the different trajectories of electrons six particles with various energies and pitch angles were simulated. The particles were tracked from the same initial position $r = 0.7$ m and $z = 0$ m. The energies of the electrons were 100 keV, 1 MeV and 10 MeV. The pitch $\xi = \frac{v_\parallel}{v}$ was chosen to be 0.9 and 0.5. The electrons with $\xi = 0.9$ are passing particles and electrons with $\xi = 0.5$ are mostly trapped particles. As can be seen in figure 4.4, the electrons with $\xi = 0.5$ and energies 100 keV, are on banana orbits. However, the electron with energy 10 MeV has already sufficiently large component of velocity parallel to the magnetic field and is passing again. The reason why is the electron passing is that the deviation from the original flux surface is large and the electrons is moving only in the low magnetic field, where cannot be trapped.

The figures of the poloidal projections of the particle orbits are shown in figures 4.3, 4.4. The figure 4.3 shows poloidal trajectories of the passing particles with the different energies. As is clearly visible from this figure, the less energetic particles remain on the same flux surface. However, for energetics particles the deviation from the initial flux surface is visible. The influence of the particle energy on the size of the Larmor radius is also clear.

On the other hand, in the figure 4.4, the poloidal projections of the trajectories of mostly trapped electrons are shown. The effect of the energy of particles on their trajectories is also clear. With the increasing energy of the particle, the width of the banana orbit is also increasing. From the figure, it is also clear, that the banana orbit is closing in the direction to the center of tokamak. The drift, which is responsible for the shape of the banana orbit trajectories, is the ∇B drift given by formula

$$\boldsymbol{v}_{\nabla B} = \frac{m v_\perp^2}{2qB} \frac{\boldsymbol{B} \times \nabla B}{B^2}, \tag{4.3}$$

where q is a charge of the particle. If we realize that the strength of the magnetic field is inversely proportional to the radial distance, then it states

$$|B| \propto \frac{1}{R}. \tag{4.4}$$

Here R is the distance from the major axis of the torus. Thus $\nabla B \parallel \hat{R}$ and the direction of the ∇B drift is always upwards or downwards, depending on the direction of the magnetic field and the charge of the particle.

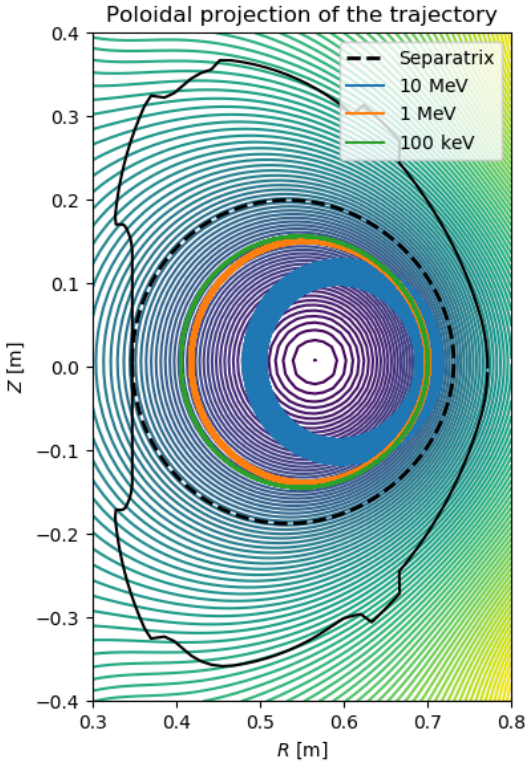

Figure 4.3: Poloidal projections of the trajectories of three passing particles with different energies. The particles were initialised on the same radial position (r = 0.7 m) with energies of 100 keV, 1 MeV and 10 MeV. The pitch ξ of particles was set to 0.9.

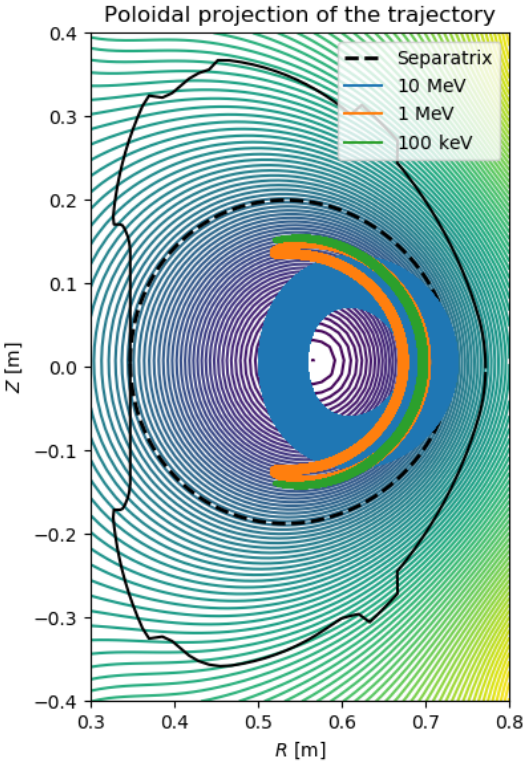

Figure 4.4: Poloidal projections of the trajectories of two trapped and one passing particle with different energy. The particles were initialized on the same radial position (r = 0.65 m) with energies of 100 kev, 1 MeV and 5 MeV. The pitch ξ of particles was set to 0.5.

There are two preserving quantities in the case that the particle are simulated in the static axisymetric magnetic field without presence of the electric field. The first quantity, which is conserved during simulation is the kinetic energy of the particle $\mathcal{E}$. The kinetic energy of the electron is given by relation

$$\mathcal{E} = E_{Tot} - E_{Rest} = (\gamma - 1)m_e c^2, \tag{4.5}$$

where E_{Tot} is the total energy of the particle and E_{Rest} is the rest energy of the particle. The conservation of the kinetic energy during the simulation of particles is displayed in the figures 4.5, 4.6. The quantity given by following formula is shown in the figures:

$$\frac{\Delta\mathcal{E}}{\mathcal{E}_0} = \frac{|\mathcal{E}(t) - \mathcal{E}_0|}{\mathcal{E}_0}. \tag{4.6}$$

Here $\mathcal{E}(t)$ is the kinetic energy of the particle at time t and $\mathcal{E}_0$ is the kinetic energy of the particle at the beginning of the simulation. The second quantity, which is conserved due to the presence of the axisymmteric magnetic field and follows from the Noether theorem, is the toroidal component of the angular momentum. The toroidal component of the angular momentum L_ϕ can be written as

$$\mathcal{L}_\phi = Rp_\phi + qRA_\phi \tag{4.7}$$

R is the radial distance, p_ϕ is the toroidal component of the momentum, q is a charge of particle and A_ϕ is the toroidal component of the vector potential. In the case of axisymmetric field of tokamak, we can express the toroidal component of the vector potential with help of relation $\Psi = -RA_\phi$, then the equation 4.7 has the following form

$$\mathcal{L}_\phi = Rp_\phi - q\Psi, \tag{4.8}$$

The conservation of the quantity is again shown in figures 4.7, 4.8. As in the case of the conservation of the energy, the quantity given by

$$\frac{\Delta\mathcal{L}_\phi}{\mathcal{L}_{\phi 0}} = \frac{|\mathcal{L}_\phi(t) - \mathcal{L}_{\phi 0}|}{\mathcal{L}_0} \tag{4.9}$$

is computed. All the variables in 4.9 have a similar meaning like the variables in the equation 4.6. From the behaviour of the preserving quantities, we can conclude the quality of simulation (quality of the integrator, interpolation, . . .) and reliability of the results. From the figures 4.5, 4.6, 4.7 and 4.8, it can be seen that errors of the simulations are bound.

The simulation described in the previous text was done by the Boris-Buneman scheme. As was described in the chapter 2, the Boris-Buneman scheme is not the best choice for description of the dynamics of fast electrons. The scheme dedicated for this purpose was denoted as VPA (Volume Preserving Algorithm). The simulation of the six particles was also done by VPA with the same results as the Boris algorithm. For illustration of the behaviour of the VPA solver the evolution of the error of preserving quantities are displayed and compared with behaviour of the Boris-Buneman algorithm in figures 4.9, 4.11, 4.10 and 4.12.

In the figures 4.9 and 4.10 the errors of the energy and the toroidal component of the angular momentum for the passing particles are shown. In the figure 4.9 we can see, that VPA has larger

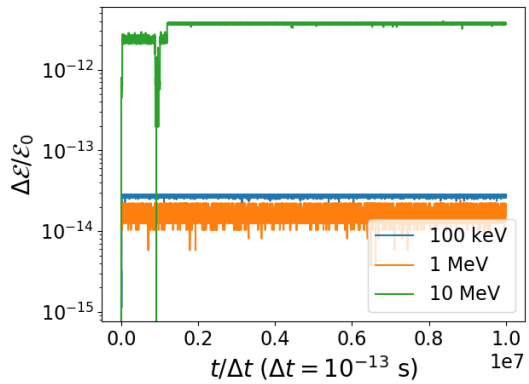

Figure 4.5: Change of the energy during simulation of the passing particle using the Boris-Buneman algorithm.

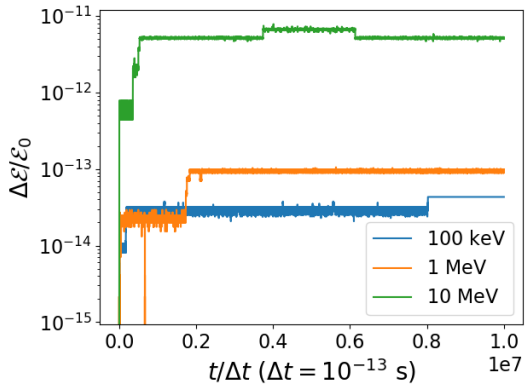

Figure 4.6: Change of the energy during simulation of the trapped particles using the Boris-Buneman algorithm.

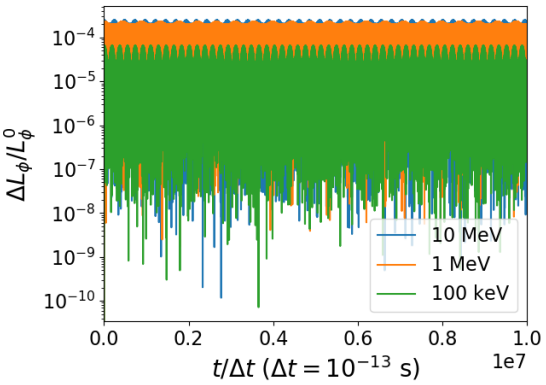

Figure 4.7: Change of the toroidal momentum during simulation of the trapped particles using Boris-Buneman algorithm.

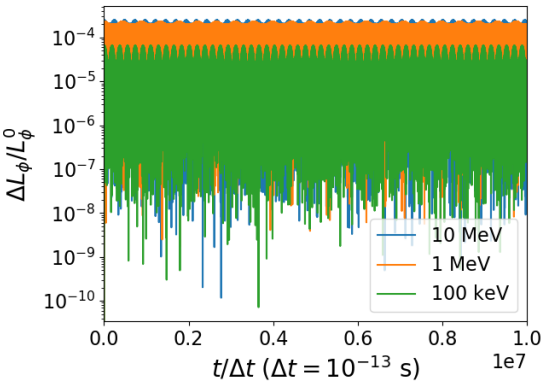

Figure 4.8: Change of the toroidal momentum during simulation of the trapped particles using Boris-Buneman algorithm.

errors than the Boris-Buneman scheme. This difference in the error is probably caused by the computationally demanding nature of the VPA. The scheme is volume preserving, but involves numerically difficult operations e.g. calculation of the inverse matrix. However, as can be seen in the figure 4.10 the VPA results better with respect to momentum conservation. The same situation is repeated in the figures 4.11, 4.12 for the case of trapped particles.

For the better illustration of the particle trajectories in the figures 4.13, 4.14, 4.15, 4.16, 4.17 and 4.18, the trajectories of studied particles in 3D are shown. The trajectories of the particle are plotted by the red curve. The poloidal projections of the particles trajectories displayed in black.

4.4 Method of the simulation of the impact

The convention method of simulation of the impact of the particles, which was used for example in determination of the influence of the blanket module in ITER on confinement of

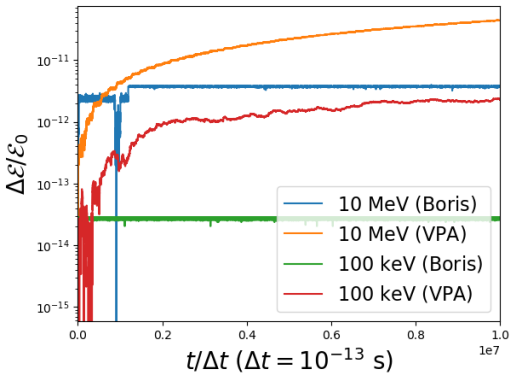

Figure 4.9: Change of the energy in simulation of the passing particles calculated by Boris-Buneman algorithm and by VPA.

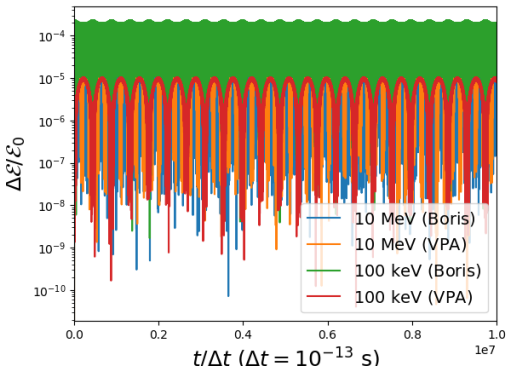

Figure 4.10: Comparison of change of the momentum in simulation of the passing particles calculated by Boris-Buneman algorithm and by VPA.

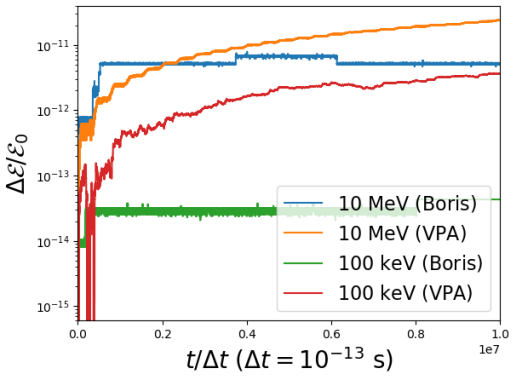

Figure 4.11: Comparison of change of the energy in simulation of the passing particles calculated by Boris-Buneman algorithm and by VPA.

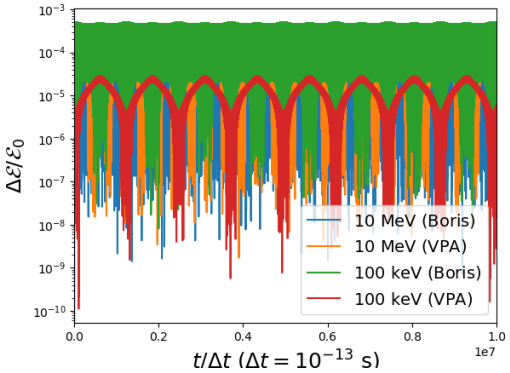

Figure 4.12: Comparison of change of the momentum in simulation of the passing particles calculated by Boris-Buneman algorithm and by VPA.

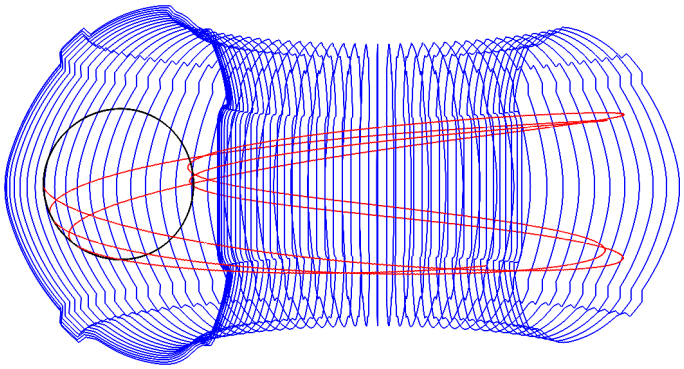

Figure 4.13: Visualization of the trajectory of the passing particle. The particle energy is 100 keV.

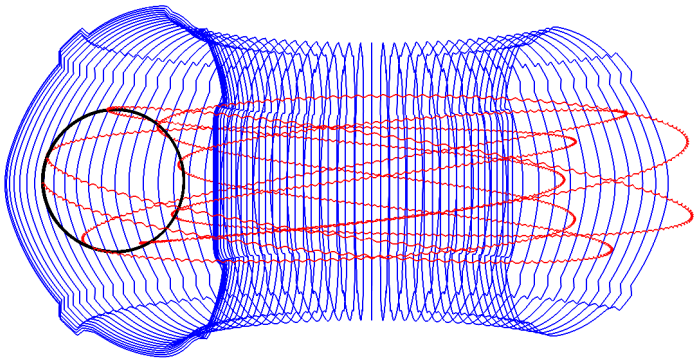

Figure 4.14: Visualization of the trajectory of the passing particle. The particle energy is 1 MeV.

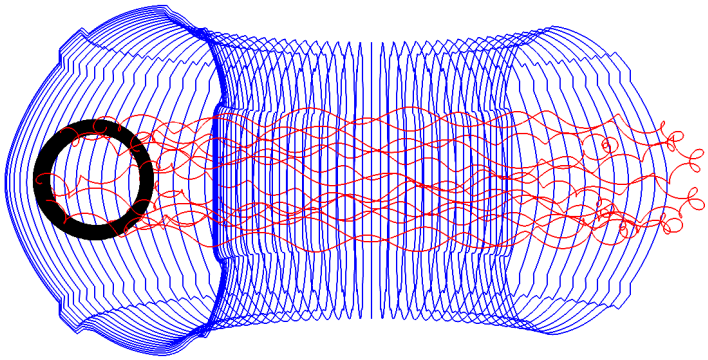

Figure 4.15: Visualization of the trajectory of the passing particle. The particle energy is 10 MeV.

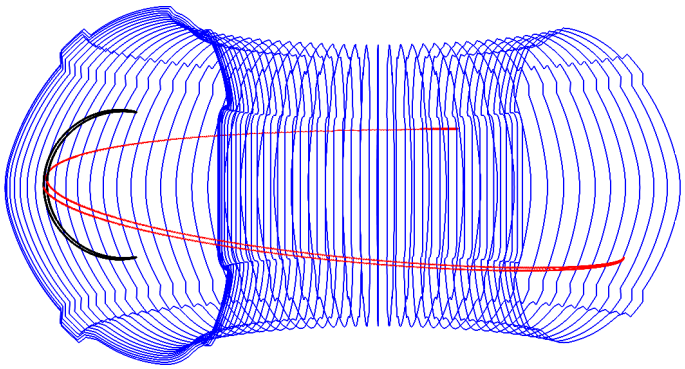

Figure 4.16: Visualization of the trajectory of the trapped particle. The particle energy is 100 keV.

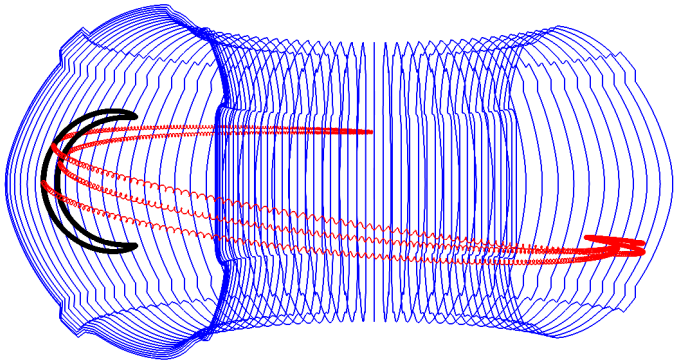

Figure 4.17: Visualization of the trajectory of the trapped particle. The particle energy is 1 MeV.

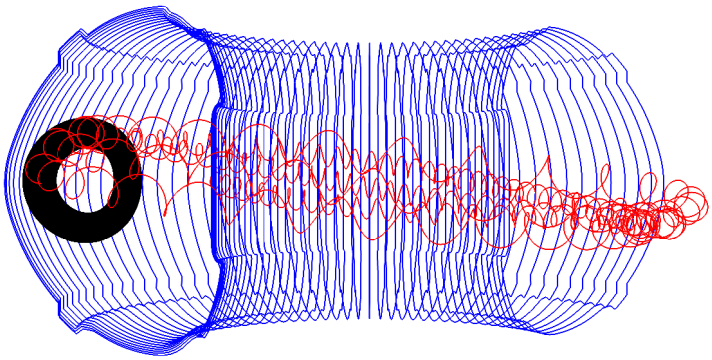

Figure 4.18: Visualization of the trajectory of the passing particle. The particle energy is 10 MeV.

fast particles [23], is based on the random initialization of the particles inside plasma and then followed by particle tracking for several milliseconds. If some particles do not hit the first wall of the device, they are declared to be confined. For the lost particles the location of their impact is determined and the connection between the effects influencing the dynamics of the particles is searched for.

If we are interested in the calculation of location of the impact, the importance of the full orbit solvers is increased. Because the guiding centre formalism describes only the movement of the guiding centre, the impact location determined by this approach can differ from the reality. The standard method, how deal with it, is to switch to the full orbit approach before the particle hits the wall. The position of the guiding centre and the size of the Larmor radius are known and only the gyro-angle has to be chosen. Many specialized articles dedicated to particle tracking were written showing the discrepancy in determination of the location of the impact between the full orbit method, guiding centre method and combined method - guiding centre with switching to full orbit [38, 37].

The choice of the full orbit approach has both advantages and disadvantages. The benefits of this method are correct description of the particle motion without any assumptions and a possibility of precise calculation of the point of impact. On the other hand, this approach presents high computational demands. This difficulty almost excludes the possibility of the tracking particles for several milliseconds without implementation of the simulation code in the low-level programming languages (C, C++, Fortran, ...) and use of supercomputers. Because of this difficulties the new approach of determination of the impact has to be considered.

It should be reminded, the simulations are carried out in the static axisymmetric magnetic field without assuming any effects of the toroidal ripple or different error fields, which could have detrimental effects on confinement. The particle will follow the field lines and stay confined, except for the particles with large energies, this phenomenon will be discussed later. Notice, that the topology of the magnetic field is not the only parameter determining the particle trajectories. The influence of the electric field and the collisions have to be taken into account.

The electric field causes the acceleration of the particle and thus rise of the particle energy. The result of the acceleration of the particle is slow radial outward drift. The velocity of this slow drift can be approximated by the formula [18]

$$v_{dr} = \frac{qE}{B_0}, \tag{4.10}$$

where the q is the safety factor, E is a magnitude of the electric field and B_0 is the magnitude of the magnetic field on axis. If we assume typical COMPASS-like parameters $q = 2$, $E = 0.4\ \mathrm{V/m}$ and $B_0 = 1.5$ T, we get $v_{dr} = 0.53$ m/s. With the knowledge of the value of the drift velocity caused by the toroidal electric field, we can guess a confinement time of the runaway electrons from equation

$$\tau_{conf} = \frac{a}{v_{dr}}. \tag{4.11}$$

Here a denotes the minor radius of the tokamak. If we take a equal to 0.23 m (COMPASSs minor radius), we get the value of the confinement time as $\tau_{conf} = 432$ ms. In spite the fact

that relation (4.10) has to be understood more likely as a guess of the order of magnitude of the drift, it shows us, that the outward drift caused by accelerating electric field is rather slow.

The outward drift of the particles could be also caused by collisions, but the collisionality of the relativistic electrons is low, thus we can assume that the electrons are collisionless without causing large inaccuracy in our results. We have to keep in mind, that the collisions still influence the dynamics of the fast electrons.

The method used for simulation of the impact of the runaway electrons skips the part of the simulation, in which particles are accelerated inside the plasma volume. In this part of simulation, only the gradual acceleration and the energy growth is in this part of simulation. This acceleration causes the outward drift and ends, when particle crosses the separatrix. The flux surfaces behind the separatrix are not closed and the field lines end on the inner wall surface. The particles on these field lines are lost and hit the surface.

Our approach is based on initialization of particles close to the separatrix, but outside the separatrix e.g. outside the plasma. By this choice, as was already said, we skips the accelerating phase of the simulation and concentrate on the dynamics of the particles outside the plasma. In this case the particles are indeed collisionless and we do not take into account the electric field, because the influence of the field is almost negligible on small time scale.

In the end of the section, the simulation method will be summarised. At beginning particles of various energies and pitch angles are initialised in the vicinity of the separatrix but outside the plasma volume. Then the trajectory of the particle is calculated and the impact point of the particle is determined. The primary motivation of this research is not determination of the location of impact but decision, which particles could be detected by the Cherenkov detector. The basic description of the Cherenkov detector is given in the fourth chapter of the thesis, detailed description of the detector and its principle of detection is given in the previous work of the author [7]. From the point of view of the evaluation of the simulation we are not only interested in location of the impact but also in the question whether the trajectory of the particle crosses the volume of the detector.

4.5 Initialization of the particles

As was reported in the previous section, the particles are in the beginning of the simulation initialised in the vicinity of the separatrix but outside the plasma volume. Approximately 100 particle were uniformly distributed in each simulation. The described method is visualised in the figure 4.19. This method of the initialisation of particles enables study of the dynamics behind the separatrix even for low energy particles. The low energy particles strictly follow the field lines and these particle cannot escape from the plasma volume in our model without influence of additional effects like collisions. The collisions would cause the diffusive-like behaviour of the particles. If we employ also accelerating electric field in the simulations, the energy of the particles will probably grow to much before the particles cross the separatrix and the study of the of low energetic electrons would be very difficult.

In the previous section, it was also written that particles, which are initialised outside the separatrix, hit the wall. However, it is not always true for high energetic particles. Particles with high energy deviate from initial flux surface and thus can be confined even if in the beginning

of the simulation it was situated in the vicinity of the field line, which crosses on the material surface.

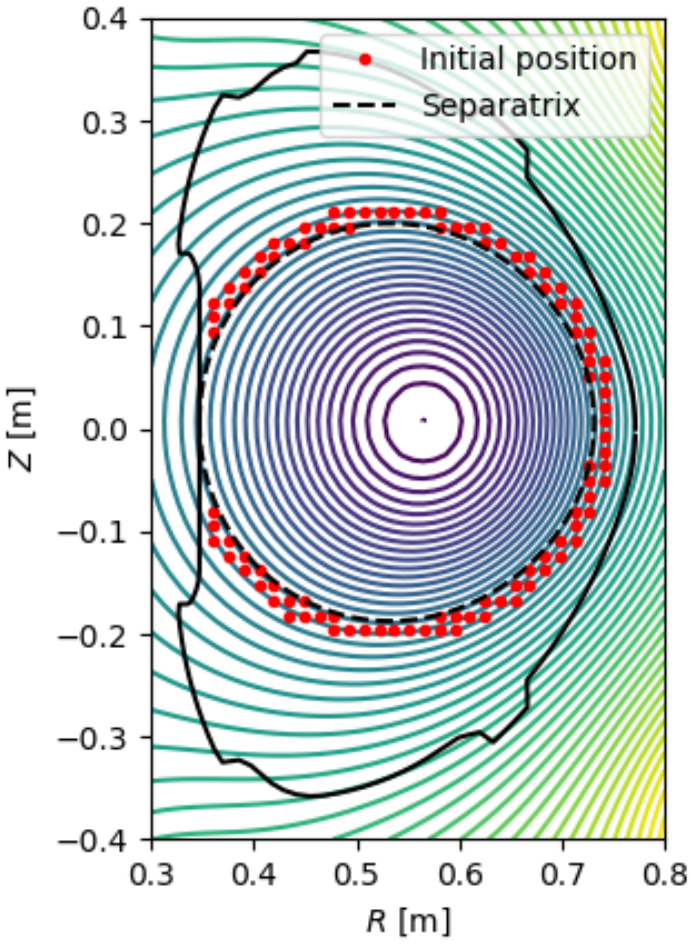

Figure 4.19: The example of the initialization of the particles in simulation. The particles were set in the vicinity of the separatrix, but outside the plasma volume.

4.6 Influence of the orientation of B_ϕ

Topology of the magnetic field is crucial for plasma confinement. The orientation of the magnetic field affects the drifts of the particles. For example in the COMPASS tokamak standard orientation of the magnetic field is clock-wise, if we are looking from above on the tokamak device, and the direction of the plasma current is the same. If we assume that the direction of the plasma current is determined by the movement of the positively charged particles, the runaway electrons have to move in the opposite direction. Due to the fact that the conventional of definition of cylindrical coordinates system has angle anti-clock wise oriented, the standard magnetic field is always written with negative sign, as $B = -1.15$ T. This configuration of the magnetic field is called forward.

In figures 4.20 and 4.21 the poloidal projections of trajectories of electrons with energy 60 keV are shown. In figure 4.20 the particle in the forward orientation of the magnetic field and plasma current is shown. On the other hand, in the figure 4.21 the particle in the reversed magnetic field configuration is displayed ($B_T = 1.15$ T). As is clearly seen from the figures, dynamics of the electrons is different. They are moving in the poloidal plane in the opposite directions. From the figures we can see, that due to the different direction of the movement of the electrons, the location of the impact is very different. Consequently, the detection of the particle by the Cherenkov detector can be influenced by the field orientation.

The particles were simulated for 10^{-6} s with the time step Δt between $10^{-12} - 10^{-13}$ s. The chosen time of simulation is sufficient even for low energetic particle to complete at least one poloidal rotation. Most of the particles were not be tracked for the whole time interval, because they hit the wall. But not all of initialised particles hit the wall. The particles with lower energies and higher pitch angles can be trapped. On the other hand, the particles with higher energies (> MeV) deviate significantly from the initial flux surface and can be confined even if they were initialised on the field line, which crosses the material surface.

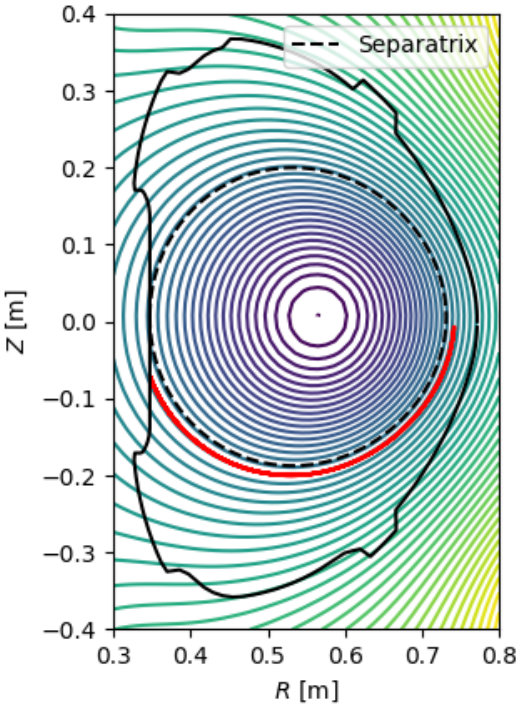

Figure 4.20: The graph of the poloidal projection of the particle trajectory (red) in forward configuration of the magnetic field. The toroidal magnetic field has the same orientation as the plasma current.

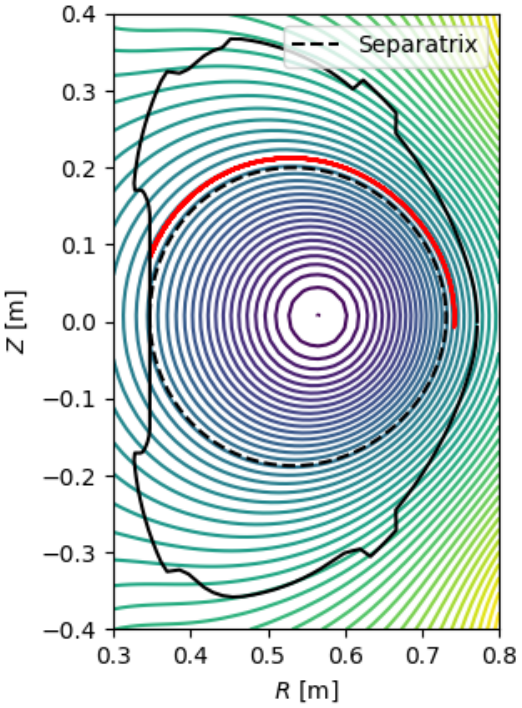

Figure 4.21: The graph of the poloidal projection of the particle trajectory in reversed configuration of the magnetic field. The toroidal magnetic field has opposite orientation to the plasma current.

The events, when the particles were confined, were excluded from the impact location statistics, because they could not reach the wall in the described model. In the case of electrons on banana orbits, if the electric field would be present in the simulation, the trapped electrons will

pitch inwards to the centre of the tokamak until the detrapping condition meet is. Afterwards, the electrons would be accelerated due to the accelerating electric field and slowly radially move outwards due to growth of the velocity parallel to the magnetic field. In the case of electrons, which are confine due to their sufficiently large momentum resulting in the deviation of the initial flux surface. They will be further accelerated by the electric field and reach even higher energies, but outward drift is connected with the growth of the energy, which will result in collision with the wall. The electrons will hit the wall on the high field side of the tokamak. The exclusion of the confine electrons from the impact statistics could give rise to some errors, but as the matter of fact, the presented model is already highly idealised.

4.6.1 Impact of the particles

In the figure 4.22 histograms of the impact of electrons with various energies and pitch angles are shown. In the figures the number of impact of particles depending on the poloidal angle θ is shown. The point with poloidal angle $\theta = 0$ satisfies the condition $Z = 0$ and $r = R - R_0 > 0$, where R_0 is the major radius of the tokamak. The point corresponding to poloidal angle $\theta = \pm\pi$ satisfies the conditions $Z = 0$ and $r = R - R_0 < 0$. In the clockwise direction from $\theta = 0$ the poloidal angle decreases and has always negative values, while in the anti-clockwise direction it increases and has positive values.

From the figures, it is seen that all particles with energies lower than 1 MeV hit the wall around $\theta = \pm\pi$. It means that the location of the impact is low field side limiter. This trend is visible for all simulated pitch angles. Only the most energetic particles are capable of hitting the wall on different poloidal location. The energetic particles mostly hits the wall on the high field side.

Similar situation is illustrated also in figures 4.23 where results of simulation in the reversed field configuration are presented. As in the previous case, the low energetic particle hit the wall on the high field side and while of the more energetic particles hit the the wall of the tokamak on the low field side.

Notice, there are some differences between two studied cases. In the case where the magnetic field is oriented in the direction of the plasma current (forward configuration of the magnetic field), majority of the locations of the impact of high energetic particles lies in the interval $\theta \in (0, 0.5\pi)$. On the contrary, in the case of the reversed field, the majority of the locations of the impact of the energetic particles lies in the interval $\theta \in (-0.5\pi, 0)$. This distribution of the locations of the impact is a result of the direction of the drift movement in the poloidal projection. Both cases are not exactly symmetrical. In the reversed field configuration, small number of more energetic particles hit the wall the above mid-plane on high field side.

4.6.2 Detection of the particles

The main reason of simulation of the particle trajectories was the determination of the parameters of the runaway electrons that can be detected by the Cherenkov detector. For this purpose the same simulations as in the case of determination of the location of the impact were used. However, in these studies the trajectories were tested if across the defined area of the detector.

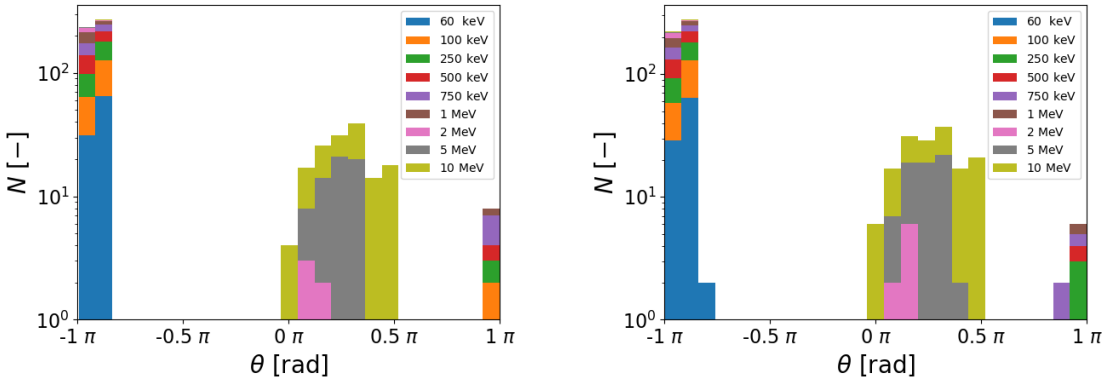

(a) $\xi = 0.9$ (b) $\xi = 0.8$.

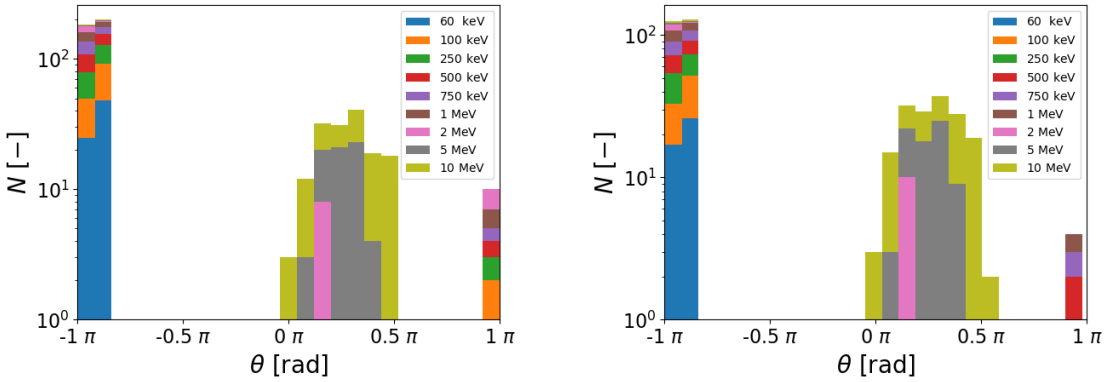

(c) $\xi = 0.7$ (d) $\xi = 0.6$

Figure 4.22: Histograms of the detected impact of the particles with four different pitches $\xi = \frac{v_\parallel}{v}$.

The detection area of the Cherenkov detector - the Cherenkov radiators, are too small to apply our method of the simulation of particle trajectories. From this reason the trajectories were tested, if crosses area comparable with dimensions of the Cherenkov measuring head. This choice could be a source of additional errors. The Cherenkov detector was modelled in different radial positions and the dependence of the radial position on parameters of the runaway electrons like energy and the pitch angle was investigated.

The Cherenkov detector was always modelled to be on the mid plane ($Z = 0$ m) and only its radial position was changed in simulations. The radial position is denoted by R, where R equals zero on major tokamak axis.

In the figures 4.24 the dependencies of number of detected particles on the energy and pitch of the particle are displayed in the different radial positions of the detector. In the figure 4.24a the case is shown, in which the detector is placed at $R = 0.755$ m. From the figure it can be clearly seen, than the dependence of the number of detected particles is roughly identical for all pitches and it is peaked for the energy of 2 MeV. In the figures 4.24b and 4.24c, which represents the measuring with the Cherenkov detector placed at $R = 0.760$ m, $R = 0.765$ m respectively, we can see similar trends as in the figure 4.24a. However, the figure 4.24d differs from the others, because it shows different trends. In this radial location, which corresponds to

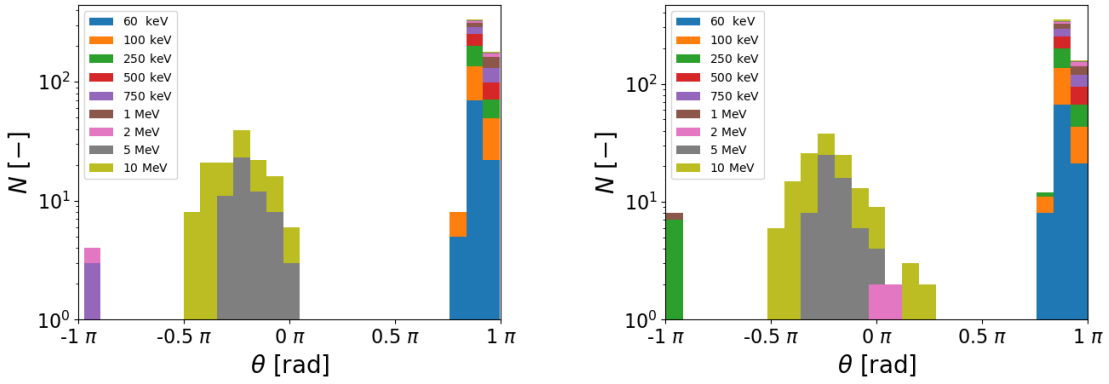

(a) $\xi = 0.9$ (b) $\xi = 0.8$

(c) $\xi = 0.7$ (d) $\xi = 0.6$

Figure 4.23: Histograms of the detected impact of particles witch four different pitches $\xi = \frac{v_\parallel}{v}$. The particles were simulated in the reversed field configuration.

the edge of the port of the tokamak, the electrons with 10 MeV dominate.

In the previous analysis all initialized electrons were taken into account. If we assume that the trajectories of the electrons are shifted outwards, we can restrict our analysis only on particles, which were initialized in position with radial coordinate greater then 0.6 m ($R >$ 0.6 m). Then the trajectories of the particles can be analysed as in the previous case. The results are shown in the figure 4.25. The main difference between analysis with all particles and particles for which initial position fulfil the condition $R > 0.6$ m is that in the later case the particles with higher energies (> 5 MeV) play more important role than low energetic one.

If the sum of the detected particle is done for each position of the detector, the radial position scan of the Cherenkov detector could be imitated. The result is visible in the figure 4.26. From the potentially detected particles were only ones, which were initialised with radial position greater than the $R = 0.6$ m were chosen. From the figure it can be seen, that with the decreasing radial distance of the Cherenkov detector the number of the detected particle increases. This agrees with the experimental observations, which will be discussed in the last chapter. From figure 4.24 is also obvious that only the high energy particles are detected.

So far only the results of the simulations, which were carried out with the standard orienta-

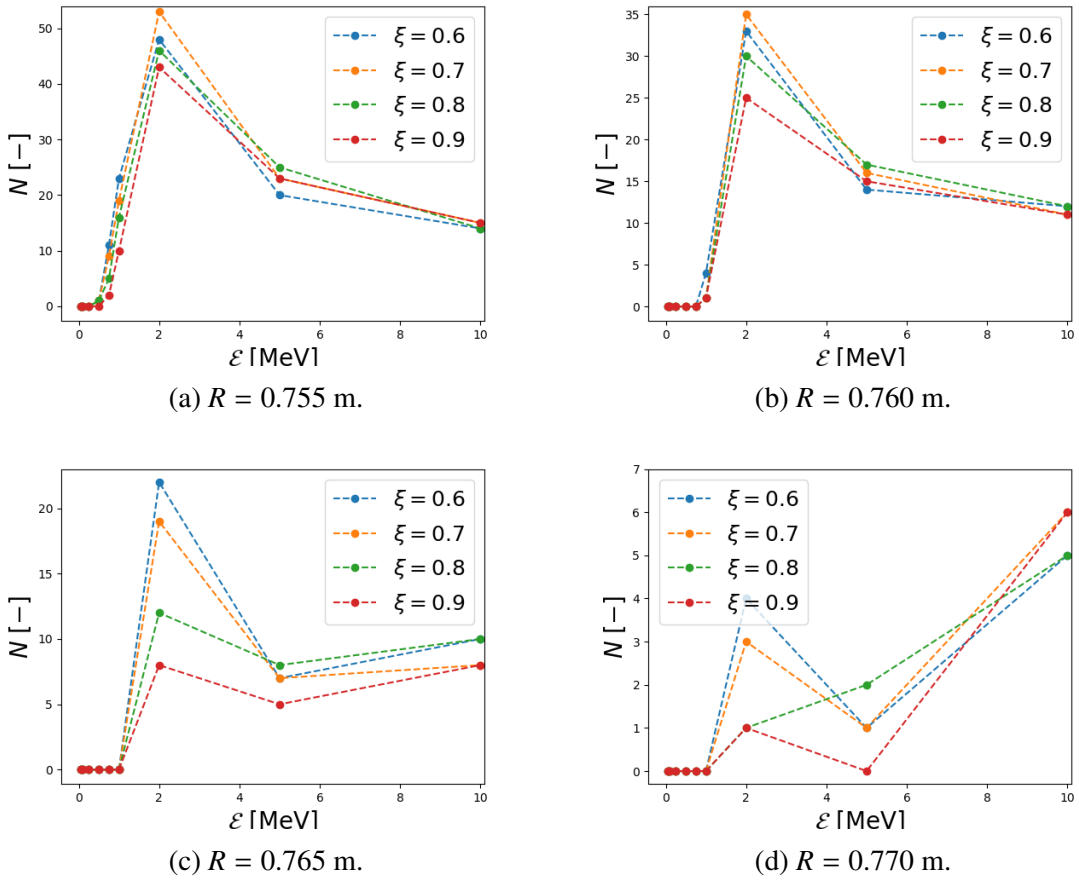

(a) R = 0.755 m.

(b) R = 0.760 m.

(c) R = 0.765 m.

(d) R = 0.770 m.

Figure 4.24: The dependences of the number of detected particles on energy E and pitch ξ for different position of the detector.

tion of the magnetic field were presented (forward configuration of the magnetic field). In the following text the results from the simulation in reversed field configuration will be shown and only electrons with initial radial position greater than 0.6 m will be assumed. The dependencies of number of detected particles on energy and pitch for the detector placed in the various radial positions are displayed in figure 4.25. From the figure it can be seen that the numbers of detected particles are approximately equal to the case with the standard orientation of the magnetic field. Also the trends of dependences of numbers of detected particle on their energy and pitch behave similarly for both cases. For completeness in the figure 4.28 the dependence of all detected particles on the radial position is shown.

4.7 Influence of the B_ϕ magnitude

The direction of the magnetic field is not the only parameter, which can influence the topology of the magnetic field and therefore has effect on the dynamics of particles. Another parameter, which can be changed, is a magnitude of the toroidal magnetic field. In the following

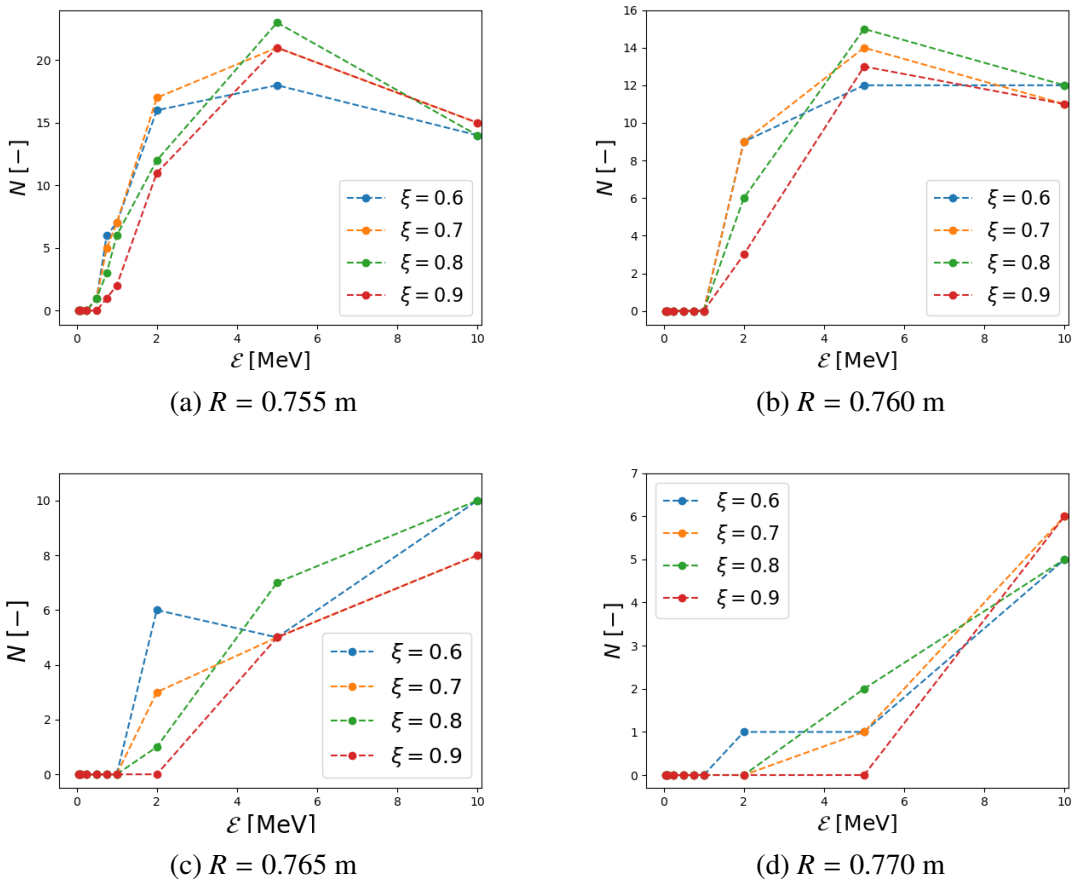

(a) $R = 0.755$ m (b) $R = 0.760$ m

(c) $R = 0.765$ m (d) $R = 0.770$ m

Figure 4.25: The dependences of the number of detected particles on energy $\mathcal{E}$ and pitch ξ for different position of the detector. From the all potentially detectable particles were chosen only these, which were initialized with the radial position greater than 0.6 m ($R > 0.6$ m).

section the discharges with the values −0.92 T and 1.5 T of the toroidal field on the magnetic axis will be studied.

For the following studies the discharges #16649 and #16651 were used. The discharges were carried with same plasma current $I_p = 140$ kA in the flat-top phase, which is a phase of the discharge with the constant plasma current. The equilibrium reconstruction of the field was taken from the time 1200 ms. The discharges differ in the magnitude of the toroidal field. In the discharges #16649 and #16651 the magnitude of the magnetic field on axis was −1.5 T and −0.92 T, respectively. With the same plasma current I_p, which is driven through the plasma column and creates the poloidal magnetic field, the discharges differ in the safety factor q. The safety factor q is defined as the number of toroidal transits per single poloidal transit of the magnetic field line on a toroidal flux surface. So the safety factor could be written

$$q = \frac{m}{n}, \tag{4.12}$$

where m denotes a number of toroidal turns, which are needed to complete n turns in poloidal direction. If the circular cross section of the plasma can be assumed, the safety factor can be

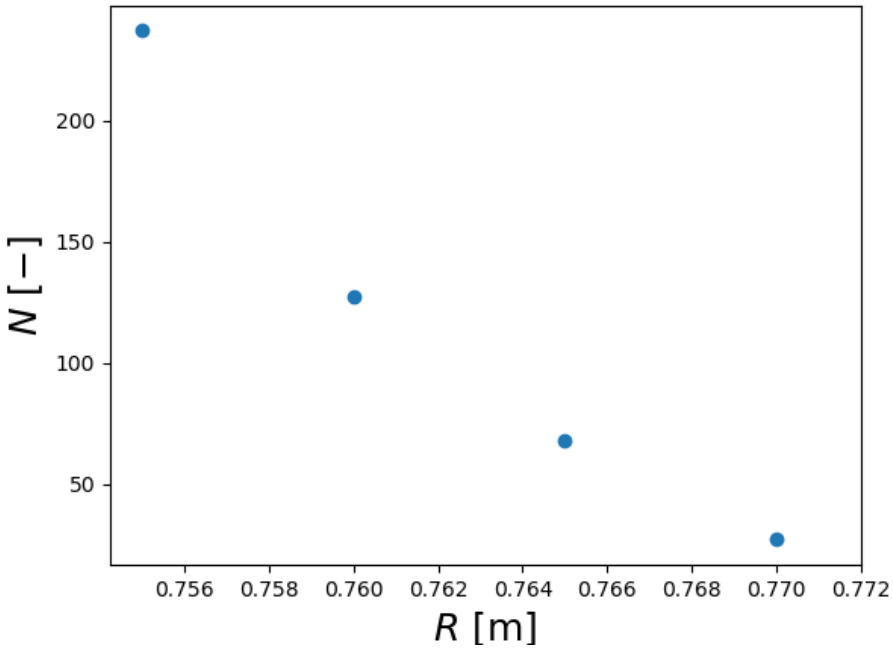

Figure 4.26: Dependence of the detected particles on the radial position of the detector. From potentially detectable particles only those were chosen, which were initialised with the radial position greater than 0.6 m ($R > 0.6$ m)

.

expressed as

$$q \approx \frac{r}{R}\frac{B_T}{B_p}, \tag{4.13}$$

where r denotes the radial distance from the tokamak centre, R is major radius of the tokamak, B_T and B_p states for the toroidal and poloidal magnetic field strength respectively. From the equation (4.13), it can be seen, that with the increasing toroidal magnetic field the safety factor q is also increasing. For characterization of the safety factor and its profile the two special values are used. The limit of the safety factor on magnetic axis is denoted q_o and safety factor in 95% of the minor radius of the tokamak is used and denoted q_{95}.

4.7.1 The impact of particles

In the discharge with lower magnetic field (−0.92 T) at 1200 ms the parameters have values: $q_0 = 1$ and $q_{95} = 2.6$. As it was done in the previous chapter, the locations of the particle impacts were search. The results are given in the figure 4.29 . As it can be seen from the graphs, the character of results agrees with results obtain with standard orientation of the field, which was investigated in the previous section.

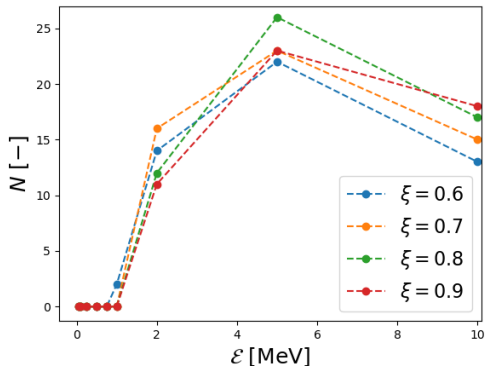

(a) R = 0.755 m.

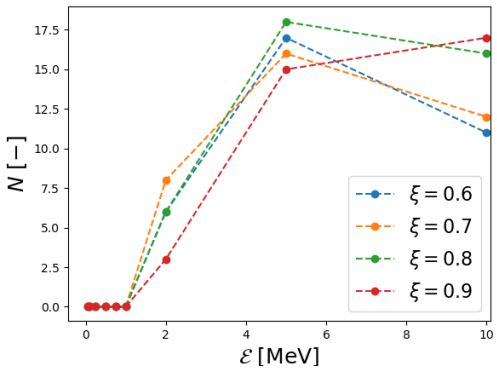

(b) R = 0.760 m

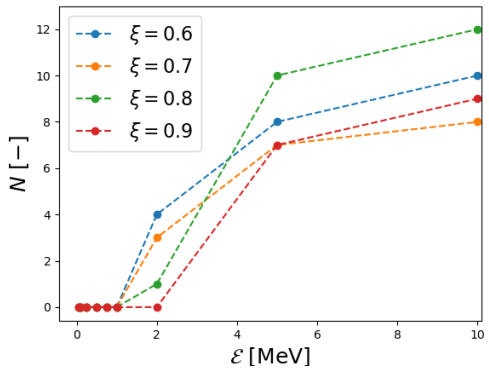

(c) R = 0.765 m

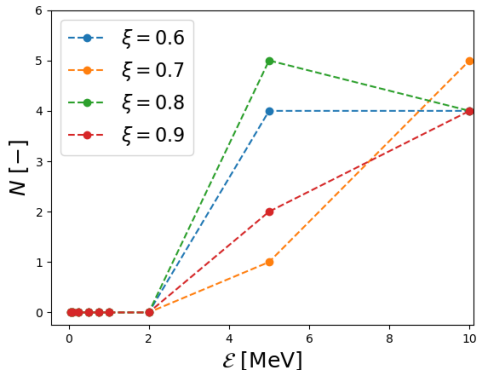

(d) R = 0.770 m

Figure 4.27: The dependences of the number of detected particles on energy $\mathcal{E}$ and pitch ξ for different position of the detector. From the all potentially detectable particle were chosen only these, which were initialized with radial position greater than 0.6 m ($r > 0.6$ m). The simulation was carried out with the reversed toroidal magnetic field.

The figure shows, that on the outer midplane only particles with MeVs energies are capable of an impact. Other less energetic particles follow the field lines and impact on the high field side limiter.

A slightly different situation is illustrated in the figure 4.30 where the results from simulation with higher magnetic field are displayed. The q and q_{95} were in this case 1.3 and 3.5, respectively. From these figures it can be seen, that only the electrons with energies 5 and 10 MeV were capable to hit the first wall on the low field side.

4.7.2 Detection of the particles

As in the comparison of the influence of the orientation of the toroidal magnetic field, the investigation of possibility of the detection of the runaway electrons by Cherenkov detector in toroidal magnetic field with the various magnitude was also done. The evaluation of the simulation was done as in the previous case.

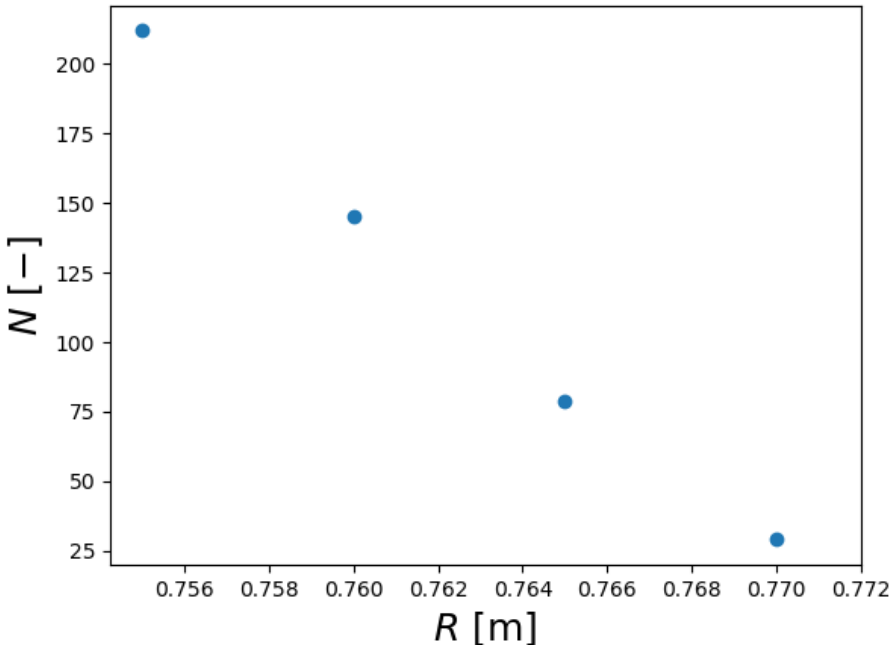

Figure 4.28: Dependence of the detected particles on the radial position of the detector. From potentially detected particles only those were chosen, which were initialised with the radial position greater than 0.6 m ($R > 0.6$ m). The simulation was carried out with the reversed toroidal field.

In the figure 4.31 the dependences of number of detectable electrons on energy and pitch are displayed for various radial positions of the Cherenkov detector in the case of lower magnetic field. In the graphs the corrected number of detectable particles are shown, i.e. only electrons with initial radial position greater than 0.6 m were assumed.

For position $R \leq 0.760$ the detector is capable to detect relatively large number of particles with energies around 1 MeV. However, for the detector position $R \geq 765$ m the particle with energies $E > 2$ MeV dominate. This behaviour of the simulated position scan with Cherenkov detector remains valid for greater radial positions in all analysed cases.

If we compare results from last paragraph with results displayed in the figure 4.32 , where the results from the simulation carried out in the higher toroidal magnetic field are shown, we can distinguish important differences. In the case of the lower toroidal magnetic field the Cherenkov detector is capable to detect more particles, than in the case with higher magnetic field. In the higher magnetic field only the particles with energies greater than 4 MeV can be detected.

The differences in that two studied cases are also clearly visible in the figure 4.33, where the imitation of the position scan with the Cherenkov detector is displayed. From the figure it can be seen, that for the higher magnitude of the magnetic field (−1.5 T) the number of detectable particles is substantially decreased compared to case with lower magnitude of the toroidal magnetic field (−0.92 T).

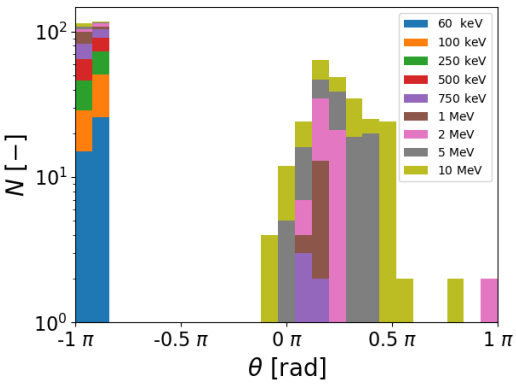

(a) $\xi = 0.6$

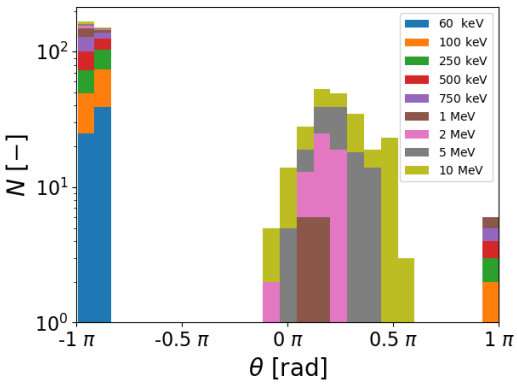

(b) $\xi = 0.7$

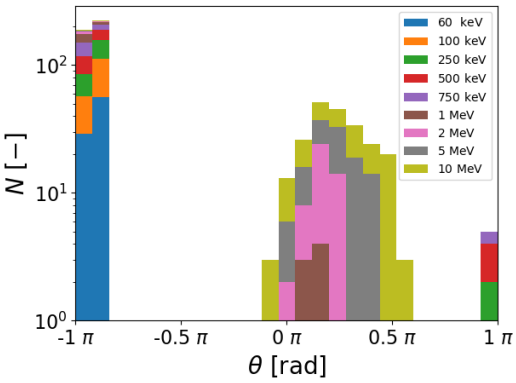

(c) $\xi = 0.8$

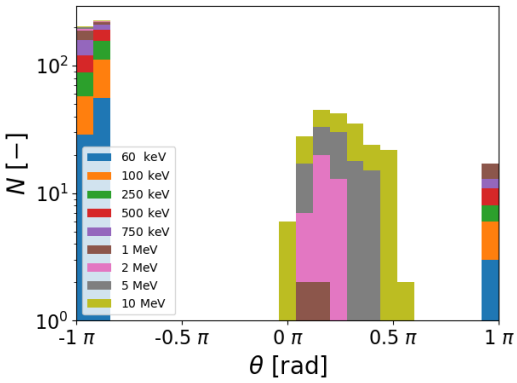

(d) $\xi = 0.9$

Figure 4.29: Histograms of the detected impact of the particles with the different pitches ξ. The particles were simulated in the toroidal magnetic field with value $B_T = -0.92$ T on magnetic axis.

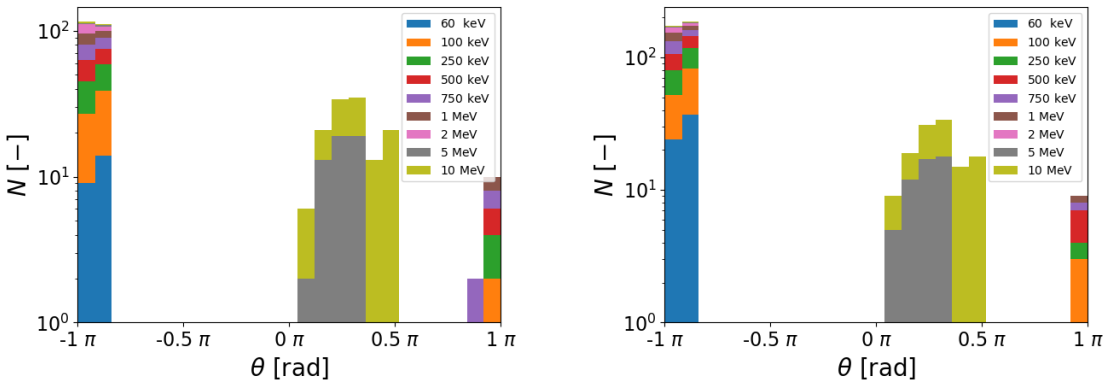

(a) $\xi = 0.6$ (b) $\xi = 0.7$

(c) $\xi = 0.8$ (d) $\xi = 0.9$

Figure 4.30: Histograms of the detected impact of the particles with the different pitches ξ. The particles were simulated in the toroidal magnetic field with value $B_T = -1.50$ T on magnetic axis.

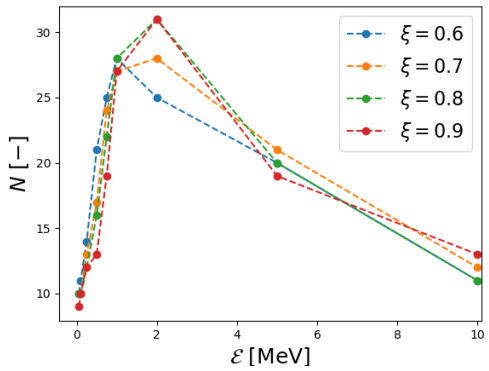

(a) $R = 0.755$ m

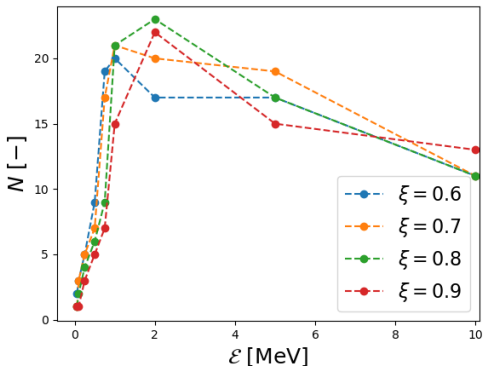

(b) $R = 0.760$ m

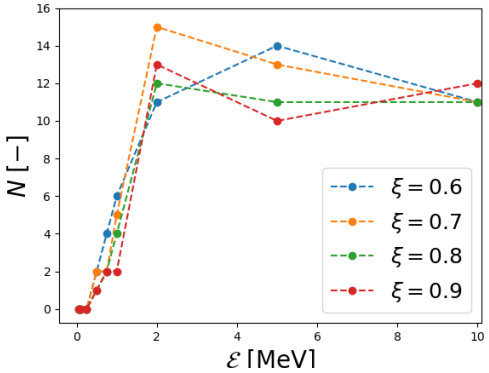

(c) $R = 0.765$ m

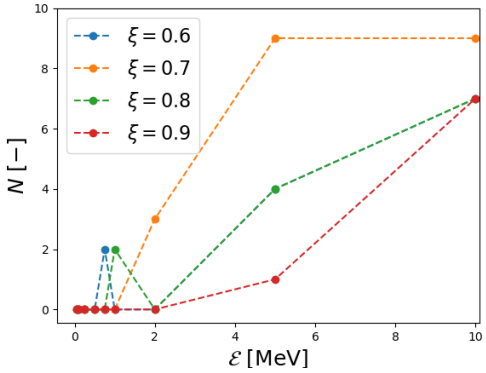

(d) $R = 0.770$ m

Figure 4.31: The dependences of number of detected particles on energy $\mathcal{E}$ and pitch $\xi = \frac{v_\parallel}{v}$ for different radial positions of the Cherenkov detector. From all potentially detectable particles only the particles, which were initialised with radial position greater than 0.6 m ($R > 0.6$ m). The simulations were carried out with the toroidal magnetic field $B_T = -0.92$ T on magnetic axis.

The observation described in the previous paragraph could be easily proved by the experiment. The runaway generation rates reviewed in the section 1.2 are independent of the magnitude of magnetic field. This means that during the discharges approximately the same population of the runaway electrons would be generated for different magnitude of the magnetic field. If the positions of the Cherenkov detector were the same for all discharges with the different magnitude of the magnetic field, different amounts of the particles could be detected by the Cherenkov detector, which results in different intensity of the measured signal. However, the experiment cannot be perform easily. In the tokamak COMPASS the substantial amount of the runaway electrons is generated during plasma breakdown and the plasma breakdown is affected by the magnitude of the magnetic field.

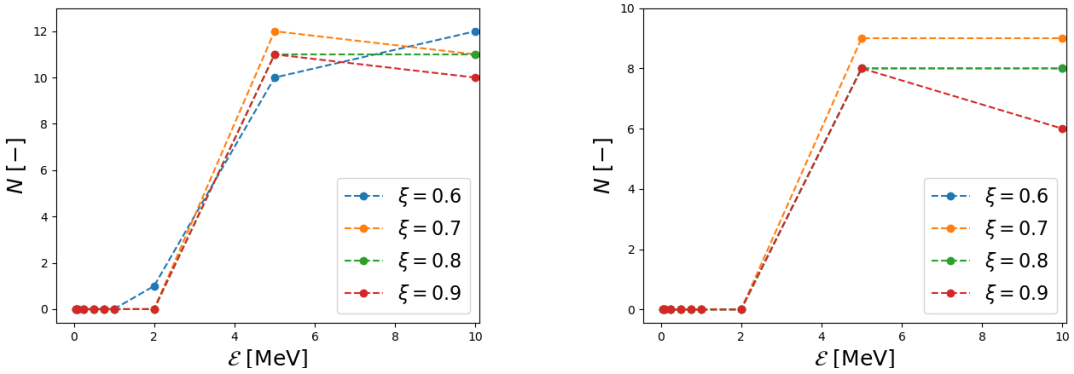

(a) $R = 0.755$ m (b) $R = 0.760$ m

(c) $R = 0.765$ m (d) $R = 0.770$ m

Figure 4.32: The dependences of number of detected particles on energy $\mathcal{E}$ and pitch $\xi = \frac{v_\parallel}{v}$ for different radial positions of the Cherenkov detector. From all potentially detectable particles only the particles, which were initialised with radial position greater than 0.6 m ($R > 0.6$ m). The simulations were carried out with the toroidal magnetic field $B_T = -1.5$ T on magnetic axis.

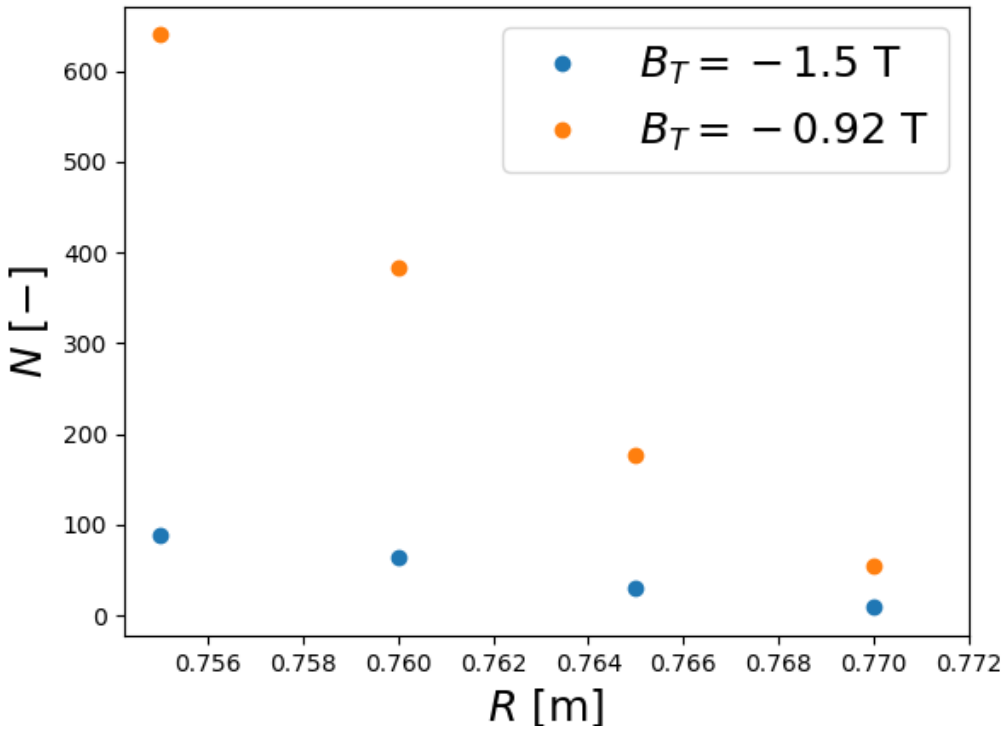

Figure 4.33: The comparison of the imitation of the position scan with the Cherenkov detector for two different values of the toroidal magnetic field on the magnetic axis.

Chapter 5

Comparison with experimental results

In this chapter the results of the simulations are compared with the experimental observations. The particular emphasis is put on analyzing data from the Cherenkov detector. The Cherenkov detector is a unique diagnostics tool, which is capable of direct observation of runaway electrons with a very good temporal resolution at a well-defined location. We have to keep in mind that the simulations presented in the previous chapter do not describe realistic situations in the tokamak plasma because they do not include several phenomenon, which could fundamentally influence the particle dynamics. These limitations will be also discussed in the following section (see 5.1).

5.1 Constraints of the model

The model presented in the previous chapter uses several simplifications, which can result in the disputable conclusions. The complex simulation code attempting to realistically describe the dynamics of runaway electrons faces many issues. The simulation has to be performed in the 3-D magnetic field, e.g. without assumption of axis symmetric magnetic field of the tokamak. This symmetry could be destroyed by toroidal ripples and for example in ITER by blanket modules, which are the source of the stray field. Another aspects is behavior of the plasma itself, the trajectories of the runaway electrons could be affected also by the plasma instabilities. This phenomenon was observed on several devices.

The simulation technique, which was used to perform the simulations, can also bring the mistakes to the drawing of the conclusions. The particle was initialized outside the separaterix and then the locations of their impact were calculated. This approach was used due to computationally demanding process, which would include slowly acceleration of the electrons and their slow drift from the plasma volume. This part of the simulation was skipped and only trajectory out of separatrix was reconstruct. This method could result in the wrong initial positions of the particles.

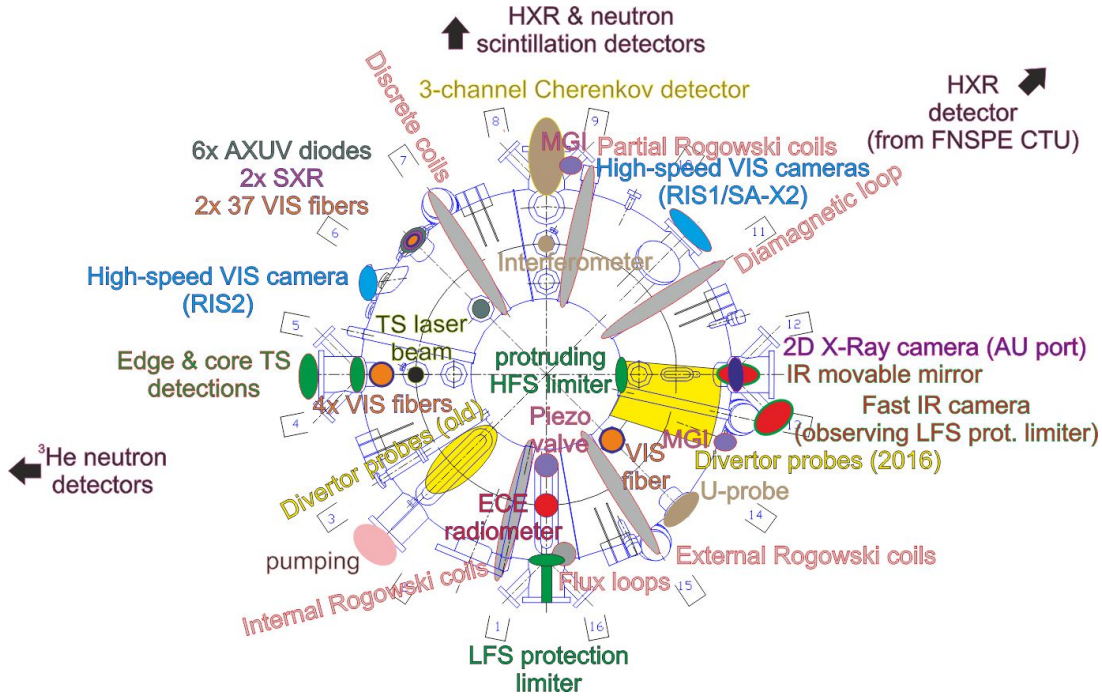

Figure 5.1: Experimental setup used during runway electrons studies.[citace]

5.2 Experimental setup

The experimental setup, which was usually used during the runaway electrons experiments, is shown in the Fig. 5.1. The interaction of the plasma facing component (PFC) with runaway electrons, which results in the emission of the hard x-ray (HXR) radiation, is measured by scintillation detector. The detector is based on NaI(Tl) scintillator with a photomultiplier. As can be seen in the figure 5.1 it is situated in the north wall of the tokamak hall. For measuring HXR radiation another scintillation detector is additionally installed. For detection of the so called photo-neutrons (see 1.4), which are produced by interaction of high energetic runaway electrons with the PFC, plastic scintillation detetor is used. The neutron detector is placed inside the lead housing (10 cm) in the north of the tokamak hall near the standard HXR detector. It is known, that the detector dedicated for detection of the neutrons is also sensitive to the high energetic photons. The neutron detector is denoted as HXR-S (S for shielding).

The Cherenkov detector [31], which detects the in-flight runaway electrons, is located in the horizontal port of the tokamak on the mid-plane. The Cherenkov type detector was intensively described in the previous work of the author [7].

5.3 The Cherenkov detector

A brief description of the detector used on the experiments in the tokamak COMPASS will be given (for details see [7]).

The idea of the Cherenkov detector is to use the Cherenkov radiation (see section 1.3.5), which is emitted by the charged particles penetrating through the material, for the detection

Figure 5.2: Detail of the measuring head of the multichannel Cherenkov detector.

Figure 5.3: The three-channel Cherenkov detector. In the figure the whole set-up of the Cherenkov detector is shown. The detector consists of the measuring head, the detector tube, the detector body and the flange.

of the fast electrons. When the particle travels through the so called radiator, then sufficiently energetic particles emit radiation. The emitted radiation is then transferred with help of the optic fibres to the photomultiplier and collected.

The three channel Cherenkov detector is shown in figure 5.2, 5.3. In the figures 5.2 the detail of the measuring head of the Cherenkov detector is displayed. The three radiators are clearly visible. The different thickness of the covering layer of the radiators sets the energy detection threshold for observation of the fast electrons. The radiators are typically crystals with the desired refractive index, the CVD diamonds are usually applied.

The Cherenkov detector is located in the horizontal port of the tokamak on the mid-plane. Before each measurement it can be placed in a different radial position in the tokamak chamber with help of movable support. For safety reasons the detector is always operated in larger radial positions than the position of the edge of the low field side protection limiter, i.e. in the shadow of the LFS limiter.

5.4 Experimental results

In the following section the experimental results will be discussed. Firstly, the profile of the electron fluency (signal from the Chererenkov detector integrated in the time domain) will be shown and compared with results of the simulation. Then the signal from the Cherenkov detector during ramp-up experiments will be shown. In these experiments the detector provides important insight into runaway dynamics during the disruptions. In this part of the section the two applied configurations will be discussed and their influence on the recorded signals will be considered. In the last section of this chapter effects of the MHD activity on losses of the runaway electrons observed by the Cherenkov detector will be shown.

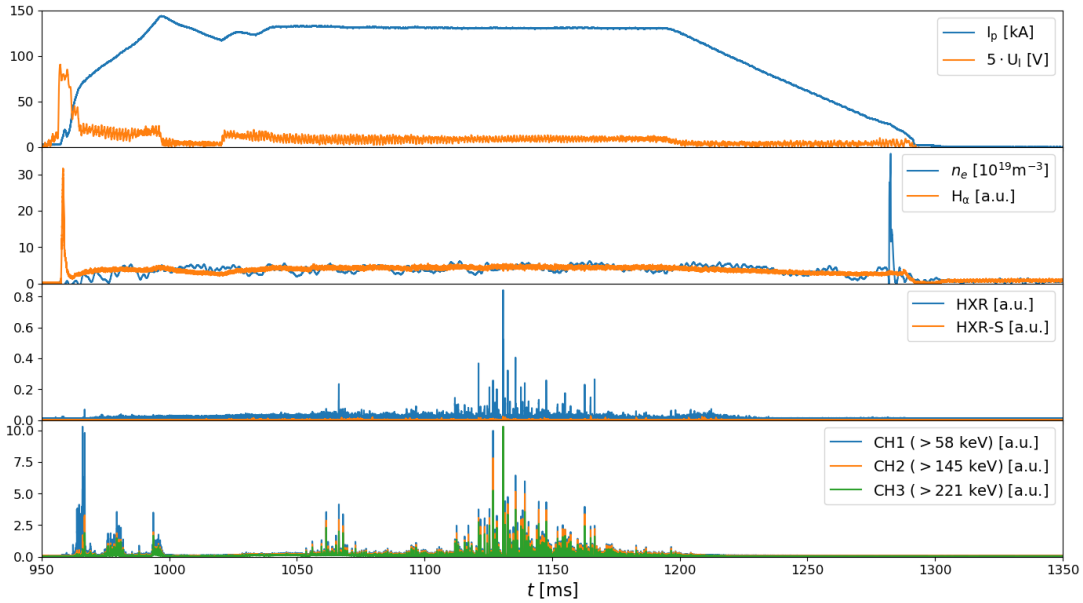

Figure 5.4: Overview of the basic signals from COMPASS shot # 14559. In the first graph the plasma current I_p and the loop voltage U_l is displayed. The electron density of the plasma with signal of the H_α radiation is shown in the second graph. In the third graph the signals from the HXR detector and from the shielded neutron detector are plotted. The neutron detector is denoted as HXR-S, because it is also sensitive to high energy photons (MeV). The last graph shows the signals from all three channels of the Cherenkov detector.

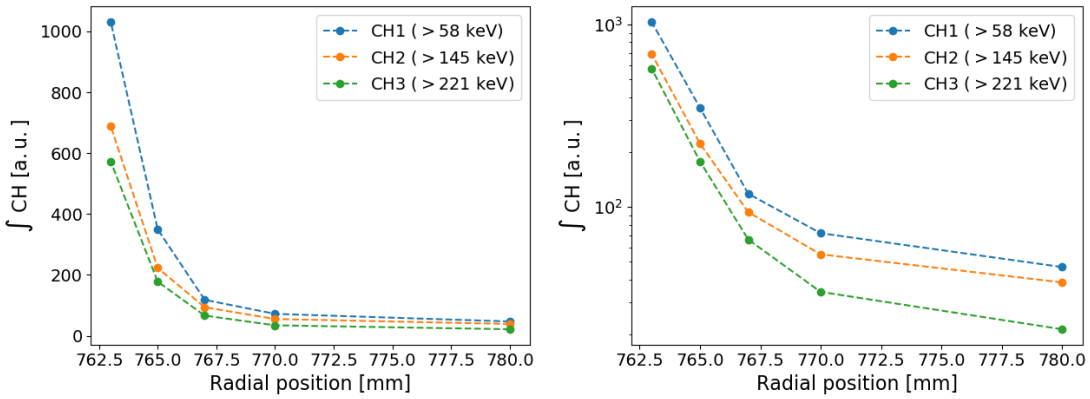

Figure 5.5: The radial profile of the electrons fluency $\int CH$ (integral of the signal from the Cherenkov detector in time domain). CH1, CH2 and CH3 denote signals from the first, the second and the third channel of the Cherenkov detector. In the right figure the radial profile recorded by the Cherenkov detector is shown in the logarithmic scale.

5.4.1 The radial position scan

The radial position scan is displayed in figure 5.5. The scan was done on shot-to-shot basis and for the scan shots #14558-145660, #14562-14563 were used. In figure 5.4 the basic signals from the one shot from the scan are shown. All five shots were carried out with the same parameters and with the same setting of the PMT of the Cherenkov detector. Data points in the figure 5.5 were obtained by integration of the signals from the Cherenkov detector during the whole discharge.

As it can be seen in the figures, the magnitude of the electrons fluency is approximately the same for all channels in the most outer position (0.780 m), which is actually hidden in the port of the tokamak. With the decreasing radial position, the electron fluency rises and the differences between channels are gradually increasing. From figure 5.5 it can be see, that the signals are increasing steeper than exponentially.

If we compare the figures 5.5 with the results of the simulations, where the reconstruction of the radial profile was made, a large discrepancy can be seen. The experimental observations suggest, that the number of detected electrons is increasing steeper then exponentially with the decreasing radial position, but the results of simulations show linear trend. It has to be also noted, that from the developed model (see chapter 3 and 4) only the electrons with energies higher than 1 MeV can be detected by the Cherenkov detector.

5.4.2 Ramp-up experiments

The most interesting results, which were achieved via measurements with the Cherenkov detector are connected to Argon induced disruptions in the ramp up current phase [44]. Argon triggers the thermal quench (sudden drop of plasma temperature) and thus causes the the rapid increase of the plasma resistivity, which leads to the rise of the loop voltage (rise of the toroidal electric field). The typical evolution of the basic plasma parameters is shown in figure 5.6.

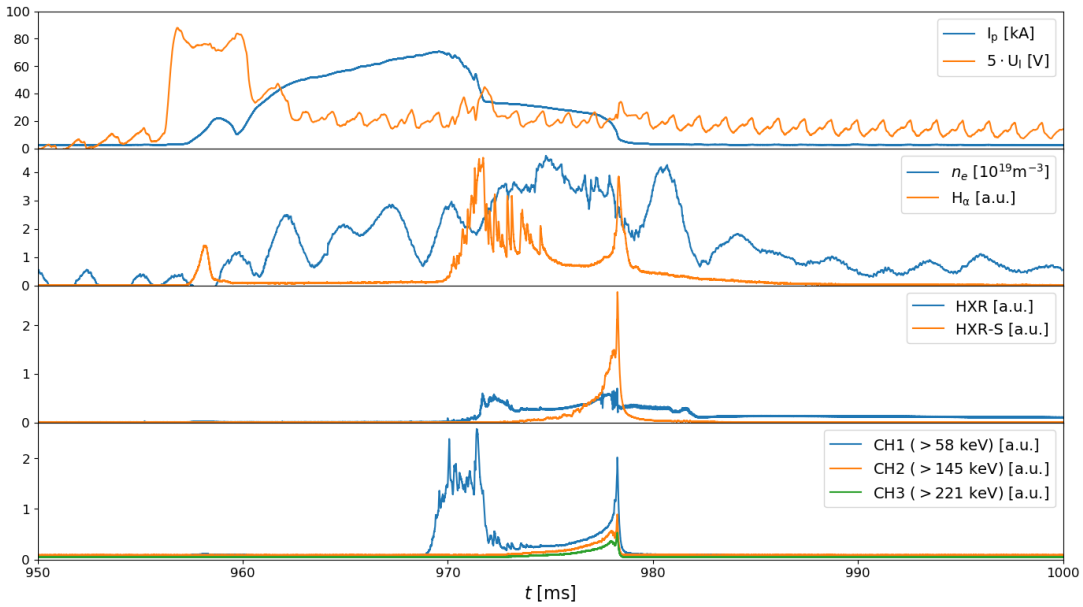

Figure 5.6: The evolution of the selected signals during the argon induced disruption in the ramp up current phase from the COMPASS discharge #13120. In the first graph the plasma current and the loop voltage are displayed. The electron density of the plasma and signal of H_α radiation are shown in the second graph. Third graph shows the signal from the HXR detector (HXR) and from the neutron detector (HXR-S). In the last graph the signals from the multichannel Cherenkov detector are given.

In the 5.6, the evolution of plasma current I_p and the loop voltage U_l can be seen in the first graph. The massive gas injection valve with Argon was triggered at 953 ms, but due to the response time of the valve the estimated time in which gas starts to flow into the chamber is approximately 963 ms. The first stage of the plasma disruptions, the thermal quench, occurs at 970 ms. The start of this phase could be estimated from the drop of the ECE signal, which corresponds to the electron temperature, or by increasing H_α radiation suggesting the plasma cooling. The thermal quench is followed by the current quench phase. This phase is characterized by the rapid decrease of the plasma current I_p. This phase ends when the runaway beam phase is reached and the whole electric current is carried by the runaway electrons. The current carried by the runaway electrons decreases relatively slowly.

In the third graph of the figure 5.6, the signals from the HXR detector (HXR) and neutron detector (HXR-S) are shown. As it is seen in the figure, the HXR signal is present from the beginning of the disruption and quickly saturates, but the signal from the neutron detector appears in the runaway beam phase. This observation suggests that during the disruptions only the low energetic runaways are lost. This phenomenon is also demonstrated in the fourth graph, where the signals from the Cherenkov detector are displayed.

During plasma disruptions, the large burst of a signal from the first channel of the Cherenkov detector appears. All channels of the Cherenkov detector shows consistent behaviour during the runaway beam phase. The fact, that only the channel with the lowest energy threshold has the signal during the disruptions again suggest, that only low energetic runaway electrons are

present.

The comparison of signals from the Cherenkov detector in the case, where the RE beam was created with another one, where it was not, is shown in the figure 5.7. In both cases the burst of the signal from the first channel of the Cherenkov detector is visible. For a deeper analysis of this phenomena see [7]. In figure 5.8 comparison of the signals from the Cherenkov detector is also shown, but in both cases the runaway beam was generated after the disruption. It has to be noted, that the shot #15726 was carried out with the different energy threshold of the first channel. For the shot #13120 the energy threshold was 58 keV as usually in the COMPASS experiments, but in the shot #15726 the energy threshold of the first channel was higher, namely 109 keV. As it is clear from the figure, no burst of the signal from the first channel of the Cherenkov detector is recorded in the shot #15726 (higher threshold). This observation can be easily explained by that only electrons with energies lower than 109 keV are lost during the disruptions and electrons with higher energies are confined and serve as a runway seed.

The explanation could be correct. However, the shapes of the signals from the Cherenkov detector also differ in the runaway electron phase. The Cherenkovs signals from the discharge #13120 are correlated with the decay of the RE beam, but the signals from the Cherenkov detector recorded in the discharge #15726 show only peak in the end of the RE beam phase. This discrepancy in the signals from the RE beam phase could suggest, that the differences between the signals is caused not only by different energy threshold of the first channel.

Another interesting comparison between the signals from the Cherenkov detector is shown in the figure 5.9. In the figure the signals from the Cherenkov detector recorded during the discharge #13120 are display again. This discharge was carried out with the experimental setup, which is shown in the figure 5.1. On the other hand, in the shot #10921 the Cherenkov detector was placed in the same port as in discharge #13120, but the LFS protection limiter was moved on different toroidal position between the coils 9 and 10 (originally between the coils 1 and 16).

An idea how to explain the discrepancy between the recorded signals into the two similar cases, may be as follows. In the figure 5.10 the two configuration of the Cherenkov detector and the LFS protection limiter are displayed. The left figure represents the configuration from the shot #13120. The protection limiter is 180° away from the Cherenkov detector in the toroidal direction, but in the right figure the LFS protection limiter is located in the vicinity of the detector. In both figures the direction of the plasma current is displayed and the toroidal direction of the movement of the individual plasma species is indicated. The different signals from the Cherenkov detector can be caused by the fact that the LFS protection limiter was placed on the toroidal position in front of the Cherenkov detector from the electrons side, so that all potentially detectable electrons had impacted on the protection limiter.

The situation discussed in this section is hardly comparable with results of simulations, because the topology of the magnetic field is unknown. The reconstruction of the magnetic field by the equilibrium code EFIT is not feasible in the RE dominated scenarios.

5.4.3 Recorded MHD activity

The Cherenkov detector is also capable to provide deeper insight into processes behind mechanisms of the runaway electrons losses. In figure 5.11 evolution of the basic signals is shown. At the first sight, the signal from the Cherenkov detector shows interesting behaviour.

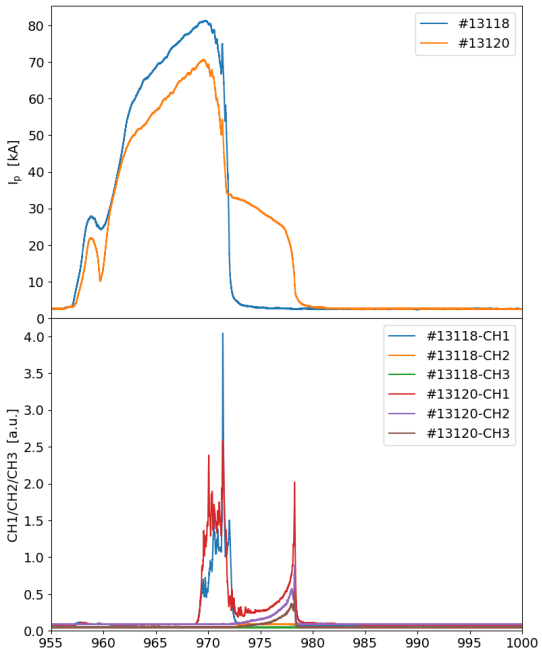

Figure 5.7: The comparison of the signals after Argon induced disruption. In the shot #13120 the RE beam was created, but shot #13118 ends without RE beam generation after the disruption.

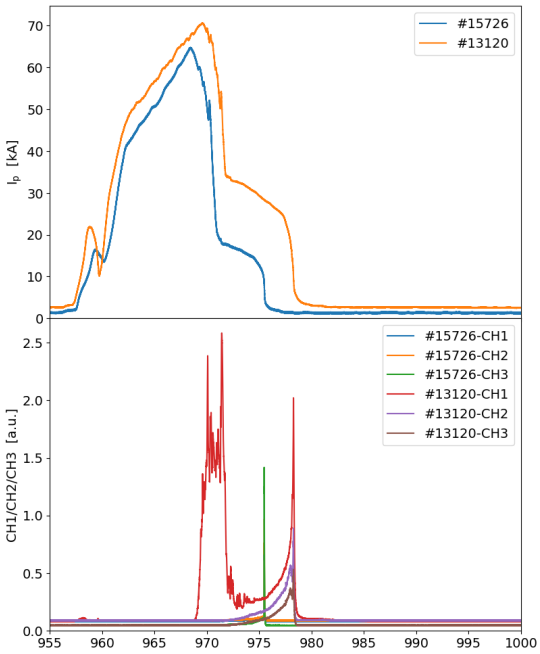

Figure 5.8: The comparison of the signals after Argon induced disruption. The first channel of the Cherenkov detector had energy threshold 58 keV (#13120) and 109 keV (#15726).

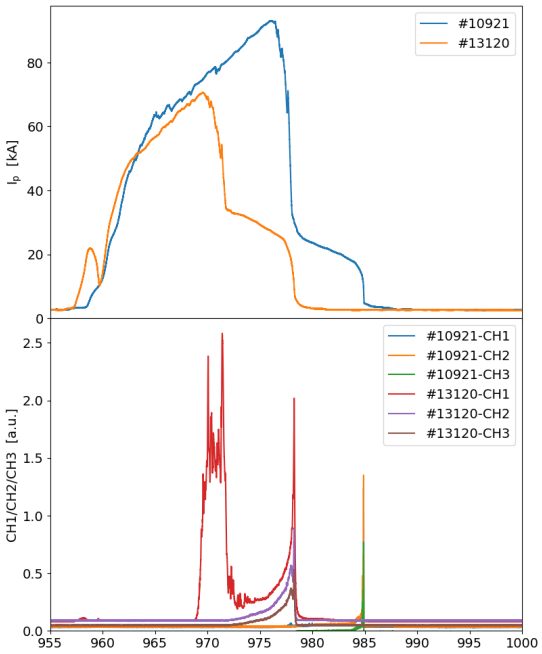

Figure 5.9: The comparison of the signals after Argon induced disruption. The two shots were carried out with different toroidal position of the Cherenkov detector.

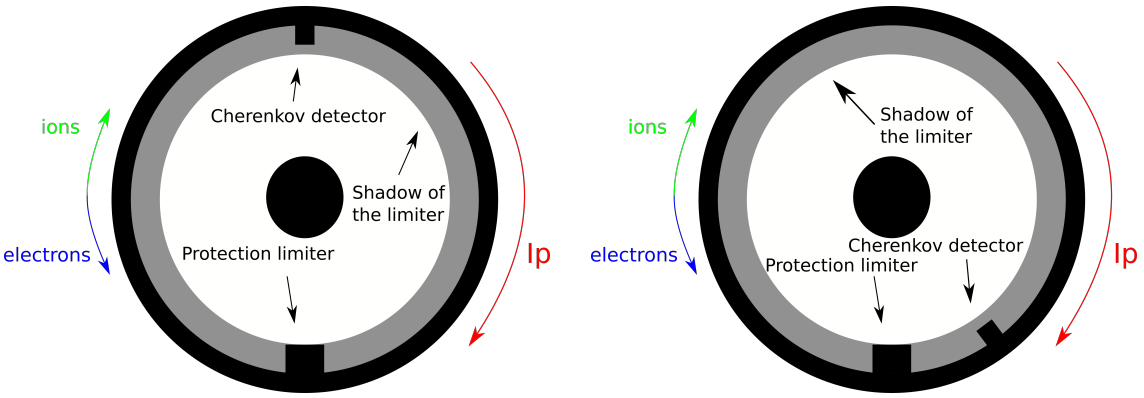

Figure 5.10: Illustration of the two configurations used in the campaigns dedicated to the investigation of the runaway electrons. In the first case (left), the Cherenkov detector was located on the LFS and was located at position, which was 180° away in the toroidal direction from the LFS protection limiter. In the second case (right), the Cherenkov detector was placed in the vicinity of the LFS protection limiter. As it is shown in the figure, the LFS protection limiter is in the later case in front of the Cherenkov detector in the direction of the movement of the electrons.

It is clearly seen, that the signals are periodic. Because the signals from the Cherenkov detector can be interpreted as losses of fast electrons, one can search for the reason of the periodic losses.

In figure 5.12 coherence of the signal from the first channel of the Cherenkov detector with the signal from the Mirnov Coil (A2) is given. At the end of the discharge the large correlation between the signals is visible. This observations means that in this stage of the discharge signals have the same frequencies. The Mirnov coil measures the MHD activity of the plasma and indicates the presence of a magnetic island in the plasma. The magnetic islands cause magnetic perturbations, which can affect dynamics of the fast particles. For this reason the correlation between the signals can be observed. This behaviour was already observed on tokamkak COMPASS with help of different diagnostics [8, 15].

Details of the signal from the first channel of the Cherenkov detector and from the Mirnov coil are displayed in the figure 5.13. From the figure it is clearly seen that the signals have the same frequencies, however the signal from the Cherenkov detector is also modulated by another lower frequency.

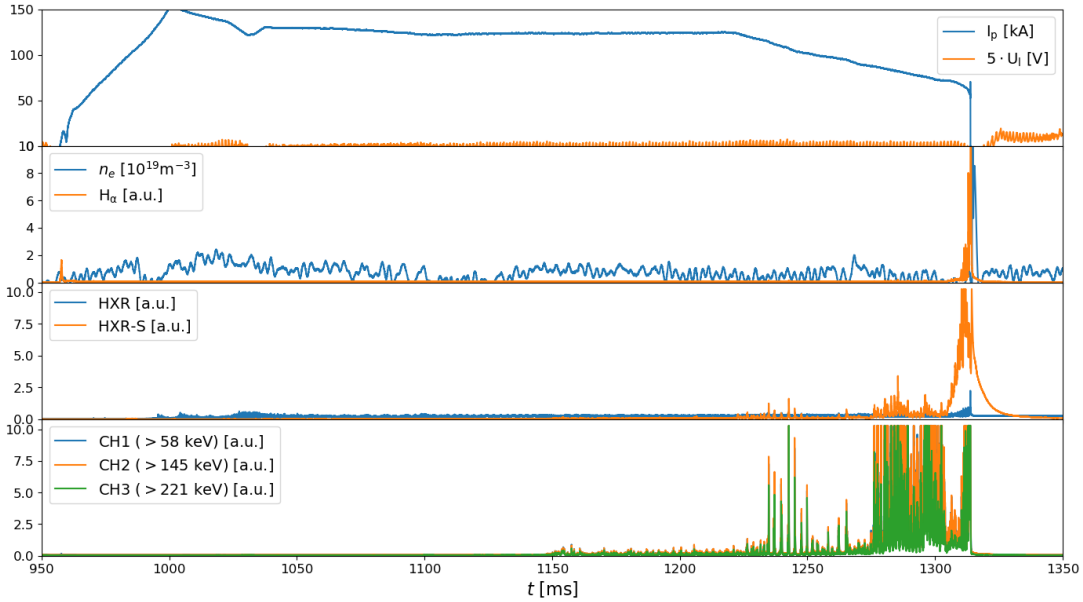

Figure 5.11: The figure shows the evolution of the basic signals in the shot #13179.

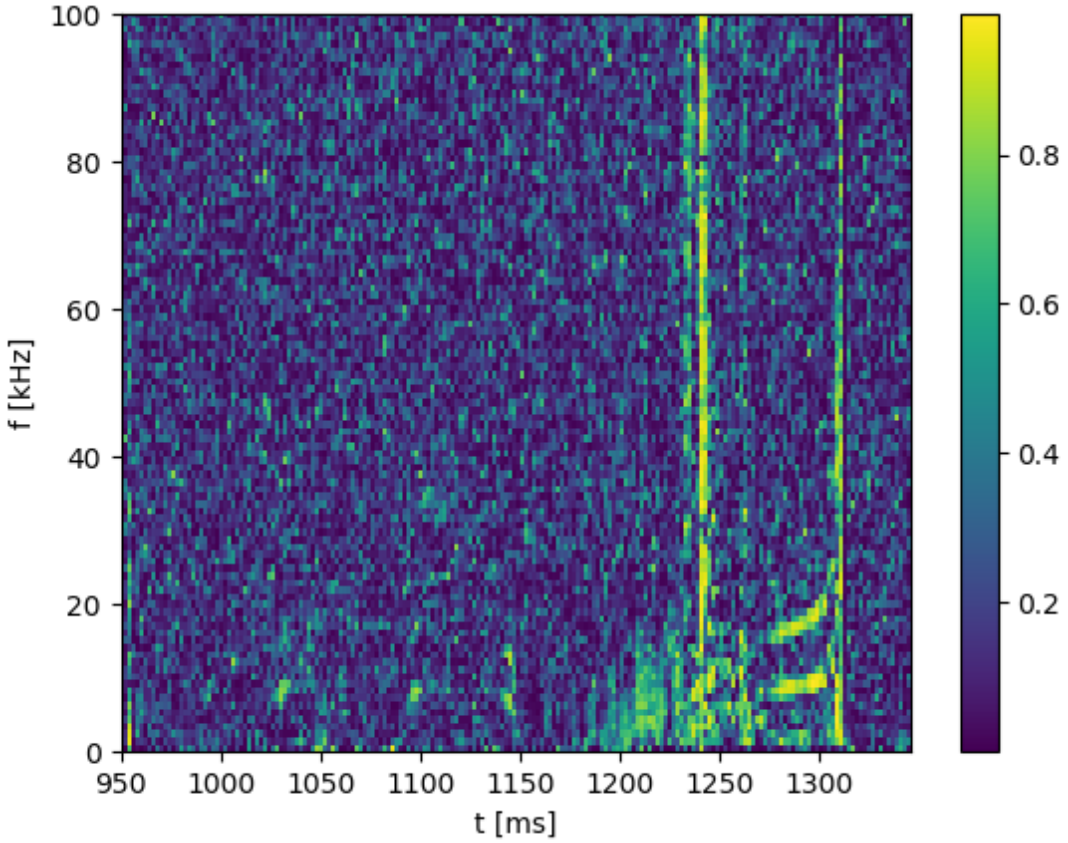

Figure 5.12: Coherence of the signal from the first channel of the Cherenkov detector with the signal from the Mirnov Coil (A2) recorded in the shot #13179. The figure shows the correlation of the signals.

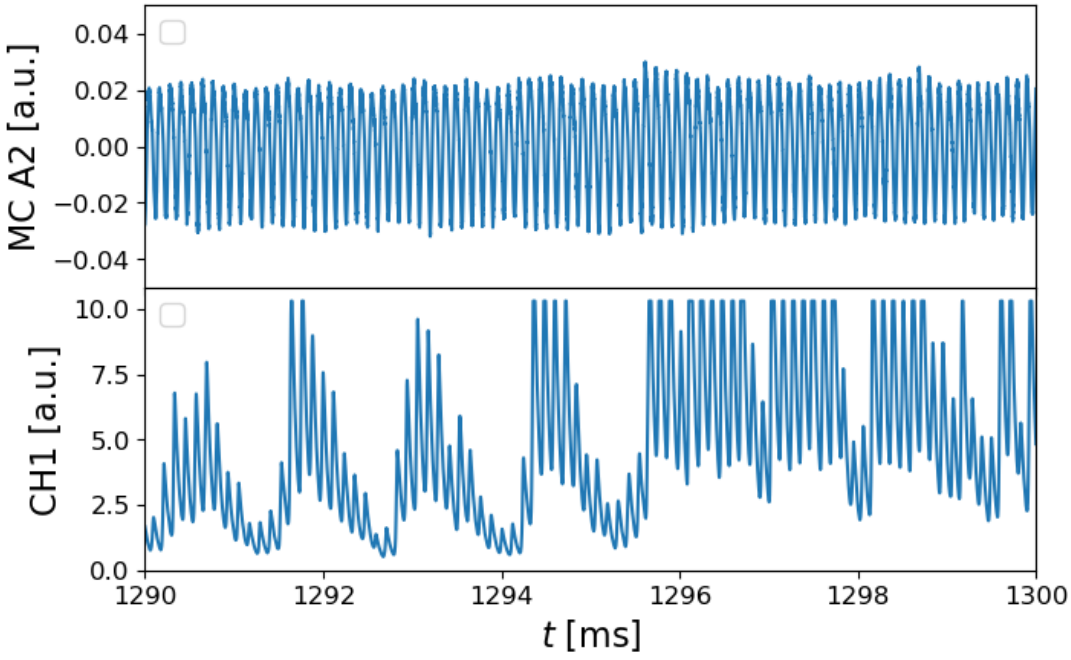

Figure 5.13: The first graph shows the signal from the Mirnov coil (A2), which indicates the MHD activity. The signal from first channel of Cherenkov detector is shown in the second graph.

Summary

The first part of this thesis summarises the fundamental knowledge about physics of runaway electrons. The possible generation processes are listed and importance of the particle radiation is discussed. A substantial part of the thesis is dedicated to the modelling of the particle motion in the magnetic field of the tokamak. The particle simulation are later used for interpretation of measurements with the Cherenkov detector, which can provide useful information about the dynamics of the fast electrons.

The first chapter begins with the intuitive description of the runaway electrons phenomena and gives insight into generation mechanisms of runaway electrons in the present and future tokamaks. In the first chapter, the radiative processes affecting the dynamic of the charged particles are also discussed and importance of the particle radiation for diagnostic purposes is pointed out. The chapter ends with a part dedicated to description of the RE-wall interaction.

In the second chapter the extensive list of numerical methods for determination of movements of the charged particle in an electromagnetic field is given. Firstly, the basics of the physics behind the motion of charged particle is reviewed. The following sections of this chapter present with various methods of calculation of particle trajectories. Two different approaches are discussed - the full orbit modelling, which reconstructs the trajectory of the particle including the Larmor radius, and guiding centre approach, which concentrates only on calculation of the position of the guiding centre.

The third chapter summarises methods required for implementation of the algorithm and also introduces the implemented algorithm, which is capable to calculate the trajectories of the runaway electrons in the magnetic field of the COMPASS tokamak. In the third chapter, the reconstruction of the magnetic field on the tokamak COMPASS is briefly explained and techniques used in simulation code are described.

In the fourth chapter, of this thesis, the results obtained by the simulation code are given. The simulation method capable to study the dynamics of the escaping runaway electrons from the plasma volume is presented and the constraints of the developed model are discussed. The simulation code is used for determination of the location of the particle impact. However, the main reason for which the simulation code was developed was an attempt to give insight into measurements with the Cherenkov detector. The simulations are carried out with various parameters of the magnetic field in the effort to determine the features of detectable particles for different radial positions of the Cherenkov detector head.

The last, more experimental, chapter is dedicated to comparison of the results of simulations with the experimental measurements. At first, the experimental setup used during the experiments with the runaway electrons is shown. Then the brief description of the Cherenkov detector is given and its principle is explained. Subsequently, the experimental results obtain

during the position scan with the Cherenkov detector are shown and discrepancy with results obtained by simulation is discussed. The details of the other measurements with the Cherenkov detector in the scenarios, which the implemented simulation code cannot describe, are given in the second part of this chapter. The most interesting observation is related to the Argon induced disruption in the current ramp-up phase. In this scenario, the Cherenkov detector gives very interesting information and proves that it can be a source of useful information about dynamics of the runaway electrons. Also the capability of the Cherenkov detector to contribute to investigation of losses of runaway electrons influenced by MHD instabilities is demonstrated.

Bibliography

[1] CCFE: How fusion works. http://www.ccfe.ac.uk/How_fusion_works.aspx. [15. 3. 2018].

[2] Bartels, H., Kunugi, T., and Russo, A. Runaway electron effects. *Nucl. Fusion 5* (1994), 225.

[3] Birdsall, C. K., and Langdon, A. B. *Plasma physics via computer simulation*. CRC press, 2004.

[4] Boris, J. P. Relativistic plasma simulation-optimization of a hybrid code. In *Proc. Fourth Conf. Num. Sim. Plasmas, Naval Res. Lab, Wash. DC* (1970), pp. 3–67.

[5] Cary, J. R., and Brizard, A. J. Hamiltonian theory of guiding-center motion. *Reviews of modern physics 81*, 2 (2009), 693.

[6] Čerenkov, P. Visible radiation produced by electrons moving in a medium with velocities exceeding that of light. *Physical Review 52*, 4 (1937), 378.

[7] Čeřovský, J. The Cherenkov detector role in the Runaway Electron diagnostics on tokamak COMPASS. Research Task. Faculty of Nuclear Sciences and Physical Engineering of CTU in Prague, 2017. https://physics.fjfi.cvut.cz/publications/FTTF/VU_Jaroslav_Cerovsky.pdf [16. 2. 2018].

[8] Čeřovský, J. Ubíhající elektrony v tokamacích. Bachelor Thesis. Faculty of Nuclear Sciences and Physical Engineering of CTU in Prague, 2016. https://physics.fjfi.cvut.cz/publications/FTTF/BP_Jaroslav_Cerovsky.pdf [20. 1. 2018].

[9] Cherenkov, P. A. Visible emission of clean liquids by action of γ radiation. *Doklady Akademii Nauk SSSR 2* (1934), 451.

[10] Connor, J., and Hastie, R. Relativistic limitations on runaway electrons. *Nuclear fusion 15*, 3 (1975), 415.

[11] Dreicer, H. Electron and ion runaway in a fully ionized gas. i. *Physical Review 115*, 2 (1959), 238.

[12] Dreicer, H. Electron and ion runaway in a fully ionized gas. ii. *Physical review 117*, 2 (1960), 329.

[13] Embréus, O., Stahl, A., Newton, S., Papp, G., Hirvijoki, E., and Fülöp, T. Effect of bremsstrahlung radiation emission on distributions of runaway electrons in magnetized plasmas. *arXiv preprint arXiv:1511.03917* (2015).

[14] Ficker, O. Generation, losses and detection of runaway electrons in tokamaks. Master's thesis, Faculty of Nuclear Sciences and Physical Engineering of CTU in Prague, 2015. `https://physics.fjfi.cvut.cz/publications/FTTF/DP_Ondrej_Ficker.pdf` [12. 2. 2018].

[15] Ficker, O., Mlynar, J., Vlainic, M., Cerovsky, J., Urban, J., Vondracek, P., Weinzettl, V., Macusova, E., Decker, J., Gospodarczyk, M., et al. Losses of runaway electrons in mhd-active plasmas of the compass tokamak. *Nuclear Fusion 57*, 7 (2017), 076002.

[16] Fülöp, T., Pokol, G., Helander, P., and Lisak, M. Destabilization of magnetosonic-whistler waves by a relativistic runaway beam. *Physics of Plasmas 13*, 6 (2006), 062506.

[17] Gallmeier, F. General purpose photoneutron production in mcnp4a. Tech. rep., Oak Ridge National Lab., TN (United States), 1995.

[18] Guan, X., Qin, H., and Fisch, N. J. Phase-space dynamics of runaway electrons in tokamaks. *Physics of Plasmas 17*, 9 (2010), 092502.

[19] Higuera, A. V., and Cary, J. R. Structure-preserving second-order integration of relativistic charged particle trajectories in electromagnetic fields. *Physics of Plasmas 24*, 5 (2017), 052104.

[20] Hoppe, M., Embreus, O., Paz-Soldan, C., Moyer, R. A., and Fulop, T. Interpretation of runaway electron synchrotron and bremsstrahlung images. *Nuclear Fusion* (2018).

[21] Hoppe, M., Embréus, O., Tinguely, R. A., Granetz, R. S., Stahl, A., and Fülöp, T. Soft: A synthetic synchrotron diagnostic for runaway electrons. *Nuclear Fusion 58*, 2 (2018), 026032.

[22] Jimenez, J., and Campos, I. Models of the classical electron after a century. *Foundations of Physics Letters 12*, 2 (1999), 127–146.

[23] Kurki-Suonio, T., Asunta, O., Hellsten, T., Hynönen, V., Johnson, T., Koskela, T., Lönnroth, J., Parail, V., Roccella, M., Saibene, G., et al. Ascot simulations of fast ion power loads to the plasma-facing components in iter. *Nuclear Fusion 49*, 9 (2009), 095001.

[24] Liu, C. *Runaway electrons in tokamaks*. PhD thesis, Princeton University, 2017.

[25] Macusova, E. Estimation of the runaway electron current during the flattop phase in compass. In *EPS 2017: 44th European Physical Society Conference on Plasma Physics. Vol. 41F Mulhose: European Physical Society* (2017).

[26] Martín-Solís, J., Loarte, A., and Lehnen, M. Formation and termination of runaway beams in iter disruptions. *Nuclear Fusion 57*, 6 (2017), 066025.

[27] Nilsson, E. *Dynamics of runaway electrons in tokamak plasmas*. PhD thesis, CEA, 2015.

[28] Nilsson, E., Decker, J., Fisch, N., and Peysson, Y. Trapped-electron runaway effect. *Journal of Plasma Physics 81*, 4 (2015).

[29] Pánek, R., Bilyková, O., Fuchs, V., Hron, M., Chráska, P., Pavlo, P., Stöckel, J., Urban, J., Weinzettl, V., Zajac, J., et al. Reinstallation of the compass-d tokamak in ipp ascr. *Czechoslovak Journal of Physics 56*, 2 (2006), B125–B137.

[30] Pfefferlé, D. *Energetic ion dynamics and confinement in 3D saturated MHD configurations*. PhD thesis, 2015.

[31] Plyusnin, V., Jakubowski, L., Zebrowski, J., Duarte, P., Malinowski, K., Fernandes, H., Silva, C., Rabinski, M., and Sadowski, M. Development of a diagnostic technique based on cherenkov effect for measurements of fast electrons in fusion devices. *Review of Scientific Instruments 83*, 8 (2012), 083505.

[32] Pétri, J. A fully implicit numerical integration of the relativistic particle equation of motion. *Journal of Plasma Physics 83*, 2 (2017), 705830206.

[33] Qin, H., Zhang, S., Xiao, J., Liu, J., Sun, Y., and Tang, W. M. Why is boris algorithm so good? *Physics of Plasmas 20*, 8 (2013), 084503.

[34] Rosenbluth, M., and Putvinski, S. Theory for avalanche of runaway electrons in tokamaks. *Nuclear Fusion 37*, 10 (1997), 1355.

[35] Smith, H., Fehér, T., Fülöp, T., Gál, K., and Verwichte, E. Runaway electron generation in tokamak disruptions. *Plasma Physics and Controlled Fusion 51*, 12 (2009), 124008.

[36] Smith, H. M., and Verwichte, E. Hot tail runaway electron generation in tokamak disruptions. *Physics of Plasmas 15*, 7 (2008), 072502.

[37] Snicker, A., et al. *Towards realistic orbit-following simulations of fast ions in ITER*. PhD thesis, 2014.

[38] Snicker, A., Kurki-Suonio, T., and Sipila, S. K. Realistic simulations of fast-ion wall distribution including effects due to finite larmor radius. *IEEE Transactions on Plasma Science 38*, 9 (2010), 2177–2184.

[39] Stahl, A., Landreman, M., Papp, G., Hollmann, E., and Fülöp, T. Synchrotron radiation from a runaway electron distribution in tokamaks. *Physics of Plasmas 20*, 9 (2013), 093302.

[40] Takeda, T., Tani, K., Tsunematsu, T., Kishimoto, Y., Kurita, G., Matsushita, S., and Nakata, T. Plasma simulator metis for tokamak confinement and heating studies. *Parallel computing 18*, 7 (1992), 743–765.

[41] Tao, X., Chan, A. A., and Brizard, A. J. Hamiltonian theory of adiabatic motion of relativistic charged particles. *Physics of Plasmas 14*, 9 (2007), 092107.

[42] Vay, J.-L. Simulation of beams or plasmas crossing at relativistic velocity. *Physics of Plasmas 15*, 5 (2008), 056701.

[43] Vay, J.-L., and Godfrey, B. B. Modeling of relativistic plasmas with the particle-in-cell method. *Comptes Rendus Mécanique 342*, 10 (2014), 610–618.

[44] Vlainic, M. Post-disruptive runaway electron beam in compass tokamak. *arXiv preprint arXiv:1503.02947* (2015).

[45] Ware, A. Pinch effect for trapped particles in a tokamak. *Physical Review Letters 25*, 1 (1970), 15.

[46] Zhang, R., Liu, J., Qin, H., Wang, Y., He, Y., and Sun, Y. Volume-preserving algorithm for secular relativistic dynamics of charged particles. *Physics of Plasmas 22*, 4 (2015), 044501.

[47] Zohuri, B. *Plasma Physics and Controlled Thermonuclear Reactions Driven Fusion Energy*. Springer, 2016.

Appendix A

Simulation scripts

All scripts used for calculation of the trajectories of runaway electrons in the COMPASS tokamak are available at web page:

`https://drive.google.com/drive/folders/1uMKq9RkDcZcNgvrp6T0LQMScIf_nPgnM?usp=sharing`.

For proper functionality of the code the access to the COMPASS database is needed. The example of use of programme is shown in script *sim_example.py*. Please contact the author in case of any problems.